


Spring 1-1-2014

# An Investigation of Alternate Transfer Strategies to the Sun-Earth Triangular Lagrangian Points

Brian Wesley Lathrop

University of Colorado Boulder, shellao@comcast.net

Follow this and additional works at: [https://scholar.colorado.edu/asen\\_gradetds](https://scholar.colorado.edu/asen_gradetds)

 Part of the [Astrodynamics Commons](#), and the [Navigation, Guidance, Control and Dynamics Commons](#)

## Recommended Citation

Lathrop, Brian Wesley, "An Investigation of Alternate Transfer Strategies to the Sun-Earth Triangular Lagrangian Points" (2014).  
*Aerospace Engineering Sciences Graduate Theses & Dissertations*. 84.  
[https://scholar.colorado.edu/asen\\_gradetds/84](https://scholar.colorado.edu/asen_gradetds/84)

This Dissertation is brought to you for free and open access by Aerospace Engineering Sciences at CU Scholar. It has been accepted for inclusion in Aerospace Engineering Sciences Graduate Theses & Dissertations by an authorized administrator of CU Scholar. For more information, please contact [cuscholaradmin@colorado.edu](mailto:cuscholaradmin@colorado.edu).

**AN INVESTIGATION OF ALTERNATE TRANSFER STRATEGIES TO THE  
SUN-EARTH TRIANGULAR LAGRANGIAN POINTS**

by

**BRIAN WESLEY LATHROP**

B.S., Aerospace Engineering and Mechanics, University of Minnesota, 1988

M.S., Aerospace Engineering, Pennsylvania State University, 1990

A thesis submitted to the  
Faculty of the Graduate School of the  
University of Colorado in partial fulfillment  
of the requirement for the degree of  
Doctor of Philosophy  
Department of Aerospace Engineering Sciences  
2014

This thesis entitled:  
An Investigation of Alternate Transfer Strategies to the Sun-Earth Triangular  
Lagrangian Points  
written by Brian Wesley Lathrop  
has been approved for the Department of Aerospace Engineering Sciences

---

George H. Born

---

Jeffrey S. Parker

Date\_\_\_\_\_

The final copy of this thesis has been examined by the signatories, and we find that both the content and the form meet acceptable presentation standards of scholarly work in the above mentioned discipline.

Lathrop, Brian Wesley (Ph.D., Aerospace Engineering Sciences)

An Investigation of Alternate Transfer Strategies to the Sun-Earth

Triangular Lagrangian Points

Thesis directed by Professor George H. Born (Chair)

Techniques for low energy transfers have been applied to constructing trajectories to various locations in the solar system. Previous techniques have concentrated on orbit matching trajectory maneuvers and two-body transfers. This research investigates several strategies for low energy transfers that can be utilized to intersect desirable objects or locate to different equilibrium regions in the solar system. The principle tools utilized in this investigation stem from the three-body problem and the development of Lagrangian equilibrium points, periodic orbits and invariant manifolds. Another principle tool is the use of low thrust propulsion to develop low energy transfer trajectories utilizing long duration flight times. Of primary interest is the transfer to the Sun-Earth triangular equilibrium Lagrange points, commonly referred to as  $L_4$  and  $L_5$ . Given the localized stability of these regions leading and trailing the Earth as it orbits the Sun, there is low cost to keep a spacecraft in these locations to perform scientific investigations. Of primary interest in the S-E  $L_4/L_5$  regions is the study of small body Trojan asteroids and near Earth objects, stereoscopic solar observations, and various space weather and early warning solar storm detection. This research attempts to minimize the trajectory transfer cost in terms of velocity maneuver impacts.



## DEDICATION

To Michele, my family, and my friends, whose support and encouragement have been never ending, and meant all the difference.

“I have no special talents. I am only passionately curious.”

- Albert Einstein

## ACKNOWLEDGMENT

I would like to express special gratitude for the members of my Ph.D. committee for the time and effort spent supporting me through my long journey. And especially for their patience as I balanced work and research, if not always meeting schedules, certainly growing my knowledge and broadening my perspective from many different levels.

First I thank Brandon Jones for stepping in late but providing keen insight and probing questions. I would like to thank Webster Cash for his kind demeanor and his alternative looks at the approach and problem at hand. A special thank you to Rodney Anderson who at one time I had tutored, but has since introduced me to the three-body problem and given me much more tutoring and insight than I could have ever given him.

I am honored to have worked with Alan Stern, who gave me great inspiration for this research and continues to support me even though he has been called away to his many important tasks. I couldn't have completed this task without the support and guidance of Jeffrey Parker, who helped me initially then went off to expand his career. Fortunately my journey lasted long enough to still be going when he decided to come back and teach. He once again guided me through the last pieces of research, and was always there with advice and the right amount of realism to keep things going.

Finally, my sincerest gratitude to my research advisor, Dr. George Born. He stuck by me through the entire journey, from guiding me early on through orbit determination to leading my requests for time and support from my employer and the graduate school. His breadth of knowledge, experience, guidance and dry wit enriched my experience and made the journey more than worth the effort, as he always said it would.

I must also give thanks to the many colleagues and managers that supported me from my employer throughout this journey. And also a special thanks to my family and friends that shared my excitement for the work and the goals. Especially my wife, Michele, whose love and support is endless.

## CONTENTS

### Table of Contents

CHAPTER 1 INTRODUCTION	1
1.1 Motivation	1
1.2 Background Information	2
1.3 Dissertation Organization	6
CHAPTER 2 TRANSPORT METHODS	7
2.1 The Circular Restricted Three-Body Problem (CRTBP)	7
2.1.1 Summary of the Three-Body Problem	7
2.1.2 Definition of the CRTBP	9
2.1.3 Equations of Motion	10
2.1.4 Jacobi Integral of Motion	11
2.1.5 Zero-Velocity Curves	12
2.2 Periodic Orbits	13
2.2.1 Construction of Periodic Orbits in the CRTBP	14
2.3 Invariant Manifolds	24
2.3.1 Invariant Manifolds of Unstable Periodic Orbits	24

2.4	Low Thrust	27
2.4.1	Low Thrust Optimization	28
2.4.2	Optimized Low Thrust Transfer Examples	28
CHAPTER 3 CHARACTERISTICS OF THE 3-BODY SYSTEM		33
3.1	Relationships for Different 3-Body Systems	33
3.1.1	Jacobi Constant Characteristics of KBO's	33
3.1.2	Parametric Evaluation of the Jacobi Constant	39
3.1.3	Invariant Manifold Structure vs. Jacobi Constant	41
3.1.4	Intersections of Manifolds with KBO Orbits	44
3.1.5	Summary of Method	50
3.2	Manifold Transport to NEO's	50
3.2.1	Periodic Orbits in the CRTBP	51
3.2.2	Invariant Manifolds of Unstable Periodic Orbits	52
3.2.3	Computation for Total $\Delta V$ to Rendezvous	54
3.2.4	Limitations of the Analysis	57
3.2.5	Results and Analysis	59
3.2.6	Specific Cases	66
3.2.7	Summary of Method	69
3.3	Periodic to Periodic Orbit Transfer	70
3.3.1	Grid Search Method	71
CHAPTER 4 LOW ENERGY TRANSFERS (APPLICATIONS TO L4/L5)		79
4.1	Impulsive Ballistic Transfers	79

4.2	Low Thrust Transfers	87
4.2.1	Direct Transfer to S-E $L_4$	88
4.2.2	Direct Transfer to S-E $L_5$	95
4.3	Manifold Transport	101
4.3.1	Transfer From S-E $L_1$ Staging Orbits to $L_4$ Periodic Orbits	103
4.3.2	Transfer From S-E $L_2$ Staging Orbits to $L_4$ Periodic Orbits	105
4.3.3	Transfer From S-E $L_1$ Staging Orbits to $L_5$ Periodic Orbits	107
4.3.4	Transfer From S-E $L_2$ Staging Orbits to $L_5$ Periodic Orbits	109
CHAPTER 5 SUMMARY AND CONCLUSIONS		111
5.1	Summary of Contributions	111
5.2	Conclusions	111
5.3	Future Work	113
BIBLIOGRAPHY.....		116
APPENDIX A .....		120

## TABLES

Table 3-1. Simple Hohmann transfer velocity increments to transfer from Earth to various binary KBO orbits.....	46
Table 3-2 Total $\Delta V$ from a 185 km Circular LEO Park Orbit to various Sun-Earth Lagrange Point Lyapunov Orbits .....	55

## FIGURES

- Figure 2-1. Zero-velocity curves for the Sun-Neptune system, with Jacobi constant values corresponding to the equilibrium L1 (left) and L2 (right) points..... 13
- Figure 2-2. Family of Periodic Lyapunov Orbits about the S-E L1 Equilibrium Point. The Jacobi constants,  $C$ , increase in magnitude the closer to the L1 centroid they are..... 19
- Figure 2-3. Family of Periodic Lyapunov Orbits about the S-E L2 Equilibrium Point. The Jacobi constants,  $C$ , increase in magnitude the closer to the L2 centroid they are..... 19
- Figure 2-4. Family of Periodic Lyapunov Orbits Concentric about the S-E L4 Equilibrium Point. .... 20
- Figure 2-5. Closeup of Family of Periodic Lyapunov Orbits Concentric about the S-E L4 Equilibrium Point. The Jacobi constants,  $C$ , increase in magnitude the closer to the L4 centroid they are..... 21
- Figure 2-6. Family of Periodic Lyapunov Orbits Concentric about the S-E L5 Equilibrium Point. The Jacobi constants,  $C$ , increase in magnitude the closer to the L5 centroid they are..... 22
- Figure 2-7. Family of Periodic Lyapunov Orbits that Intersect the S-E L5 Equilibrium Point. These are all periodic about different radial axes, but all go through the L5 point at the lower apex of their shape. .... 23
- Figure 2-8. The unstable (top) and stable (bottom) invariant manifolds for a periodic orbit about the Sun-Neptune L2 equilibrium point. .... 26
- Figure 2-9. Low Thrust Transfer to S-E L4 for  $I_{sp} = 1500$  s and  $TOF = 1.833$  yrs. This figure shows (a) rotating frame trace, (b) inertial frame trace, (c) argument of perihelion, (d) apohelion and perihelion radii, and (e) thrust profile for this transfer. .... 29



Figure 2-10. Low Thrust Transfer to S-E L4 for $I_{sp} = 4000$ s and TOF = 3.333 yrs. This figure shows (a) rotating frame trace, (b) inertial frame trace, (c) argument of perihelion, (d) apohelion and perihelion radii, and (e) thrust profile for this transfer.....	30
Figure 2-11. Low Thrust Transfer to S-E L5 for $I_{sp} = 2000$ s and TOF = 1.667 yrs. This figure shows (a) rotating frame trace, (b) inertial frame trace, (c) argument of perihelion, (d) apohelion and perihelion radii, and (e) thrust profile for this transfer.....	31
Figure 2-12. Low Thrust Transfer to S-E L5 for $I_{sp} = 3000$ s and TOF = 5.400 yrs. This figure shows (a) rotating frame trace, (b) inertial frame trace, (c) argument of perihelion, (d) apohelion and perihelion radii, and (e) thrust profile for this transfer.....	32
Figure 3-1. Jacobi constant values for Centaur class KBO's for the Sun/outer planet systems.....	35
Figure 3-2. Jacobi constant values for Jupiter Trojan class KBO's for the Sun/outer planet systems. ....	36
Figure 3-3. Jacobi constant values for TNO class KBO's for the Sun/outer planet systems. ....	36
Figure 3-4. Jacobi constant values for the KBO's as a function of various orbital parameters. ....	38
Figure 3-5. Jacobi constant values as a function of mass ratio for a stationary object in the CRTBP.....	40
Figure 3-6. Unstable invariant manifold structures from various periodic orbits about the Sun-Saturn L2.....	44
Figure 3-7. Intersections between the unstable invariant manifolds from an L2 orbit in the Sun-Uranus system and the binary KBO 2002 CR46. ....	49
Figure 3-8. Periodic L2 Lagrange point Lyapunov orbit with Jacobi Constant value equal to 3.00051. ....	53
Figure 3-9. Periodic L2 Lagrange point Lyapunov orbit with Jacobi Constant value equal to 3.00081. ....	53
Figure 3-10. Total $\Delta V$ as function of NEO semimajor axis.....	62
Figure 3-11. Total $\Delta V$ as function of NEO eccentricity.....	62

Figure 3-12. Total $\Delta V$ as function of NEO inclination. ....	63
Figure 3-13. Total $\Delta V$ as a function of the relative change in Jacobi Constant between the Lyapunov periodic orbit and the NEO object.....	66
Figure 3-14. Total trajectory from LEO park orbit to rendezvous of example ATE asteroid 2004 FH. This example utilizes an interior region starting unstable manifold from an L2 Lyapunov orbit with Jacobi constant value equal to 3.00051. ....	69
Figure 3-15. Total trajectory from LEO park orbit to rendezvous of example APO asteroid 2007 UN12. This example utilizes an exterior region starting unstable manifold from an L2 Lyapunov orbit with Jacobi constant value equal to 3.00051. ....	69
Figure 3-16. Propagation of Unstable Manifolds from S-E L1/L2 Lyapunov Orbits to Intersections with L4/L5 Lyapunov Orbits. ....	71
Figure 3-17. Closeup of Propagation of Unstable Manifolds from S-E L1/L2 Lyapunov Orbits. ....	72
Figure 3-18. Closeup of Propagation of Unstable Manifolds Intersecting S-E L4 Centered Periodic Lyapunov Orbit.....	73
Figure 3-19. Closeup of Propagation of Unstable Manifolds Intersecting S-E L5 Intersecting Periodic Lyapunov Orbit.....	74
Figure 3-20. Phase Space Traces of Starting and Ending Periodic Lyapunov Orbits and the Connecting Unstable Manifold. The position axis corresponds to the radial magnitude, and the velocity axis corresponds to the total rotational velocity magnitude. The delta V magnitude is applicable at the positional intersection of the manifold and the ending Lyapunov orbit. ....	75
Figure 3-21. Component Phase Space Traces of Starting and Ending Periodic Lyapunov Orbits and the Connecting Unstable Manifold. The position axes correspond to the component x (top) and y (bottom) positions, respectively. The velocity axes correspond to the component x (top) and y (bottom) velocities, respectively. The component delta V magnitudes are applicable at the positional intersection of the manifold and the ending Lyapunov orbit.....	76
Figure 3-22. Case Solution for Locally Minimum Injection into S-E L4 Centered Lyapunov Orbit Transferring from an L1 Lyapunov Orbit. ....	77

Figure 3-23. Case Solution for Locally Minimum Injection into S-E L5 Intersecting Lyapunov Orbit Transferring from an L2 Lyapunov Orbit. ....	78
Figure 4-1. Circular Coplanar Rendezvous for a Target leading the Interceptor. The example is for the target representing the L4 Lagrange point located at a phase angle of $-60^\circ$ from the initial interceptor point at the Earth. ....	81
Figure 4-2. Circular Coplanar Rendezvous for a Target trailing the Interceptor. The example is for the target representing the L5 Lagrange point located at a phase angle of $+60^\circ$ from the initial interceptor point at the Earth. ....	84
Figure 4-3. Circular Rendezvous Phasing Orbit SMA versus Transit Time. Larger phasing orbits needed to allow L5 target to catch up, while smaller phasing orbits needed to speed up and catch the L4 target. ....	85
Figure 4-4. Total Velocity Needed versus Varying Transit Times for Circular Rendezvous to S-E L4/L5 Targets. Based from impulsive maneuvers from Earth escape to the leading and trailing Lagrange points.....	86
Figure 4-5. Low Thrust Transfer Example to S-E L4 for $I_{sp} = 1500$ sec and TOF $= 1.833$ years. Example case that departs Earth at $C3 = 0$ and intersects L4 in the rotating frame after 1.833 years. The trace in the rotating frame is shown in plot (a), and the inertial frame in plot (b).....	89
Figure 4-6. Total delta V for Low Thrust Transfers to S-E L4 versus Transit Time. Multiple cases for engine $I_{sp}$ variances from 1500 to 4000 sec. Velocity change based on an Earth departure at $C3 = 0$ and intersecting the L4 point in the rotating frame. Lower bound impulsive velocity change shown in dashed black line. ....	90
Figure 4-7. Orbital Parameters versus Total delta V for Low Thrust Transfers to S-E L4. Multiple cases for engine $I_{sp}$ variances from 1500 to 4000 sec. Velocity change nearly linearly affects the in-plane shape of the transferring orbit via the semi-major axis, but is apportioned differently between the two radii of apsides. Comparison to the impulsive velocity change results shown from the dashed black line. ...	92
Figure 4-8. Estimated Fuel Mass versus Transit Time required achieving the desired delta V for a Transfer to S-E L4. Fuel mass varies with engine $I_{sp}$ to achieve the resultant velocity change and is a greater proportion of total payload mass for higher velocity requirements.....	94

- Figure 4-9. Low Thrust Transfer Example to S-E L5 for  $I_{sp} = 4000$  sec and TOF = 4.667 years. Example case that departs Earth at  $C3 = 0$  and intersects L5 in the rotating frame after 4.667 years. The trace in the rotating frame is shown in plot (a), and the inertial frame in plot (b). ..... 96
- Figure 4-10. Total delta V for Low Thrust Transfers to S-E L5 versus Transit Time. Multiple cases for engine  $I_{sp}$  variances from 1500 to 4000 sec. Velocity change based on an Earth departure at  $C3 = 0$  and intersecting the L5 point in the rotating frame. Lower bound impulsive velocity change shown in dashed black line. .... 97
- Figure 4-11. Orbital Parameters versus Total delta V for Low Thrust Transfers to S-E L5. Multiple cases for engine  $I_{sp}$  variances from 1500 to 4000 sec. Velocity change nearly linearly affects the in-plane shape of the transferring orbit via the semi-major axis, but is apportioned differently between the two radii of apsides. Comparison to the impulsive velocity change results shown from the dashed black line. ... 98
- Figure 4-12. Estimated Fuel Mass versus Transit Time required achieving the desired delta V for a Transfer to S-E L5. Fuel mass varies with engine  $I_{sp}$  to achieve the resultant velocity change and is a greater proportion of total payload mass for higher velocity requirements. .... 101
- Figure 4-13. Delta Velocity and Time of Flight for Manifold Transfers from L1 Periodic Orbits injecting into L4 Centered Periodic Orbits. .... 103
- Figure 4-14. Delta Velocity and Time of Flight for Manifold Transfers from L1 Periodic Orbits injecting into Periodic Orbits that intersect L4. .... 104
- Figure 4-15. Delta Velocity and Time of Flight for Manifold Transfers from L2 Periodic Orbits injecting into L4 Centered Periodic Orbits. .... 105
- Figure 4-16. Delta Velocity and Time of Flight for Manifold Transfers from L2 Periodic Orbits injecting into Periodic Orbits that intersect L4. .... 106
- Figure 4-17. Delta Velocity and Time of Flight for Manifold Transfers from L1 Periodic Orbits injecting into L5 Centered Periodic Orbits. .... 107
- Figure 4-18. Delta Velocity and Time of Flight for Manifold Transfers from L1 Periodic Orbits injecting into Periodic Orbits that intersect L5. .... 108
- Figure 4-19. Delta Velocity and Time of Flight for Manifold Transfers from L2 Periodic Orbits injecting into L5 Centered Periodic Orbits. .... 109

Figure 4-20. Delta Velocity and Time of Flight for Manifold Transfers from L2  
Periodic Orbits injecting into Periodic Orbits that intersect L5..... 110

# CHAPTER 1

## INTRODUCTION

### 1.1 Motivation

The primary goal of this research is to find and analyze alternate mission transport schemes to reach the Sun-Earth triangular equilibrium Lagrange point regions, namely  $L_4$  and  $L_5$ . The motivation is to utilize low energy and dynamical system techniques to obtain minimal delta velocity requirements as the cost function and characterize the trade with time of flight for the transfers.

In 2010, the WISE spacecraft mission observed and identified the first Earth orbit Trojan satellite. Asteroid 2010 TK7 was verified by ground based telescopes to be traveling in the Earth's orbit about the Sun in the leading  $L_4$  region (NASA/JPL, 2010). It transits about a periodic orbit near the Sun-Earth  $L_4$  libration point in a "tadpole" orbit, slowly progressing counterclockwise in the rotating frame over a long period of time. It is not such an easy object to visit as the orbit has a large inclination to the ecliptic and would require large velocity maneuvers to reach. But this object validates the long held speculation of small Trojan bodies being located relatively close by the Earth in stable regions of the rotating Sun-Earth system.

Such objects would hold great scientific value if the ability to rendezvous with them if trajectory transfers can be developed to get there within reasonable velocity costs. Many small spacecraft missions have been developed and flown utilizing low energy transfers to different places in the solar system, and this

research hopes to add to this by analyzing alternate methods to achieve those types of results.

## 1.2 Background Information

Equilibrium points in the three-body problem equate to finding the points where an object could be located with the appropriate velocity in the inertial frame, but where it remains stationary in the rotating frame. This is to say that this point is still acted on by forces and follows a Keplerian orbit in the inertial frame, but that it stays fixed in the rotating synodic frame of the Circular Restricted Three Body Problem (CRTBP), described later in Section 2.1.2. The location of these points in the CRTBP can be found by balancing the forces of the two primary masses with the force from the barycenter of the system, which is the only fixed point in the inertial frame. An example of this procedure can be found in (Murray & Dermott, 1999).

The system has an equilibrium point at the apex of an equilateral triangle with the base formed by line joining the two masses (the x-axis in the rotating frame). There is a corresponding equilibrium point below the same line. These are the Lagrange equilibrium points  $L_4$  and  $L_5$ , respectively. In the classical problem there are three more equilibrium points,  $L_1$ ,  $L_2$  and  $L_3$ , which lie on the x-axis. By convention,  $L_1$  lies between the two primary masses,  $L_2$  lies outside of the second primary mass and  $L_3$  lies outside the first primary mass.

It turns out that in the CRTBP the location of the Lagrange points is purely a function of the mass ratio of the two primary bodies,  $\mu$ . For a given value of  $\mu$  all five Lagrange points can be found for the system. It is seen that the equilibrium points get closer to the primary masses as the mass ratio decreases, or as the second

primary gets smaller. Some of these Lagrange points will be used as central points for periodic orbits as described in later sections.

Recently several missions have been designed and launched to small objects in the near Earth solar system. A number of these missions included encounters with asteroids, such as the Near Earth Asteroid Rendezvous (NEAR) mission, which was launched in 1996 to rendezvous with the minor planet 433 Eros but also made a flyby of asteroid 253 Mathilde along the way (see trajectory details in Farquhar et al (Farquhar, Dunham, & McAdams, 1995)). The Hayabusa mission, launched in 2003, was designed to rendezvous with and collect pieces of asteroid 25142 Itokawa and return the samples to Earth (Yano, et al., 2006). This mission utilized a low thrust engine to make the transfer. Another example is the DAWN mission, launched in 2007 and also used low thrust maneuvers, and designed to orbit two separate main asteroid belt objects (first Vesta and then Ceres) starting in 2011 (Rayman, Fraschetti, Raymond, & Russell, 2006). An example of a low  $\Delta V$  mission design to rendezvous with several NEO asteroids for a potential future mission is described by Mitchell (2005) . The trajectory designs for these and several other missions that either fly by or rendezvous with asteroids near Earth utilize orbit matching or Hohmann type transfers. But a survey of the literature has not found any past asteroid missions that have flown and included the use of periodic Lagrange point invariant manifolds directly in the trajectory design.

A number of papers have recently been published in the astronomical community examining surveys of  $\Delta V$  requirements to launch from the Earth and rendezvous with different types of asteroids. These surveys have primarily focused on applying different types of simplifying assumptions to obtain a statistical representation of the types of  $\Delta V$ s that might be expected for asteroids in the current database and for potentially undiscovered asteroids. The results are



applicable to a wide variety of cases ranging from missions to theoretical asteroids to more realistic missions at specific epochs. They have all depended, however, on trajectories computed within the two-body problem. Christou performed a survey using velocity-optimized impulsive Lambert solutions to travel from Earth to the asteroids focusing on 27 actual objects over 11 years (Christou, 2003). The results were compared to Yanez et al.'s (2006) study using solar electric propulsion and Perozzi et al.'s (Perozzi, Rossi, & Valsecchi, 2001) study including some gravity flybys. Christou notes that these two previous studies were phase-independent and examines the corresponding differences in  $\Delta V$ . Stacey and Connors examine the  $\Delta V$  required to travel to a large number of asteroids focusing on phase-independent, low-inclination trajectories (Stacey & Connors, 2009). They also include studies of theoretical trajectories representing undiscovered asteroids and some phase-dependent asteroids, all within the two-body problem. The approach taken here follows the approach taken by Stacey and Connors using trajectories particular to the three-body problem in place of two-body trajectories.

To summarize, these previous surveys of  $\Delta V$  requirements to travel to families of asteroids have primarily focused on computing  $\Delta V$ s using two-body approximations. These have ranged from simple schemes for targeting asteroids to using solutions of Lambert's problem. As previously mentioned they have primarily focused on phase-independent studies, which is the approach also adopted for a portion here. For this research, however, low-energy trajectories to possible rendezvous with various asteroids are computed in the circular restricted three-body problem rather than using the typical two-body approximations. These types of low-energy trajectories have been previously analyzed by Conley (1968) and studied in more detail by Gomez et al. (Gomez, Llibre, Simo, & Simo, 2001). A number of researchers have examined libration point orbits and the possibility of

using invariant manifolds to transfer to them from low Earth orbit (Gomez, Jorba, Masdemont, & Simo, 1993) (Howell, Barden, & Lo, Application of Dynamical Systems Theory to Trajectory Design for a Libration Point Mission, 1997). It has also been suggested that these libration point orbits may act as a gateway from Earth to the rest of the solar system including travel to asteroids and Near Earth Objects (Farquhar, Dunham, Guo, & McAdams, 2004) (Lo, 2001). This research seeks to apply these low-energy trajectories in the form of Lyapunov orbits and their invariant manifolds, and low thrust transfers to the problem of determining transfer trajectories to a wide variety of locations near the Earth.

Very little research has been identified for transfers directly to the Sun-Earth  $L_4/L_5$  regions. Salazar, et al (Salazar, Macau, & Winter, 2013) develop trajectories into triangular Lagrange point orbits but only for the Earth-Moon system, and utilize lunar gravity assists. Llanos, et al (Llanos, Miller, & Hintz, 2012) developed transfers to the Sun-Earth  $L_4/L_5$  regions but utilized ballistic transfers techniques.

What makes the Sun-Earth triangular Lagrange point regions interesting is the linear stability applied to objects that end up there. This could be advantageous for spacecraft in the regions to lessen the amount of station keeping cost needed to remain in the locations. Other scientific reasons to travel to the  $L_4/L_5$  locations would be to observe Trojan and other near Earth objects that could be in the locations. There would be ideal locations to observe the Sun from a stereoscopic view if twin spacecraft were located in both the  $L_4$  and  $L_5$  locations.

The Sun-Earth  $L_5$  location is ideal for observing solar storms, and affords as much as 3-5 days early warning prior to hitting Earth. Coronal Mass Ejections (CME's) can also be observed from this location prior to hitting Earth.

### 1.3 Dissertation Organization

This writeup is organized first with the tools developed to analyze the various principle topics utilized in Section 2. This section goes through the three-body problem, definition of the CRTBP and the Jacobi constant derivation. It then follows with similar development of periodic orbits, invariant manifolds and low thrust optimization.

Section 3 then takes the tools and techniques of Section 2 and exercises them. It first looks at the characteristics of the Jacobi constants with different three body systems, then transfers to intersect near Earth objects. Lastly it develops a method of using invariant manifolds to transfer from one periodic orbit to another.

Then Section 4 applies the methods to locate minimal transfer costs over the various techniques and transfer times to transit to the Sun-Earth triangular Lagrange point regions. Finally Section 5 summarizes the results.

## **CHAPTER 2**

### **TRANSPORT METHODS**

This chapter describes the tools developed as the baseline methods to analyze the different transport methods of this research. These tools describe how the transport can work or the method used to develop the design.

The fundamental principles utilized in this research stem from the characteristics of low energy transfers. The backbone for much of this research is derived from the three-body problem, and in particular the circular restricted form of this system. From this, equilibrium points, invariant manifolds and periodic trajectories can be developed and utilized in various transport designs. Another form of low energy transfer is developed from the low thrust characteristics of high specific energy engines. The long duration transfer times can lead to variations of transfers requiring low energy costs.

The development of these types of tools for low energy transport is shown in the following sections.

#### **2.1 The Circular Restricted Three-Body Problem (CRTBP)**

The following sections describe, in summary, the basic dynamical problem used for much of the analysis in this report. The applications and unique features of this problem are described, and the pieces and tools used in the analysis are described in the next sections.

##### **2.1.1 Summary of the Three-Body Problem**

The full three-body problem includes three masses whose motion is based on the mutual gravitation of all three bodies. Under no restrictions each mass may

be of any shape and size and the type of the orbits about each other may be of any shape. When studying small bodies (e.g. a man made spacecraft, or an asteroid or comet) in the vicinity of the solar system planets as they both orbit about the even larger Sun, analysis of these objects generally falls into the category of the three-body problem. Based on these relative sizes, two simplifications may be made in the problem.

First, the mass of the minor body may be assumed to be negligible such that its mass won't affect the orbits of the two larger bodies about themselves. This can be easily realized as the masses of all known spacecraft and asteroids are much smaller in comparison to the solar system planets. This contributes greatly to the simplification of the problem. Second, it is assumed that two larger bodies, or primary masses orbit their barycenter in circular orbits. This is reasonable since a quick glance at the eccentricities of nearly all the planets show them to be in nearly circular orbits about the Sun.

The application of these two simplifications to the full three-body problem is known as the Circular Restricted Three-Body Problem (CRTBP). It is considered a three-body problem because of the three total bodies. Restricted in that the mass of the smallest (third) body (the spacecraft, asteroid or minor object in this case) is considered negligible. And circular in that the two primary bodies, the Sun and one of the planets in this case, are considered to be in a circular orbit about each other. This setup can be used to model the motion of a spacecraft, asteroid, or other small body in the presence of two larger bodies.

### 2.1.2 Definition of the CRTBP

For the purposes of studying minor objects in the solar system, the CRTBP includes the following assumptions, described by many in the past, but in particular following the derivation by Szebehely (1967):

- $M_1$  (Sun)  $> M_2$  (planet)  $\gg M_3$  (spacecraft or asteroid)
- $M_1$  and  $M_2$  orbit their barycenter in circular orbits
- Gravity is the only force involved and the bodies are all point masses

In a two-body system the most common way to view the motion of the bodies is in the inertial frame. In the three-body system the most common way to view the motion of the third body is in the rotating, or synodic frame. In this frame the two primary bodies hold still relative to the coordinate axes. The rotating system is described as follows:

- Synodic frame rotates with the motion of the two primary bodies, that is in a counter-clockwise fashion relative to the inertial frame
- Origin is centered at the barycenter of the two primary bodies
- x-axis extends from the origin through  $M_2$
- z-axis extends in the direction of the angular momentum
- y-axis completes the right-hand triad

It is convenient to define a normalized mass ratio constant,  $\mu$ , as

$$\mu = \frac{M_2}{M_1 + M_2} \quad (2.1)$$

The constant  $\mu$  is generally very small for any three-body system in the solar system. Using Equation (2.1), several three-body parameters can be normalized as follows:

- Total mass ( $M_1 + M_2$ ) = 1
- Mass of larger primary =  $1 - \mu$
- Mass of smaller primary =  $\mu$
- Distance between the two primary masses = 1
- Location of larger primary ( $M_1$ ) =  $[-\mu, 0]$
- Location of smaller primary ( $M_2$ ) =  $[1-\mu, 0]$
- G, Gravitational Parameter = 1
- Orbital period of two primaries =  $2\pi$

Normalizing the CRTBP is useful in that the only variable parameter in moving between one three-body system and another is the mass ratio,  $\mu$ .

### 2.1.3 Equations of Motion

The normalized equations of motion for the third body in the rotating (synodic) frame are equal to (Szebehely, 1967):

$$\begin{aligned}
 \ddot{x} &= 2\dot{y} + x - (1 - \mu) \frac{x + \mu}{r_1^3} - \mu \frac{x - 1 + \mu}{r_2^3} \\
 \ddot{y} &= -2\dot{x} + y - (1 - \mu) \frac{y}{r_1^3} - \mu \frac{y}{r_2^3} \\
 \ddot{z} &= -(1 - \mu) \frac{z}{r_1^3} - \mu \frac{z}{r_2^3}
 \end{aligned} \tag{2.2}$$

where  $r_1$  and  $r_2$  are equal to the distance from the third body to the larger and smaller primaries, respectively:

$$\begin{aligned} r_1^2 &= (x + \mu)^2 + y^2 + z^2 \\ r_2^2 &= (x - 1 + \mu)^2 + y^2 + z^2 \end{aligned} \quad (2.3)$$

In this form it is clear that the dynamics of the system depend only on the mass ratio,  $\mu$ . It is also seen that when  $\mu$  goes to zero (when  $M_2$  goes to zero) the dynamics of the system approach the two-body dynamics, albeit in a rotating frame.

#### 2.1.4 Jacobi Integral of Motion

The dynamics of the CRTBP permit an integral of motion to exist in the synodic reference frame, namely the Jacobi constant,  $C$ :

$$C = 2U - V^2 \quad (2.4)$$

where

$$\begin{aligned} U &= \frac{1}{2}(x^2 + y^2) + \frac{1 - \mu}{r_1} + \frac{\mu}{r_2} \\ V^2 &= \dot{x}^2 + \dot{y}^2 + \dot{z}^2 \end{aligned} \quad (2.5)$$

The Jacobi constant, also known as the Jacobi energy or the Jacobi integral of motion, is typically only considered in normalized units. It is nontrivial to convert from the normalized units to SI units. The Jacobi constant is an important parameter to consider because the motion of a particle with a certain Jacobi



constant may be bound within a certain space and can only transfer out of that region using some sort of nonconservative maneuver.

The Jacobi constant in the three-body system relates non-dimensionally to orbit energy in the two-body system. Larger values of  $C$  correspond to lower two-body energies. Knowing the relationship between energy and orbit parameters in the two-body system, a corresponding mapping to the relationship between the Jacobi constant orbit in the three-body system is a feature to be explored throughout this study.

### 2.1.5 Zero-Velocity Curves

Forbidden regions can be identified in the CRTBP by mapping the Jacobi constant throughout the neighborhood of the primary bodies for particles that are at rest in the synodic frame. Each contour of such a map shows a curve that has a constant value of  $C$  at zero-velocity. Each of these curves is known as a zero-velocity curve, and is calculated using:

$$2U = C \quad (2.6)$$

The motion of a particle that has a given Jacobi constant value is bound within its zero-velocity curve and is forbidden from traveling beyond that curve in the synodic frame. As an example, Figure 2-1 shows the zero-velocity curves for the Jacobi constants corresponding to the  $L_1$  and  $L_2$  equilibrium points in the Sun-Neptune (S-N) system. These figures are blown up around the second primary object (Neptune) in the rotating frame and show the forbidden regions in white. It is seen that as the Jacobi constant is decreased the forbidden region opens up

around the  $L_1$  point allowing particles to travel from around the second primary into the interior of the Sun-Neptune system.

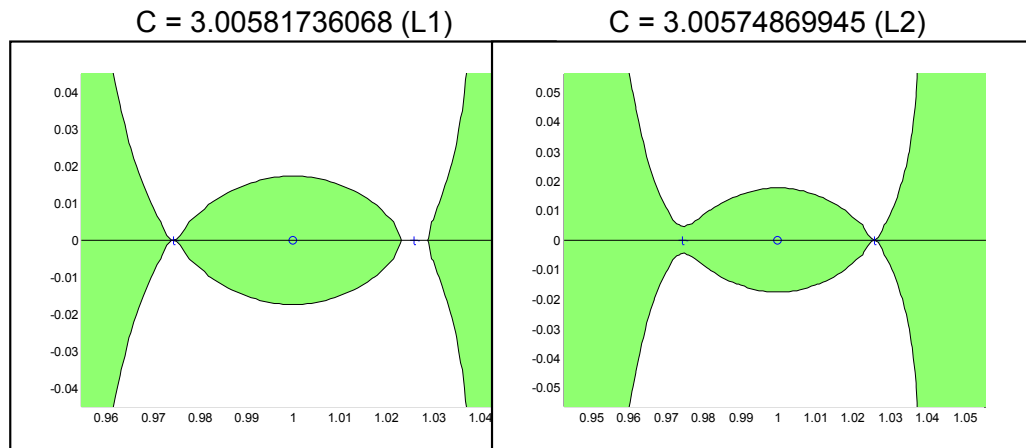


Figure 2-1. Zero-velocity curves for the Sun-Neptune system, with Jacobi constant values corresponding to the equilibrium  $L_1$  (left) and  $L_2$  (right) points.

## 2.2 Periodic Orbits

Periodic orbits in the CRTBP are orbits that repeat periodically about some axis in the rotating frame. They are not conic and do not exist in the two-body system. But real missions use them for various types of mission designs. Many families of periodic orbits exist in the CRTBP, including families that exist around each of the equilibrium Lagrange points, each of the primaries, and even around the entire system (Szebehely, 1967).

In the rotating frame of the CRTBP the small third body can travel along paths that appear to orbit around various places. Certain of these paths can return to nearly the same position and velocity in a repeatable fashion and are referred to as being periodic orbits in the synodic frame. While they may appear to be non-repeatable in the two-body frame, the localized manner of the movement in the

rotating frame can lead to desirable mission designs when interested in equilibrium points in the three-body realm. The following sections describe one method of determining certain periodic orbits near the Lagrange points.

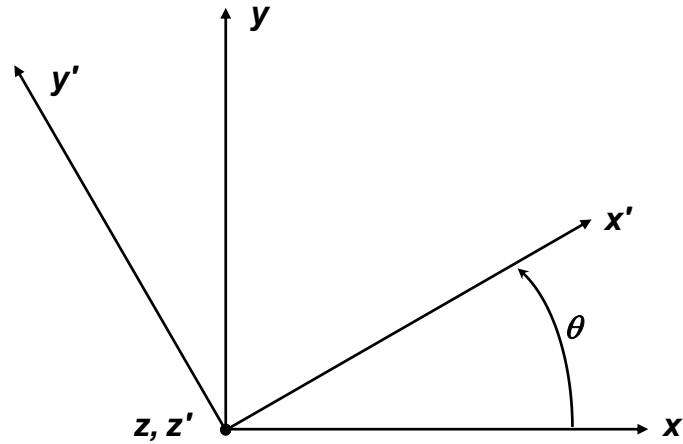
### 2.2.1 Construction of Periodic Orbits in the CRTBP

There are many varieties and categories of quasi-periodic and periodic orbits in the CRTBP, and many analyses exist on their behavior. This report relies primarily on periodic halo orbits about one of the equilibrium Lagrange points in the CRTBP, typically  $L_1$  or  $L_2$ .

The quasi-periodic orbits are often referred to as Lissajous orbits, named for the resemblance to the rectangular constrained harmonic motion curves investigated in detail by Jules Antoine Lissajous as far back as 1857. These Lissajous orbits are located in three-space, and can drift away from periodicity due to slight instabilities. The periodic form of the Lissajous orbits are usually referred to as halo orbits, and are also in three-space. In particular, periodic halo orbits that are located only in the  $x - y$  rotating plane of the primary masses are referred to as Lyapunov orbits and are the primary version analyzed throughout this study.

The halo orbits are a function of the mass ratio of the primary bodies,  $\mu$ , and tend to increase in size with increasing  $\mu$ . The orbits will be restricted to the plane of the two primaries for this analysis, which is the  $x - y$  plane in the rotating frame. The common method of differential correction is used to construct periodic orbits in the CRTBP, as described in the paper by Howell (1984). This method expands on that technique to apply the shooting method about any radial axis in the rotating CRTBP plane.

If we define a rotated frame (prime) from the inertial frame (un-primed), it acts as a randomly rotated frame in the three-body planar rotating system. The primed axis is then the basis of the shooting technique to find the periodicity about.



Basic rotational coordinate transformation:

$$\begin{bmatrix} x' \\ y' \\ z' \end{bmatrix} = \begin{bmatrix} \cos \theta & \sin \theta & 0 \\ -\sin \theta & \cos \theta & 0 \\ 0 & 0 & 1 \end{bmatrix} \begin{bmatrix} x \\ y \\ z \end{bmatrix} \quad (2.7)$$

$$\begin{bmatrix} x \\ y \\ z \end{bmatrix} = \begin{bmatrix} \cos \theta & -\sin \theta & 0 \\ \sin \theta & \cos \theta & 0 \\ 0 & 0 & 1 \end{bmatrix} \begin{bmatrix} x' \\ y' \\ z' \end{bmatrix} \quad (2.8)$$

Assume the following properties:

Invariant under  $y' \rightarrow -y'$

Invariant under  $t \rightarrow -t$

Symmetric about  $x' - z'$  plane

Intersect  $x'$  axis exactly twice per orbit

When crossing the  $x' - z'$  plane the periodic orbit will have the following properties:

Position components in  $x'$  and  $z'$  directions

Velocity only in the  $y'$  direction

Thus,

$$\bar{X}'_0 = [x'_0, 0, z'_0, 0, \dot{y}'_0, 0]^T \quad (2.9)$$

For this, the orbit will be periodic if at  $\frac{T}{2}$  another perpendicular  $x' - z'$  plane crossing may be found. Then,

$$\bar{X}'_{\frac{T}{2}} = [x', 0, z', 0, \dot{y}', 0]^T \quad (2.10)$$

This would then be considered periodic if at  $\frac{T}{2}$  the magnitudes of both  $|\dot{x}'|$  and  $|\dot{z}'| < \epsilon$ , where typically  $\epsilon = 10^{-8}$

If at  $\frac{T}{2}$  the magnitudes of both  $|\dot{x}'|$  and  $|\dot{z}'|$  are too large the initial conditions should be corrected by:

$$\delta \bar{X}'_0 = [\delta x'_0, 0, \delta z'_0, 0, \delta \dot{y}'_0, 0]^T \quad (2.11)$$

Now,

$$y' \left( \frac{T}{2} \right) \approx 0 \quad (2.12)$$

Therefore, the only desired changes to the final state at  $\frac{T}{2}$  are:

$$\begin{aligned} \delta \dot{x}' &= -\dot{x}' \\ \delta \dot{z}' &= -\dot{z}' \end{aligned} \quad (2.13)$$

Utilize the state transition matrix,  $\Phi$ , to make adjustments by relating the state at the half period to the initial state, or  $\bar{X}' \left( \frac{T}{2} \right)$  to  $\bar{X}'(0)$ . Then

$$\delta \bar{X}' \cong \Phi \left( \frac{T}{2}, 0 \right) \delta \bar{X}'_0 + \frac{\partial \bar{X}'}{\partial t} \delta \left( \frac{T}{2} \right) \quad (2.14)$$

Or

$$\begin{bmatrix} \delta x' \\ \delta y' \\ \delta z' \\ \delta \dot{x}' \\ \delta \dot{y}' \\ \delta \dot{z}' \end{bmatrix} \cong \begin{bmatrix} \phi_{11} & \dots & \phi_{16} \\ \vdots & \ddots & \vdots \\ \phi_{61} & \dots & \phi_{66} \end{bmatrix} \left( \frac{T}{2} \rightarrow 0 \right) \begin{bmatrix} \delta x'_0 \\ \delta y'_0 \\ \delta z'_0 \\ \delta \dot{x}'_0 \\ \delta \dot{y}'_0 \\ \delta \dot{z}'_0 \end{bmatrix} + \begin{bmatrix} \dot{x}' \\ \dot{y}' \\ \dot{z}' \\ \ddot{x}' \\ \ddot{y}' \\ \ddot{z}' \end{bmatrix} \delta \left( \frac{T}{2} \right) \quad (2.15)$$

From (2-11) it is seen that  $\delta y'_0 = 0$ , then from (2-15)

$$\delta y' = \phi_{21} \delta x'_0 + \phi_{23} \delta z'_0 + \phi_{25} \delta \dot{y}'_0 + \dot{y}' \delta \left( \frac{T}{2} \right) = 0 \quad (2.16)$$

If desired change is only in  $z'_0$  and  $\dot{y}'_0$ , leave  $x'_0$  fixed (and thus  $\delta x'_0 = 0$ ). Then the expression for the resultant change in the rotated velocities in  $x'$  and  $z'$  from (2.16) is

$$\begin{bmatrix} \delta \dot{x}' \\ \delta \dot{z}' \end{bmatrix} \cong \begin{pmatrix} \phi_{43} & \phi_{45} \\ \phi_{63} & \phi_{65} \end{pmatrix} \begin{pmatrix} \delta z'_0 \\ \delta \dot{y}'_0 \end{pmatrix} + \delta \left( \frac{T}{2} \right) \begin{pmatrix} \ddot{x}' \\ \ddot{z}' \end{pmatrix} \quad (2.17)$$

But, solving for  $\delta \left( \frac{T}{2} \right)$

$$\delta \left( \frac{T}{2} \right) = -\frac{1}{\dot{y}'} (\phi_{23} \quad \phi_{25}) \begin{pmatrix} \delta z'_0 \\ \delta \dot{y}'_0 \end{pmatrix} \quad (2.18)$$

Then (2.17) becomes, after substitution and rearranging to find the initial changes in  $z'$  and  $\dot{y}'$

$$\begin{bmatrix} \delta z'_0 \\ \delta \dot{y}'_0 \end{bmatrix} \cong \left[ \begin{pmatrix} \phi_{43} & \phi_{45} \\ \phi_{63} & \phi_{65} \end{pmatrix} - \frac{1}{\dot{y}'} \begin{pmatrix} \ddot{x}' \\ \ddot{z}' \end{pmatrix} (\phi_{23} \quad \phi_{25}) \right]^{-1} \begin{pmatrix} \delta \dot{x}' \\ \delta \dot{z}' \end{pmatrix} \quad (2.19)$$

Alternatively, if desired change is only in  $x'_0$  and  $\dot{y}'_0$ , leave  $z'_0$  fixed (and thus  $\delta z'_0 = 0$ ). Then the expression for the resultant change in the rotated velocities in  $x'$  and  $z'$  from (2.16) is

$$\begin{bmatrix} \delta \dot{x}' \\ \delta \dot{z}' \end{bmatrix} \cong \begin{pmatrix} \phi_{41} & \phi_{45} \\ \phi_{61} & \phi_{65} \end{pmatrix} \begin{pmatrix} \delta x'_0 \\ \delta \dot{y}'_0 \end{pmatrix} + \delta \left( \frac{T}{2} \right) \begin{pmatrix} \ddot{x}' \\ \ddot{z}' \end{pmatrix} \quad (2.20)$$

But, solving for  $\delta \left( \frac{T}{2} \right)$  with  $\delta z'_0 = 0$

$$\delta \left( \frac{T}{2} \right) = -\frac{1}{\dot{y}'} (\phi_{21} \quad \phi_{25}) \begin{pmatrix} \delta x'_0 \\ \delta \dot{y}'_0 \end{pmatrix} \quad (2.21)$$

Then (2.21) becomes, after substitution and rearranging to find the initial changes in  $x'$  and  $\dot{y}'$

$$\begin{bmatrix} \delta x'_0 \\ \delta \dot{y}'_0 \end{bmatrix} \cong \left[ \begin{pmatrix} \phi_{41} & \phi_{45} \\ \phi_{61} & \phi_{65} \end{pmatrix} - \frac{1}{\dot{y}'} \begin{pmatrix} \ddot{x}' \\ \ddot{z}' \end{pmatrix} (\phi_{21} \quad \phi_{25}) \right]^{-1} \begin{pmatrix} \delta \dot{x}' \\ \delta \dot{z}' \end{pmatrix} \quad (2.22)$$

This method was utilized to generate families of halo orbits about the  $L_1$  and  $L_2$  equilibrium points for the Sun-Earth three-body system. These planar Lyapunov orbits correspond to varying values of the Jacobi constant,  $C$ , which can be used to generate invariant manifolds to transport objects through the three-body system. Examples of some  $L_1$  and  $L_2$  periodic orbits are shown in Figure 2-2 and Figure 2-3.

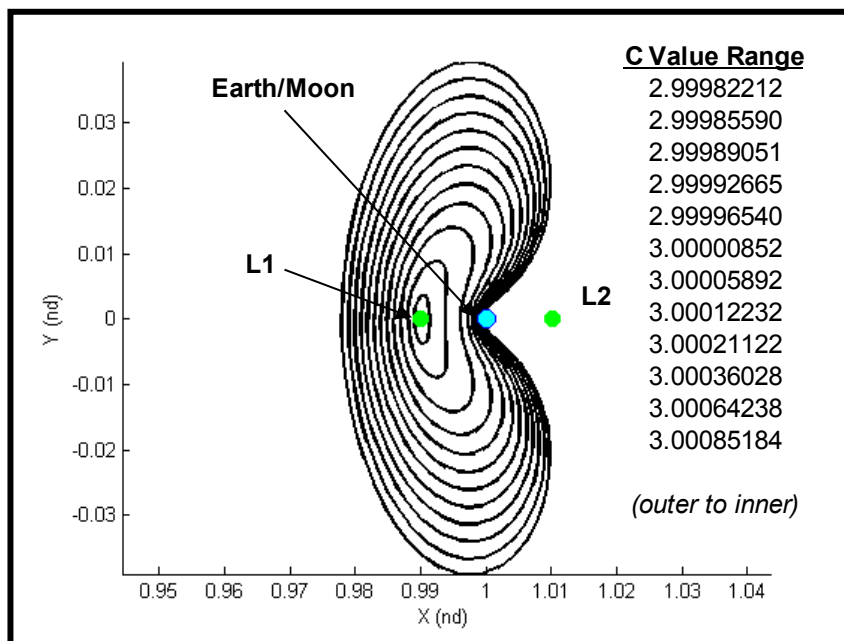


Figure 2-2. Family of Periodic Lyapunov Orbits about the S-E  $L_1$  Equilibrium Point. The Jacobi constants,  $C$ , increase in magnitude the closer to the  $L_1$  centroid they are.

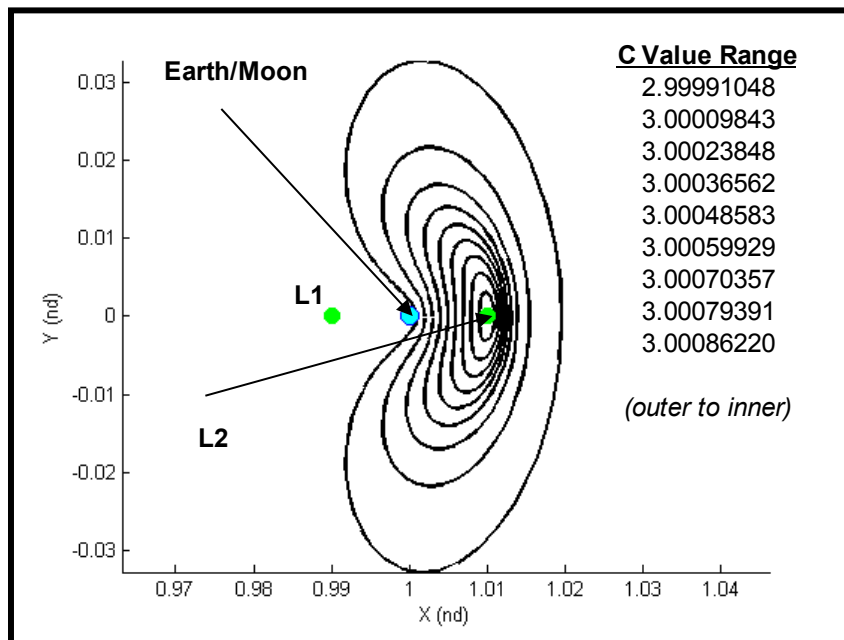


Figure 2-3. Family of Periodic Lyapunov Orbits about the S-E  $L_2$  Equilibrium Point. The Jacobi constants,  $C$ , increase in magnitude the closer to the  $L_2$  centroid they are.



This method can also be utilized to generate families of periodic orbits about axes not coincident with the primary axes, such as the  $L_4$  equilibrium point for the Sun-Earth three-body system. These planar Lyapunov orbits, shown in Figure 2-4 and Figure 2-5, correspond to varying values of the Jacobi constant,  $C$ , which can be used to generate invariant manifolds to transport objects through the three-body system.

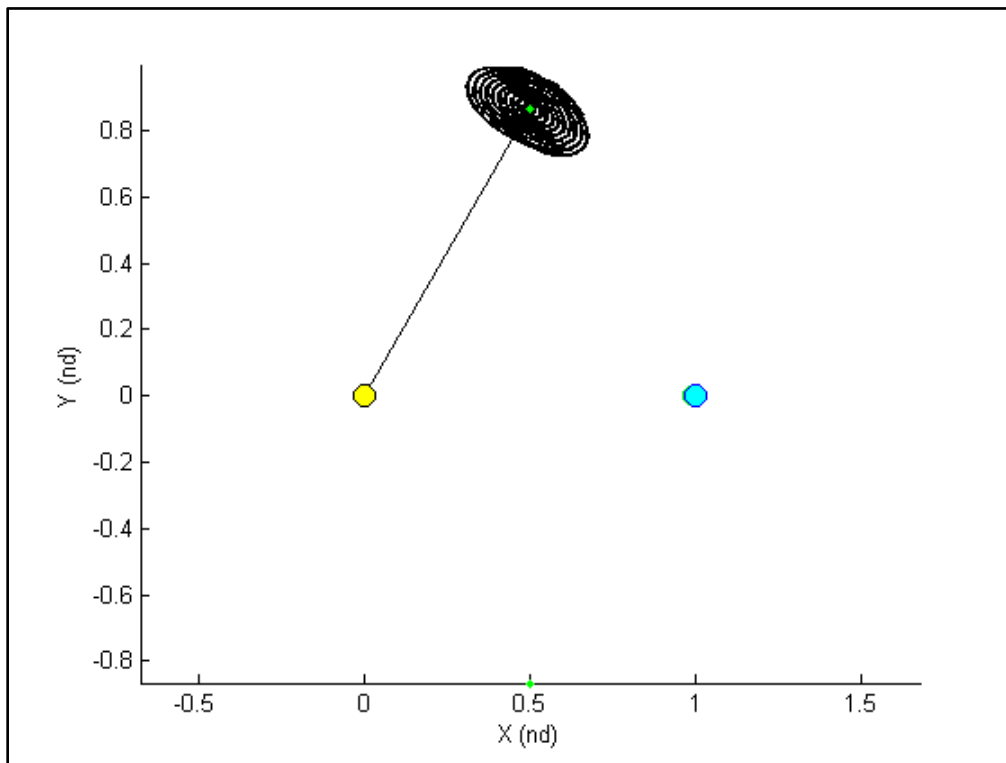


Figure 2-4. Family of Periodic Lyapunov Orbits Concentric about the S-E  $L_4$  Equilibrium Point.

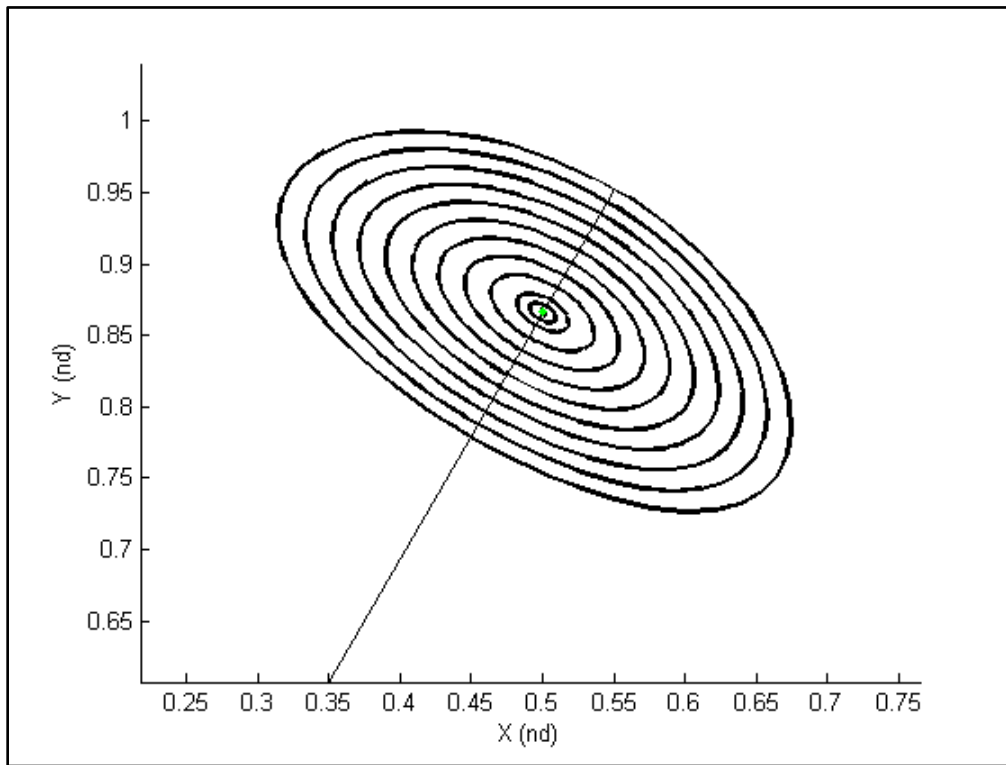


Figure 2-5. Closeup of Family of Periodic Lyapunov Orbits Concentric about the S-E  $L_4$  Equilibrium Point. The Jacobi constants,  $C$ , increase in magnitude the closer to the  $L_4$  centroid they are.

Families of periodic orbits about axes not coincident with the primary axes, such as the  $L_5$  equilibrium point for the Sun-Earth three-body system, are shown in Figure 2-6 and are concentric about the  $L_5$  point.

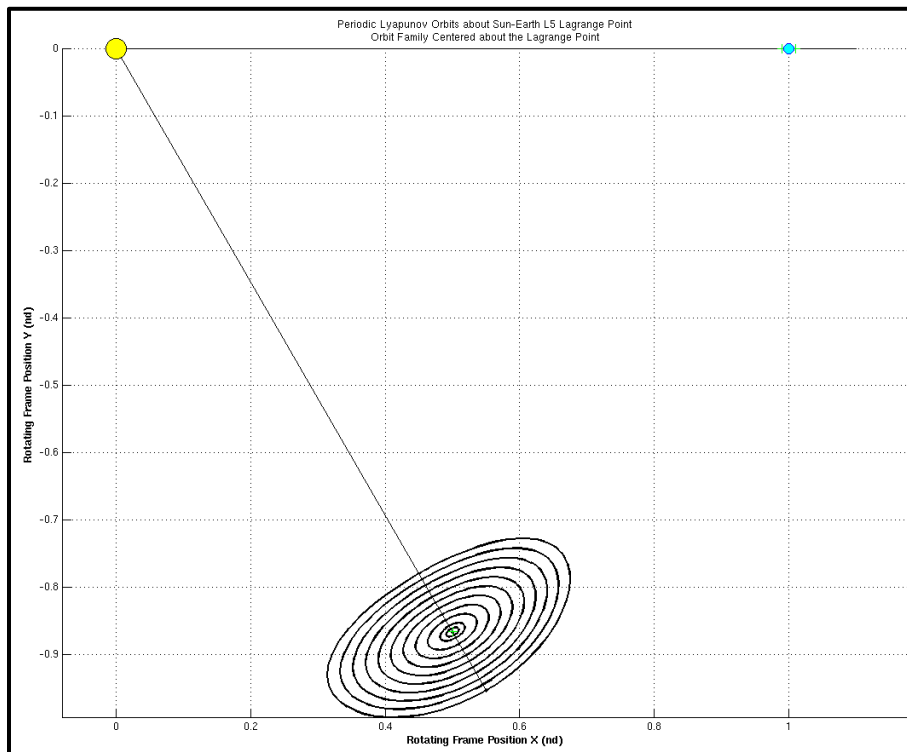


Figure 2-6. Family of Periodic Lyapunov Orbits Concentric about the S-E  $L_5$  Equilibrium Point. The Jacobi constants,  $C$ , increase in magnitude the closer to the  $L_5$  centroid they are.

It is also possible to generate periodic orbits about varying radial axes in the rotating system that correspond to orbits that will intersect one of the triangular Lagrange equilibrium points at one of the apex points in the periodic shape. By choosing the appropriate radial axis angle for the size of the orbit shape a family of periodic orbits that intersect with given triangular equilibrium point can be generated such as those in Figure 2-7 for the S-E  $L_5$  point. Similar families can be generated for the S-E  $L_4$  point in the same manor.

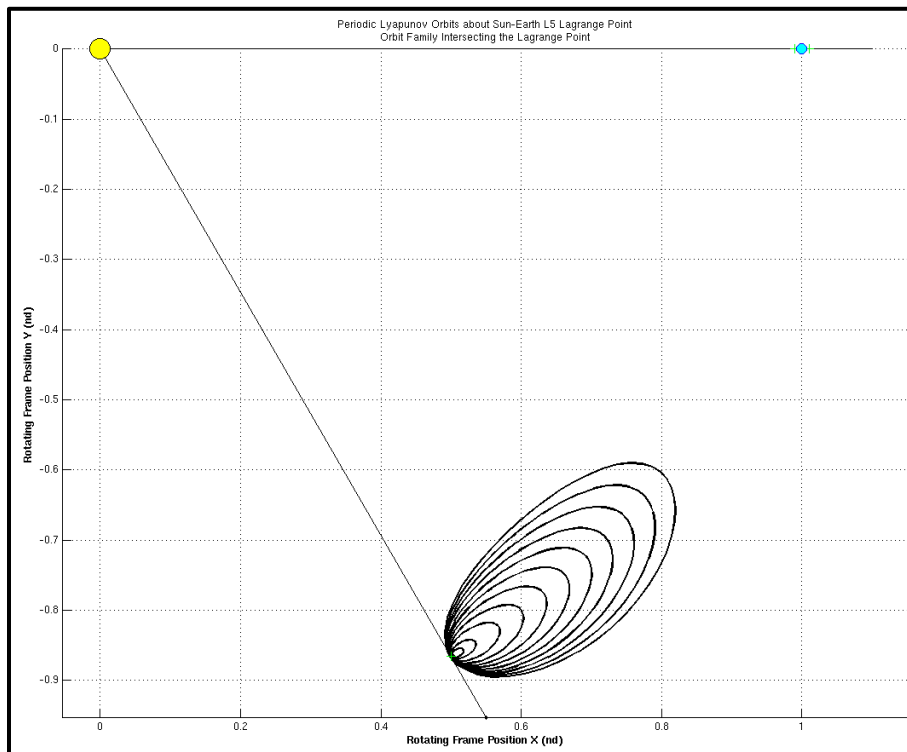


Figure 2-7. Family of Periodic Lyapunov Orbits that Intersect the S-E  $L_5$  Equilibrium Point. These are all periodic about different radial axes, but all go through the  $L_5$  point at the lower apex of their shape.

These families of periodic Lyapunov orbits about the linear Lagrange equilibrium points ( $L_1$  and  $L_2$ ) can be utilized to generate unstable invariant manifolds that can be propagated to the families of periodic Lyapunov orbits about the triangular Lagrange equilibrium points ( $L_4$  and  $L_5$ ). This transport method will be explored in a later section of this document.

## 2.3 Invariant Manifolds

### 2.3.1 Invariant Manifolds of Unstable Periodic Orbits

A manifold is an abstract mathematical space in which every point has a neighborhood which resembles Euclidian space, but in which the global structure may be more complicated. For example, in six-space where there is a velocity vector field for each three-space position, the manifold would be represented by a trajectory of each state propagated through time. The term ‘invariant’ indicates that as any point is propagated through time only one trajectory will be generated and a point on that manifold will remain on the manifold as time evolves.

Invariant manifolds can be categorized as stable or unstable. Mathematically speaking, for continuous time systems the stable and unstable manifolds are defined as:

**Stable Manifold ( $W^s$ ):** The set of initial conditions,  $x_0$ , such that  $x(t) \rightarrow x^*$  as  $t \rightarrow \infty$

**Unstable Manifold ( $W^u$ ):** The set of initial conditions,  $x_0$ , such that  $x(t) \rightarrow x^*$  as  $t \rightarrow -\infty$

where  $x^*$  is a saddle point in the system, or for the CRTBP can be an equilibrium point or a periodic orbit.

Invariant manifolds can be applied to an unstable periodic orbit, such as an unstable halo orbit about an equilibrium point in the CRTBP. An unstable orbit has at least one stable and one unstable eigenvector. An object traveling along an unstable periodic orbit that realizes a small perturbation in the direction of the unstable eigenvector will fall away from this periodic orbit in an exponential fashion

along the unstable invariant manifold. Conversely, if an object is given the correct initial conditions it will travel in an exponential fashion along the stable invariant manifold and eventually approach an unstable periodic orbit from the direction of the stable eigenvector.

To construct the invariant manifolds of an unstable periodic orbit in the CRTBP, the state transition matrix of the orbit is propagated from the initial time ( $t_0$ ) to the time after one period ( $t_0 + T$ ). After being propagated for a full orbit the matrix contains information about every part of the orbit, and is referred to as the monodromy matrix designated as  $\Phi(t_0 + T, t_0)$ .

The eigenvectors of the monodromy matrix can be propagated to any state along the periodic orbit using the state transition matrix. After normalizing the eigenvectors at the desired point to preserve their initial magnitude, a small perturbation in the direction of the unstable eigenvector (with an eigenvalue greater than one) will cause an object to be taken onto the unstable invariant manifold if propagated forward in time. The perturbation can be in the direction of the eigenvector, as just described, or in the negative of the eigenvector direction. One direction typically takes the trajectories toward the second primary object while the other direction will typically cause the object to travel away from the second primary. In a similar fashion, the perturbations can be made along the stable eigenvector direction (with an eigenvalue less than one) causing the object to be taken onto the stable invariant manifold if propagated backward on time.

Figure 2-8 shows the stable and unstable invariant manifolds emanating from a periodic halo orbit about the Sun-Neptune  $L_2$  equilibrium point. The Jacobi constant associated with the periodic orbit is 3.00564142, and the green areas represent the forbidden regions where the manifolds cannot travel to. It is seen that the manifolds have a tubular type formation as a whole and travel both toward

the interior of the system as well as away from the second primary (the light blue dot).

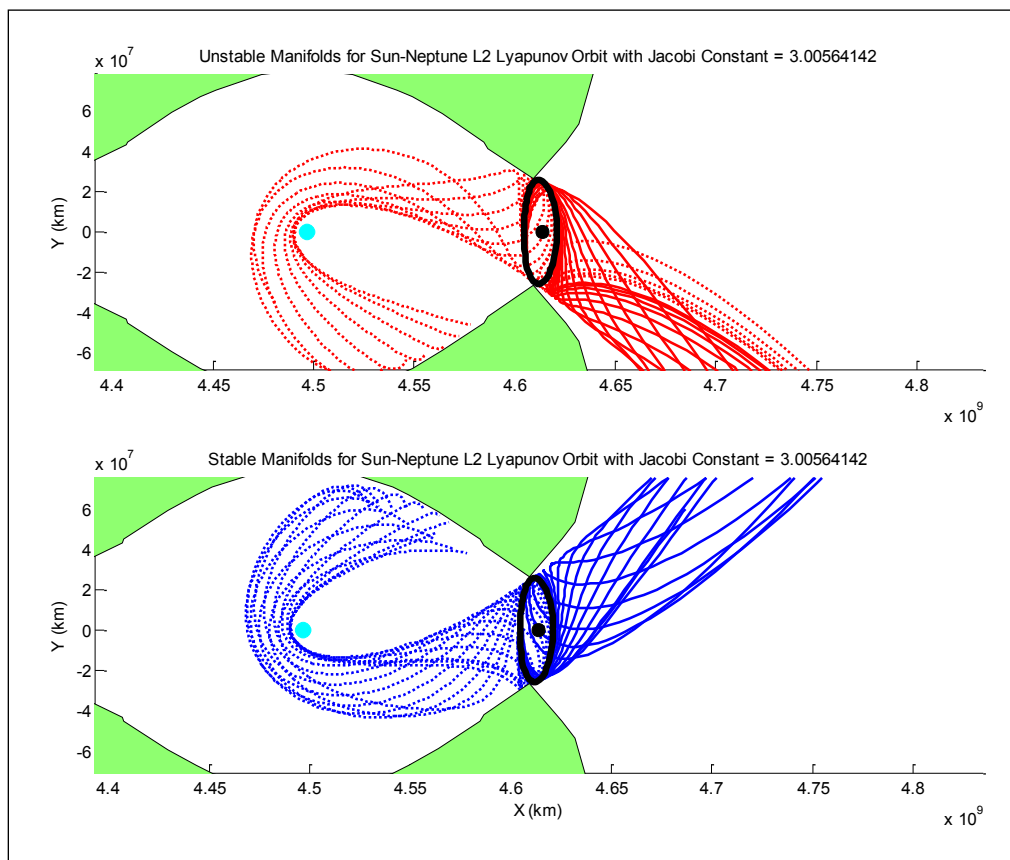


Figure 2-8. The unstable (top) and stable (bottom) invariant manifolds for a periodic orbit about the Sun-Neptune  $L_2$  equilibrium point.

The invariant manifolds of unstable periodic orbits in the CRTBP can be utilized to transport an object from one orbit and into another orbit, or to possibly intersect another object in a separate orbit. With the vast number of possible periodic orbits and the associated manifolds in the CRTBP, and the very small energy cost to get onto these transfers from the periodic orbits, the invariant manifolds are a very interesting tool to use for trajectory mission designs.

## 2.4 Low Thrust

Electric propulsion is becoming very prevalent in space operations and has shown use in interplanetary type missions such as Dawn and Hayabusa. Electric propulsion is synonymous with low-energy as well as low-thrust propulsion. The efficiency of most electric propulsion technologies is very high while the mass flow and resulting thrust is very low.

Modern chemical rocket engines, such as those typically found on larger launch vehicle second stages, can have thrust magnitudes that vary widely, but can be upwards of 100 kN. The specific impulse, or  $I_{sp}$ , values for these engines are in the range of up to 470 sec. Even smaller chemical kick stages used to boost satellite orbits typically have thrust magnitudes upwards of 500 N and  $I_{sp}$  values only up to about 300 sec.

To take full advantage of long transfer times, low energy propulsion can utilize the small size and low propellant weights of typical electric propulsion motors that have specific impulse values in the range of 1600 – 4100 sec, while only requiring thrust magnitudes in the 50 – 250 mN range. Given enough transit time duration to apply the high  $I_{sp}$ /Low thrust to affect the orbit, the low amount of required mass change allows small delta velocity changes to achieve the desired effect. This is controlled by the rocket equation:

$$\Delta v = v_e \ln\left(\frac{m_i}{m_f}\right) = g I_{sp} \ln\left(\frac{m_i}{m_f}\right)$$

Here, the delta velocity change for a given  $I_{sp}$  is directly proportional to the mass ratio across the burn length from start to finish. This is controlled directly by the amount of used propellant.



### 2.4.1 Low Thrust Optimization

To determine the minimal velocity change needed to perform low thrust transfers from the Earth region to the Sun-Earth triangular Lagrange points a Sims-Flanagan (Sims & Flanagan, 1999) and (Sims, Finlayson, Rinderle, Vavrina, & Kowalkowski, 2006) type direct transcription low thrust optimization tool was used. The tool, known as the CCAR Optimal low-Thrust Tool (COLTT), was developed at the Colorado Center for Astrodynamics Research (Herman, 2012) for use by the researches at that facility.

The COLTT tool is able to optimize a wide variety of trajectory parameters including the thrust magnitude, direction and specific impulse. It can utilize constraint parameters such as launch and arrival times and escape C3 values.

This tool utilizes the SNOPT optimization routine (Gill, Murray, & Saunders, Vol. 47, No. 1, 2005) which is an SQP type optimizer. After formulating and scaling the constrained optimal control problem, SNOPT finds a feasible and optimal solution.

### 2.4.2 Optimized Low Thrust Transfer Examples

The following four figures (Figure 2-9 through Figure 2-12) represent examples of low thrust transfers between an Earth escape starting state to the L4 and L5 locations, given various levels of engine Isp and transfer time. The figures show the trajectories in both the rotating and inertial frame, as well as the thrust profile and change in two-body planar orbit parameters. More detail of the low thrust profiles for all the transfer times for various Isp cases are shown in Appendix A.

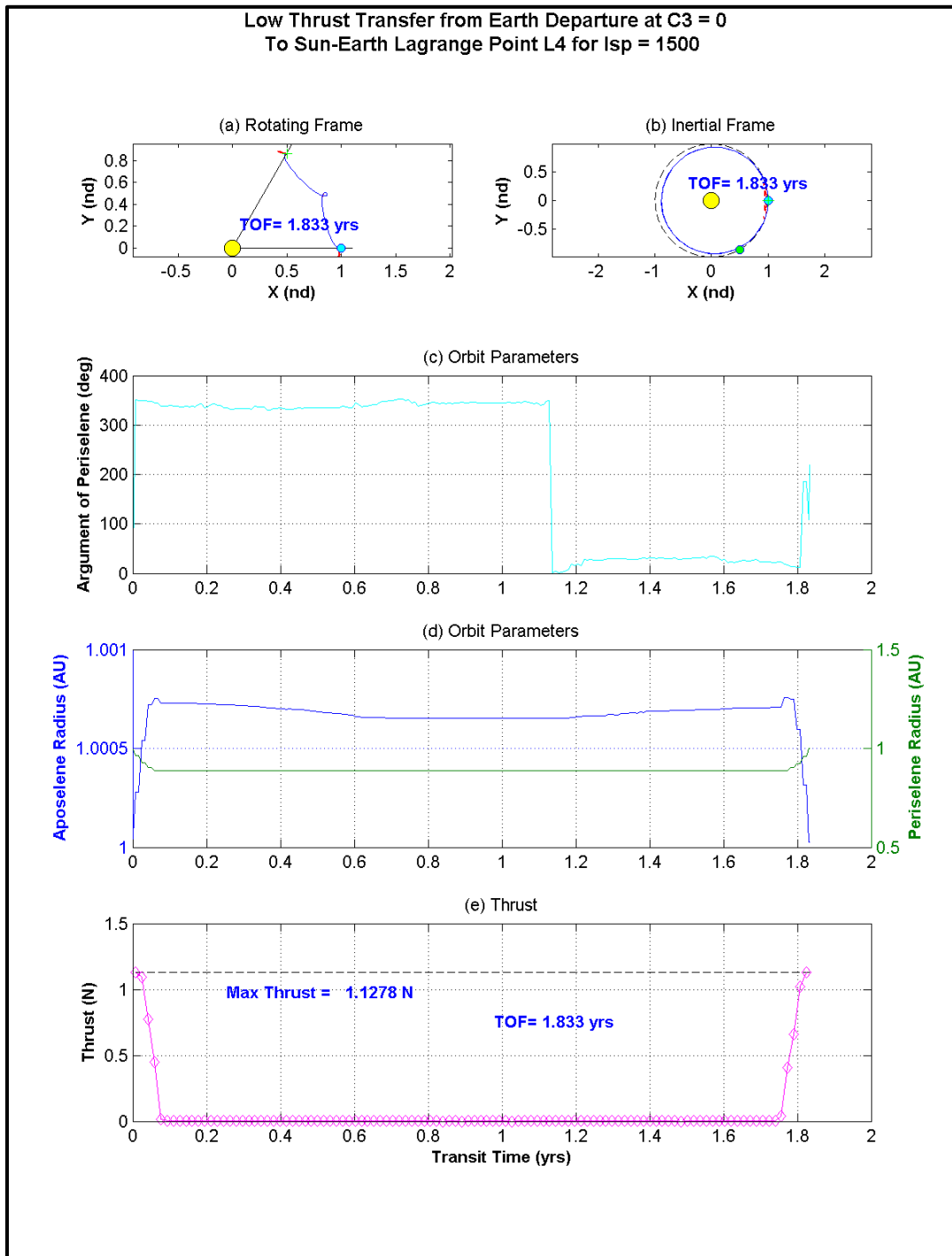


Figure 2-9. Low Thrust Transfer to S-E L<sub>4</sub> for Isp = 1500 s and TOF = 1.833 yrs. This figure shows (a) rotating frame trace, (b) inertial frame trace, (c) argument of perihelion, (d) apohelion and perihelion radii, and (e) thrust profile for this transfer.

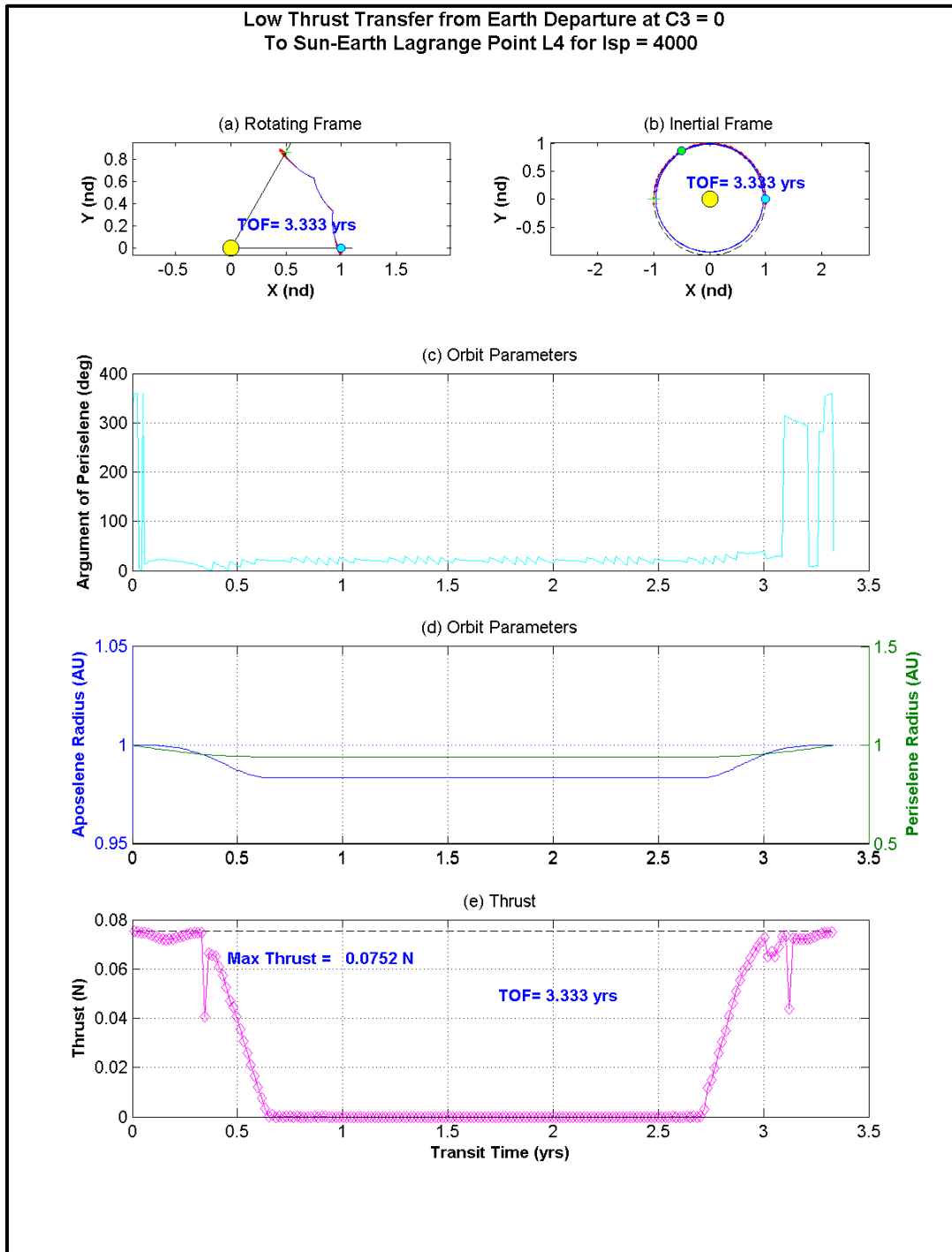


Figure 2-10. Low Thrust Transfer to S-E  $L_4$  for  $I_{sp} = 4000$  s and  $TOF = 3.333$  yrs. This figure shows (a) rotating frame trace, (b) inertial frame trace, (c) argument of perihelion, (d) apohelion and perihelion radii, and (e) thrust profile for this transfer.

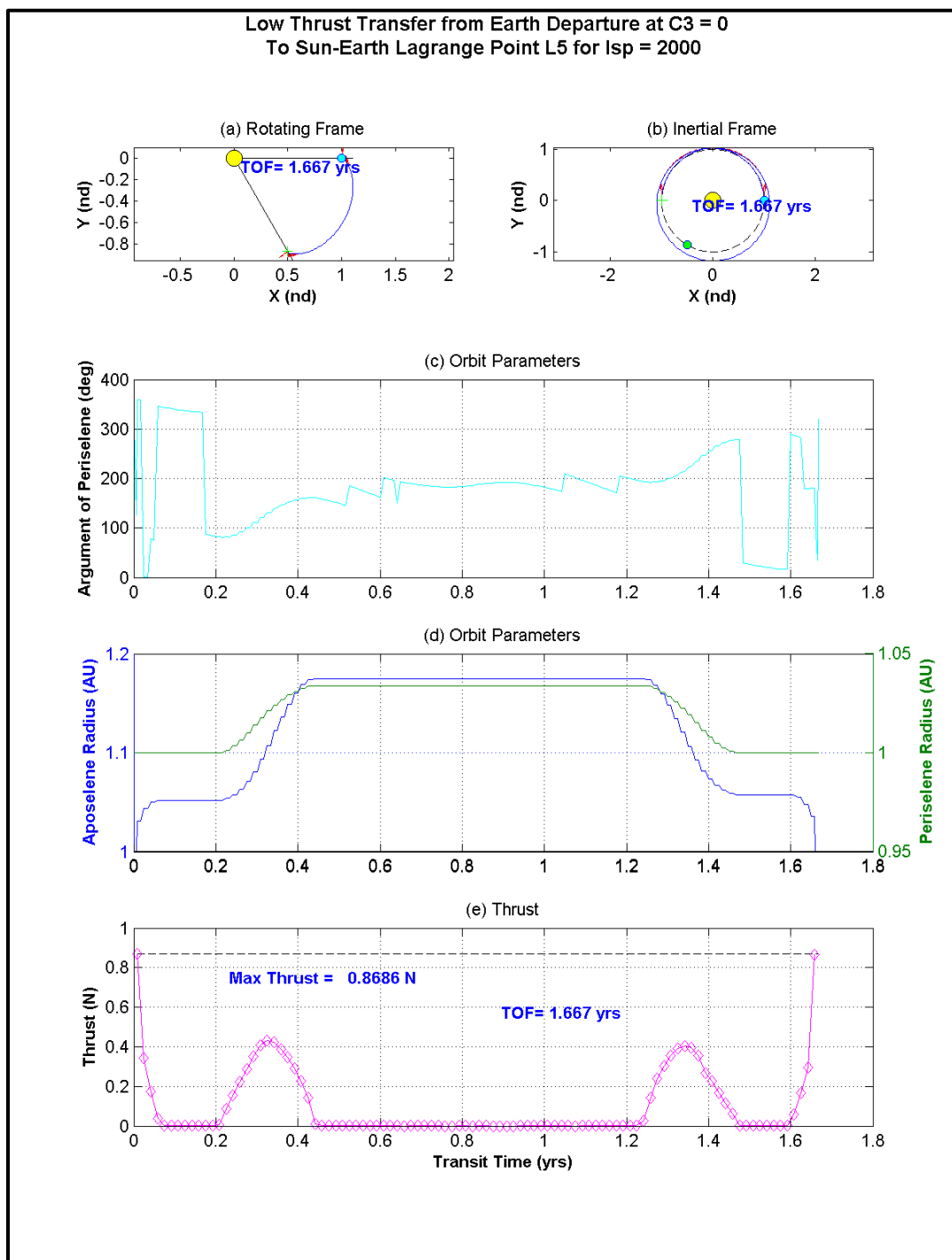


Figure 2-11. Low Thrust Transfer to S-E  $L_5$  for  $I_{sp} = 2000$  s and  $TOF = 1.667$  yrs. This figure shows (a) rotating frame trace, (b) inertial frame trace, (c) argument of perihelion, (d) apohelion and perihelion radii, and (e) thrust profile for this transfer.

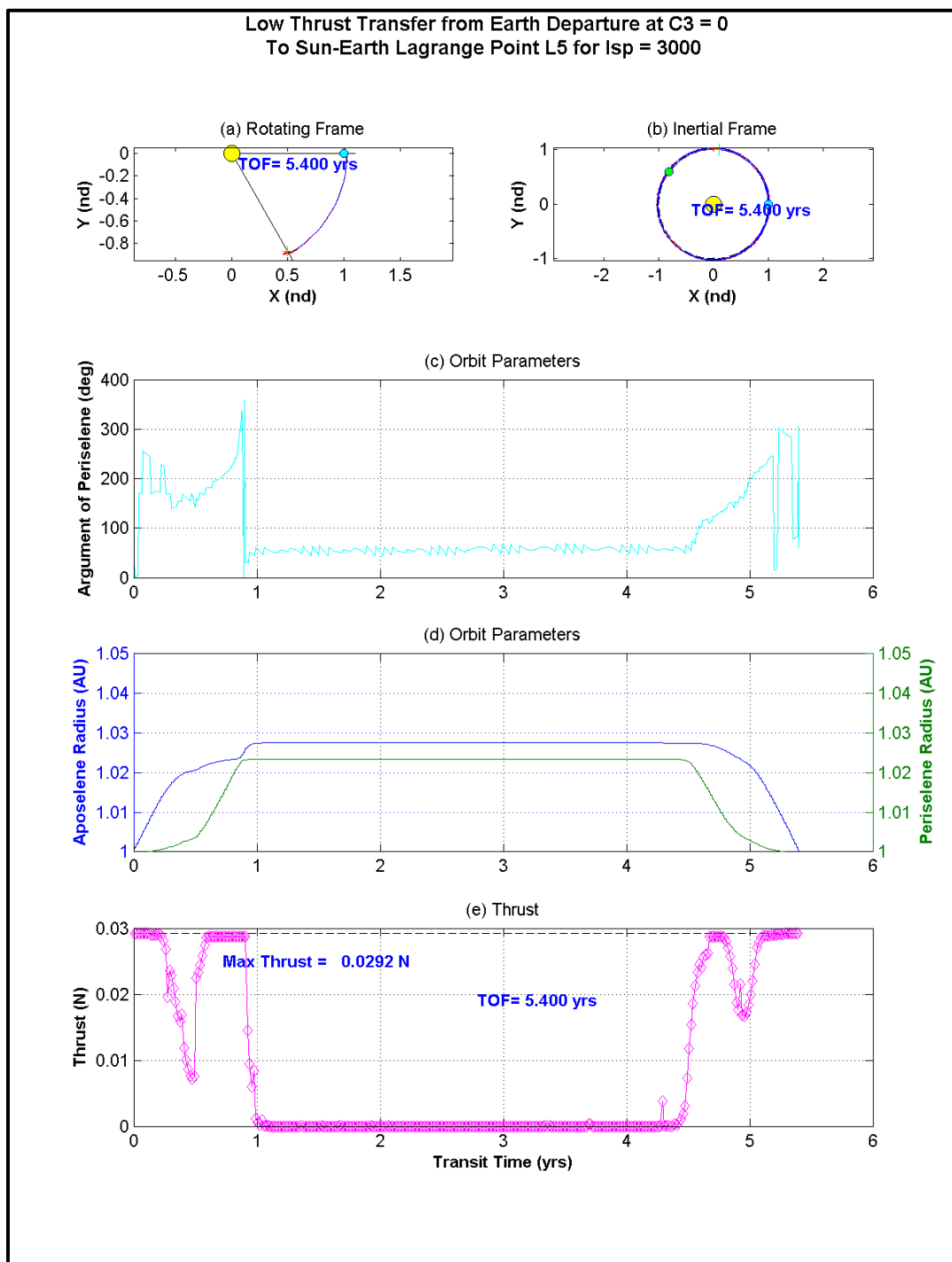


Figure 2-12. Low Thrust Transfer to S-E  $L_5$  for  $I_{sp} = 3000$  s and  $TOF = 5.400$  yrs. This figure shows (a) rotating frame trace, (b) inertial frame trace, (c) argument of perihelion, (d) apohelion and perihelion radii, and (e) thrust profile for this transfer.

## CHAPTER 3

### CHARACTERISTICS OF THE 3-BODY SYSTEM

#### 3.1 Relationships for Different 3-Body Systems

The launch of the New Horizons mission to Pluto and beyond in 2006 began the close up of the Kuiper Belt region. New missions to this region with greater capabilities would greatly enhance the understanding of this part of the solar system and its origins. Potential exists to utilize low energy methods to open up this region of the solar system for exploration. Objects in the outer solar system are vast distances away and current capabilities to send spacecraft to this region is limited. Better understanding of the relationships of the outer planets in the three-body systems with the sun could lead to unique designs for developing trajectories to move about.

This section uses several of the methods from Chapter 2 to both exercise the methods with several different three-body system parameters, and to characterize some of the attributes of periodic orbits and invariant manifold transfers in these systems.

##### 3.1.1 Jacobi Constant Characteristics of KBO's

As described in Section 2.1.4, the Jacobi constant is a dimensionless parameter in the CRTBP that closely relates to the dimensional energy of the orbit of an object in the two-body problem. In the two-body system it is useful to understand the energies of the orbits as you trade kinetic energy for potential energy when transferring from one orbit to another. Therefore it seems prudent to

try and understand the how an objects Jacobi constant is characterized in the CRTBP.

A larger database of Kuiper Belt Objects (KBO's) was extracted from the JPL HORIZONS (Jet Propulsion Laboratory, 2007) system. This is a large database of solar system data and ephemerides for many types of objects, including KBO's. The Kuiper Belt is a region of space containing many small objects from the early solar system formation that orbit the Sun extending from about the orbit of Neptune (approximately 30 AU) to approximately 50 AU from the Sun. One of the largest identified objects in this region is Pluto. It is believed that many objects from the Kuiper Belt get gravitationally pulled inward toward the inner solar system and become objects such as comets, asteroids (those not originating from the main asteroid belt between Mars and Jupiter), centaurs (orbiting between Jupiter and Neptune) and trans-Neptunian Objects (TNO's, any minor body whose semimajor axis is larger than that of Neptune). It is also theorized that most Trojan objects, those that orbit in the vicinity of the leading and trailing equilibrium points of the Sun-planet three body system, generally originate from the Kuiper Belt region.

The states of all the Centaur, Jupiter Trojan, and TNO objects available were used to determine their respective Jacobi constants,  $C$ . Figure 3-1 through Figure 3-3 show the Jacobi constant values for each of the KBO class for the various Sun/outer planet three-body systems.

It is seen from Figure 3-2 that the Jupiter Trojan objects are closely clustered into various values of  $C$  for each of the outer planet systems. Knowing that the Jupiter Trojan objects are essentially located in the same orbit, but leading and trailing Jupiter about the Sun, it seems plausible that these objects would have very similar values of  $C$  with that of Jupiter and that it would be relatively efficient

to transfer orbits between them. This may indicate that a value of  $C$  just above 3.0 for a KBO object in the CRTBP is a favorable value in terms of orbit transfer energy.

The values of  $C$  for the Centaur objects, as seen in Figure 3-1, show them to be near 3.0 as a whole but with a much looser clustering. This seems to indicate that the energy for these objects with respect to nearly all the outer planets is fairly constant. The values of  $C$  for the TNO objects (Figure 3-3) show the familial clustering about a value similar to the Trojans, but there seems to be more of the family values closer to 3.0. This may indicate that it may be more efficient to transfer to these objects from the Uranus, Neptune, or Pluto orbit than from a Jupiter orbit.

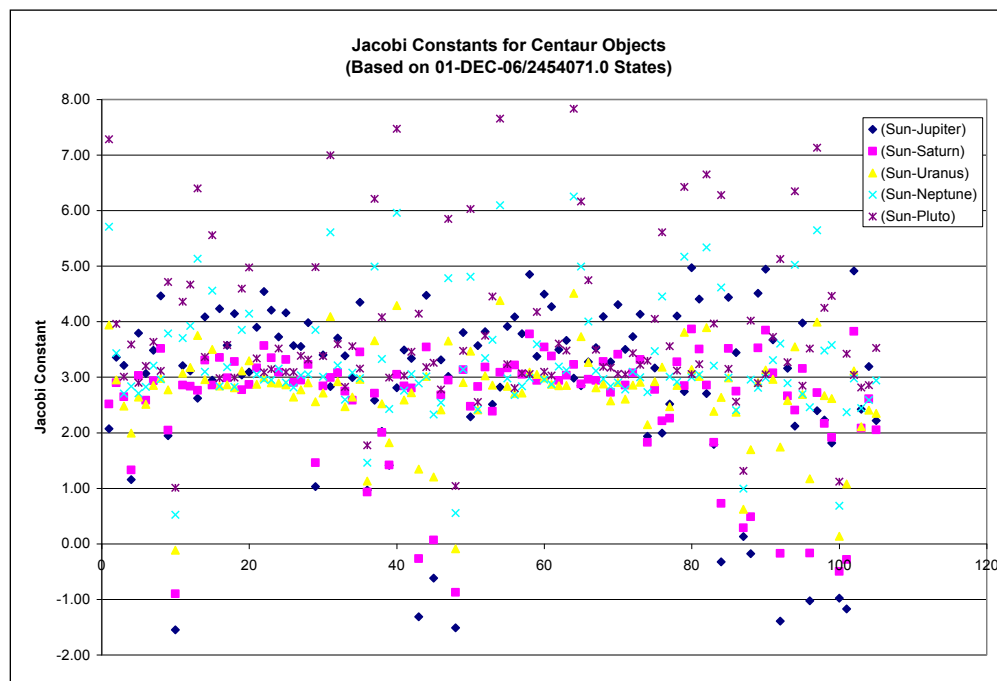


Figure 3-1. Jacobi constant values for Centaur class KBO's for the Sun/outer planet systems.



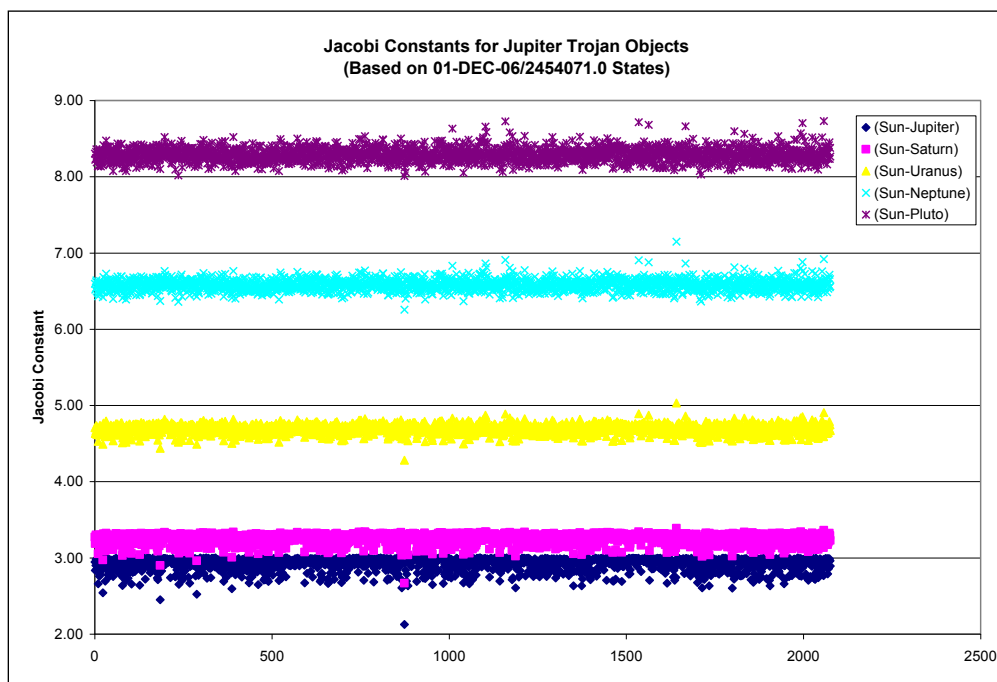


Figure 3-2. Jacobi constant values for Jupiter Trojan class KBO's for the Sun/outer planet systems.

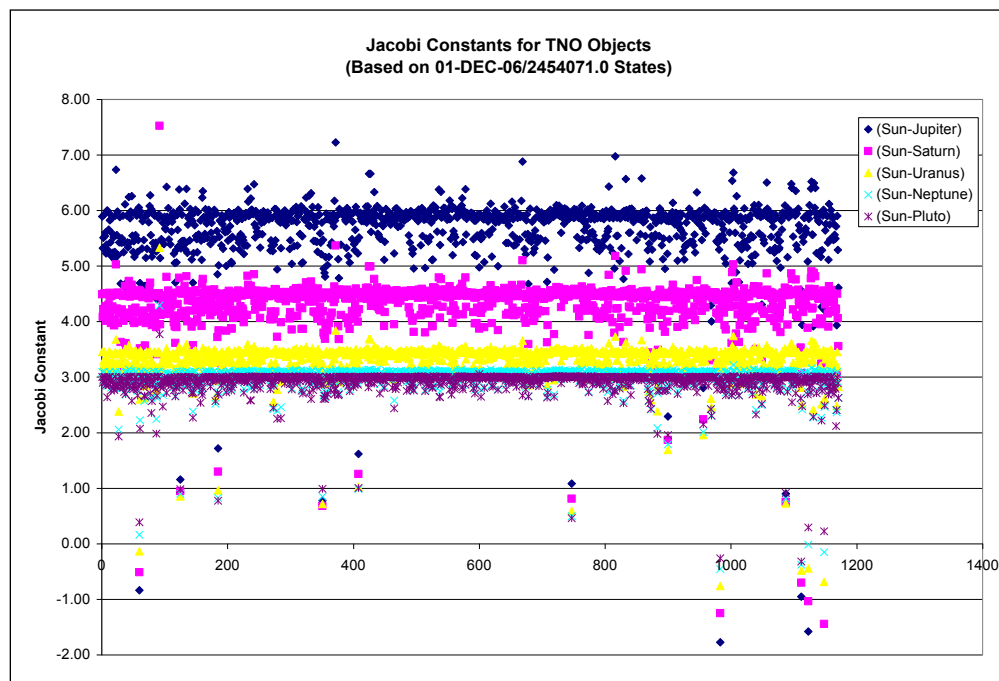


Figure 3-3. Jacobi constant values for TNO class KBO's for the Sun/outer planet systems.

Another way to try and characterize the KBO objects is to compare their Jacobi constant values relative to various orbit parameters in more of a spatial sense relative to the primary body. Figure 3-4 shows the Jacobi constant values for the KBO objects, in the Sun-Neptune system for this example, for six different orbital elements. It is sent as above that the Jupiter Trojan and TNO objects cluster together in tighter families than the Centaur objects.

The Centaur objects seem to be in a much broader and less stable family of orbits. This likely correlates with the theorized origin of Centaur objects themselves, which is that they were originally TNO's that have been pulled into the inner solar system by gravitational interactions with one of the larger planets (Jupiter or Saturn). This generally leaves them in less stable orbits for a period of time until they migrate into more stable regions, such as Trojans. This type of transportation mechanism is beyond the scope of this analysis.

The C values compared with the mean motion of the objects (the lower right figure) seems to have a somewhat linear trend throughout all the KBO objects, but this may be an artifact of the mean motion being directly related to the CRTBP formulation. No other distinguishing characteristics or clear conclusions from this data has surfaced at this time.

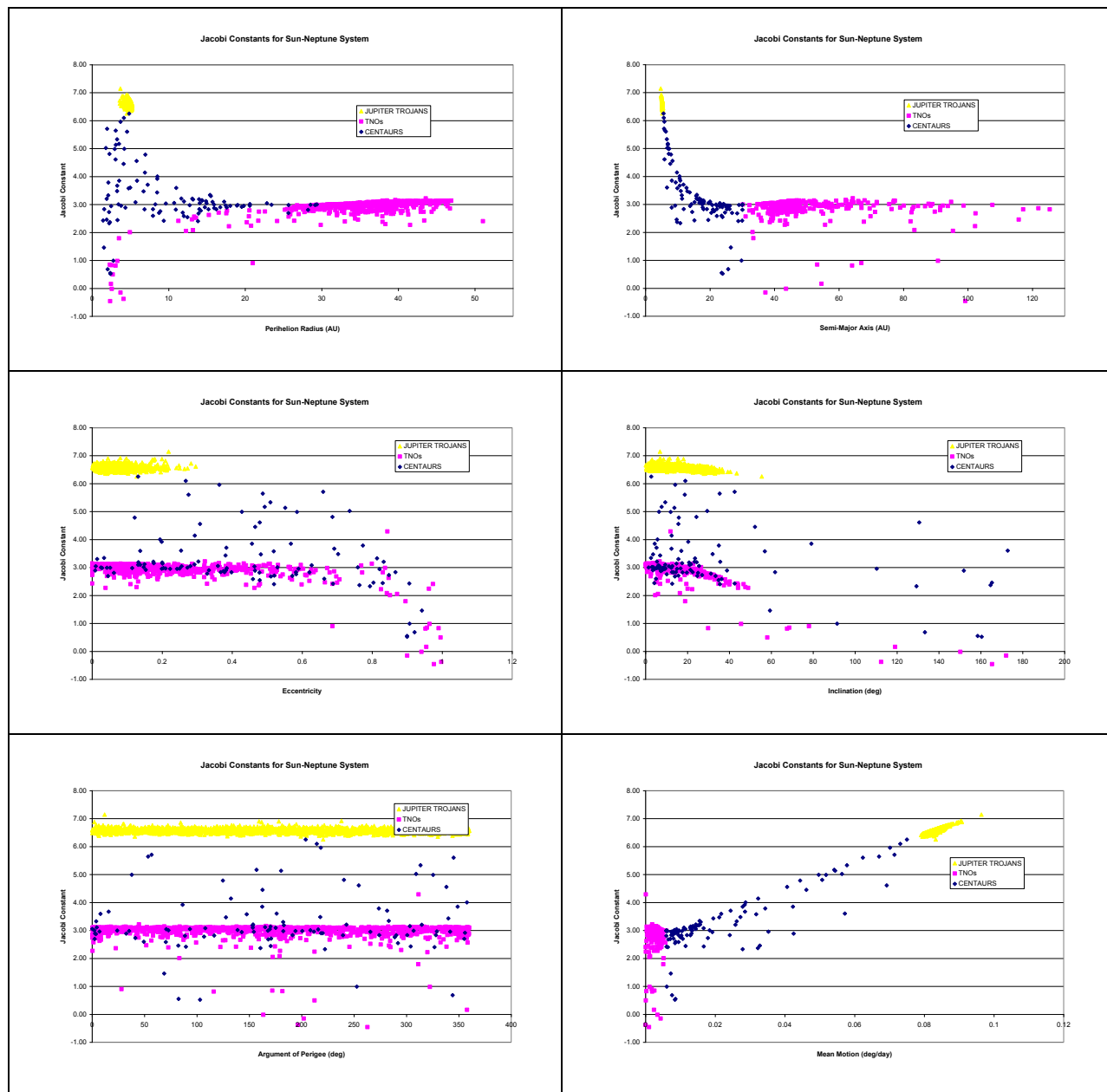


Figure 3-4. Jacobi constant values for the KBO's as a function of various orbital parameters.

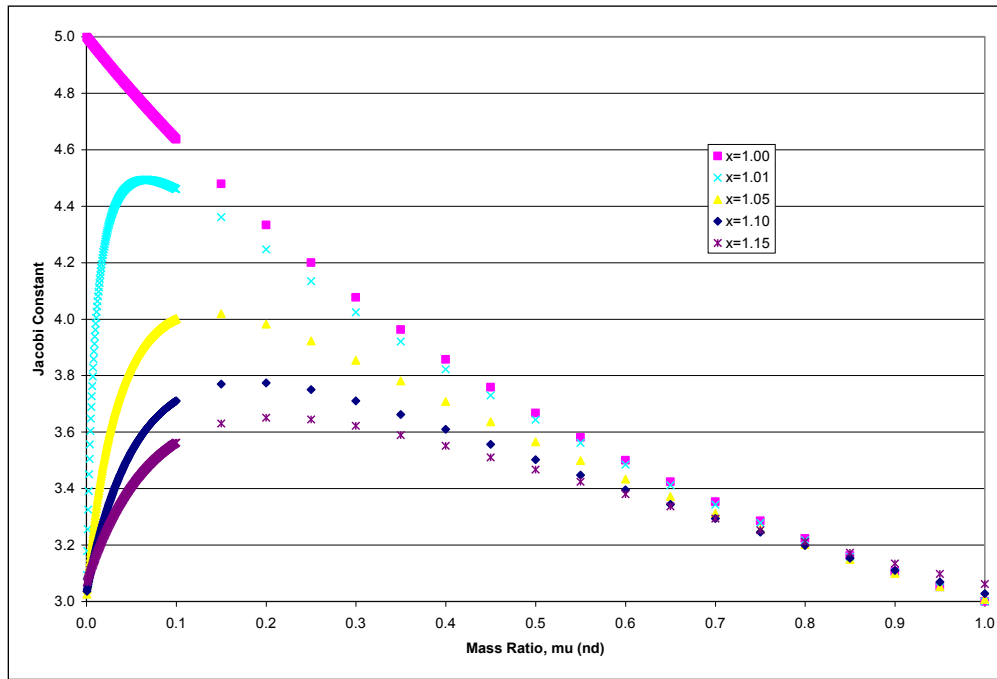
### 3.1.2 Parametric Evaluation of the Jacobi Constant

Another means of characterizing the Jacobi constant is to try and determine what value it should be for the given system from a parametric perspective. For the CRTBP the equation for the Jacobi constant is a function of the mass ratio of the two primary bodies in the system, or  $\mu$ . The mass ratio can range in value from zero to one. Taking this range of values for  $\mu$  and further simplifying the problem by assuming the third-body object is located somewhere along the x-axis with zero velocity in the rotating frame (along the line between the two primaries and rotating at the same angular rate as the second primary), Figure 3-5 shows how the Jacobi constant varies.

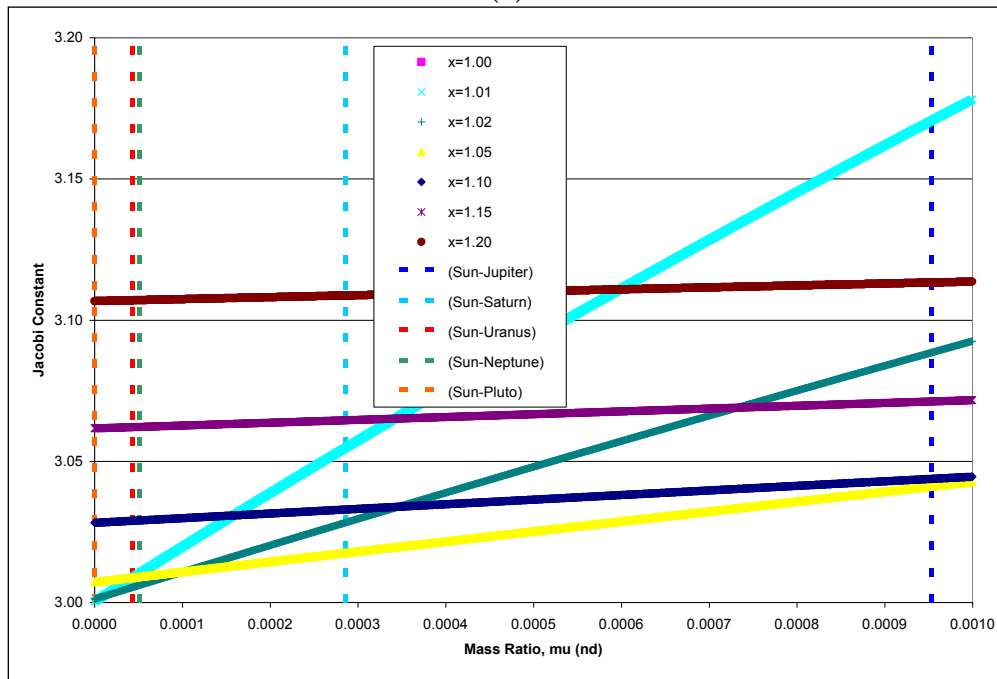
The curves represent various values of the objects location on the x-axis in the rotating frame. It is seen from equations (2.4) and (2.5), as well as in Figure 3-5a, that as  $\mu$  approaches zero (which approximates the two-body problem) the value of C approaches three (although there is the singularity when  $\mu = 0$  and  $x = 1$ ). Also, when  $\mu$  approaches one, the values for C approach three as well.

Figure 3-5b shows a blowup of the region close to where  $\mu = 0$ , and the region where the mass ratio for the Sun/outer planet mass ratios lie. It can be seen from this figure that from a theoretical sense the third-body objects that have a mean motion close to that of the outer planets should have Jacobi constant values near 3.0.

Further analysis on this parameter study could be performed with more broad assumptions to gain more insight, but that will have to be done at a later date.



(a)



(b)

Figure 3-5. Jacobi constant values as a function of mass ratio for a stationary object in the CRTBP.

### 3.1.3 Invariant Manifold Structure vs. Jacobi Constant

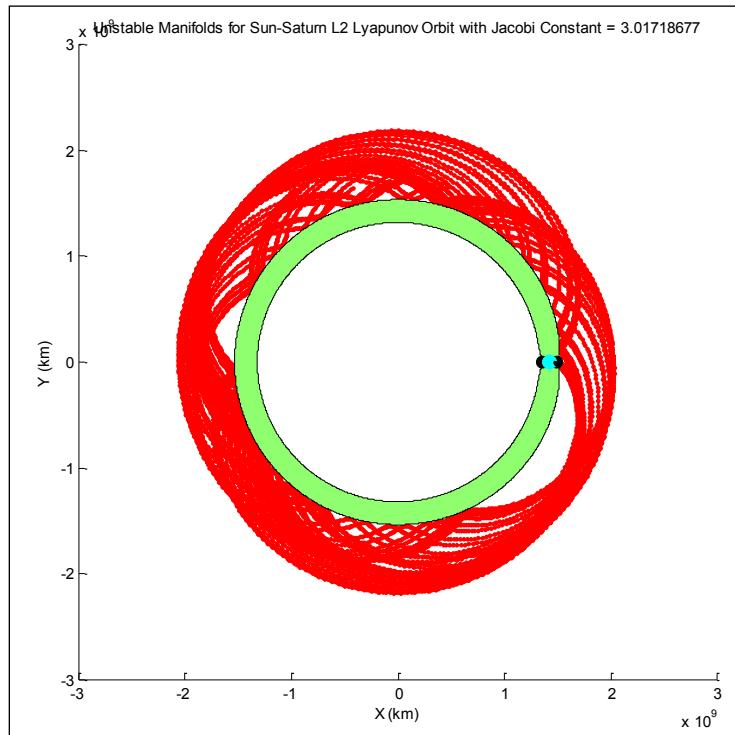
The invariant manifolds propagated from a periodic orbit in the CRTBP take on the Jacobi constant characteristics of that periodic orbit. Therefore it is of benefit to gather insight into the relationship of the given periodic orbit and the characteristic structure of the manifolds that are generated from it. Insight into this relationship can be useful in designing unstable manifolds that will intersect and rendezvous with a target object or its orbit in the most efficient way. A first look at this relationship is shown in Figure 3-6.

This figure shows the unstable manifolds propagating from periodic halo orbits about the  $L_2$  point of the Sun-Saturn system. The three figures have halo orbits with three different Jacobi constants, ranging from 3.01718677 (a) to 2.99934175 (c).

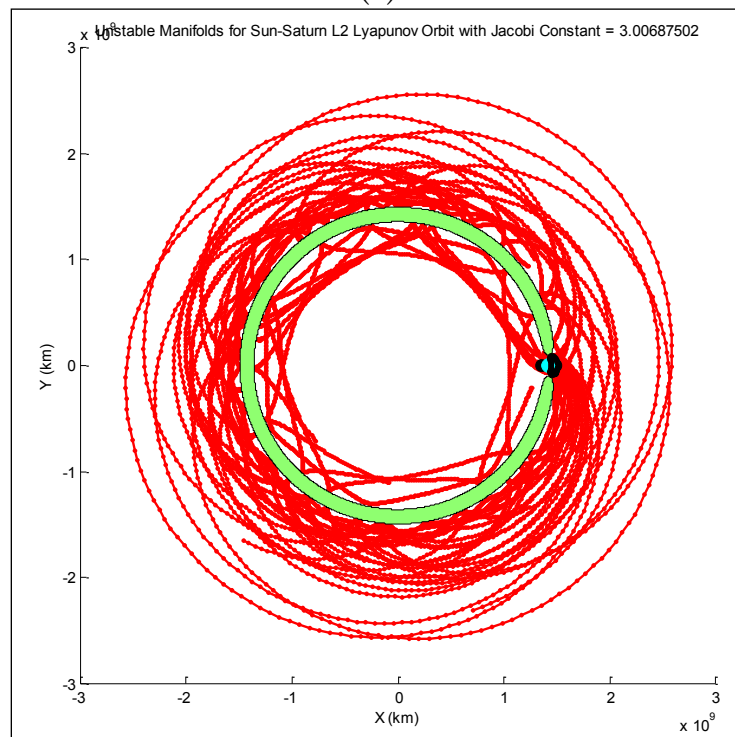
It is seen that as the Jacobi constant of the periodic orbit decreases the unstable manifolds seem to spread farther away from the primaries in a spatial sense (figure (b) vs. figure (a)). But only to a point. By decreasing the constant value more, the zero velocity curves and the forbidden zones disappear and the unstable manifolds seem to collapse inward closer to the primaries. This is likely due to the energy levels of the manifolds and the periodic orbits.

In (a) the unstable manifolds seem to hold their tubular shape and propagate around the outside of the forbidden zone. As was talked about previously, as the Jacobi constant value goes down the energy of the orbit goes up in the two-body system. This allows the forbidden zone to shrink and the manifold trajectories to migrate into broader areas in the two-body system and thus grow outward in space in the CRTBP, as in (b). But after the point where the forbidden zone disappears from the rotating frame, the manifolds likely have enough energy in the two-body system sense that they shrink back into the three-body system.

Therefore, it appears that there is some design trade in the values of the Jacobi constants for the periodic orbits and the ability of the unstable manifolds to intersect with the orbits of the desired third-body targets. This is by no means a thorough quantitative study of this phenomena, but purely a qualitative assessment of the characteristics observed this far. Further insight into this area needs to be taken to better understand where benefits lie.

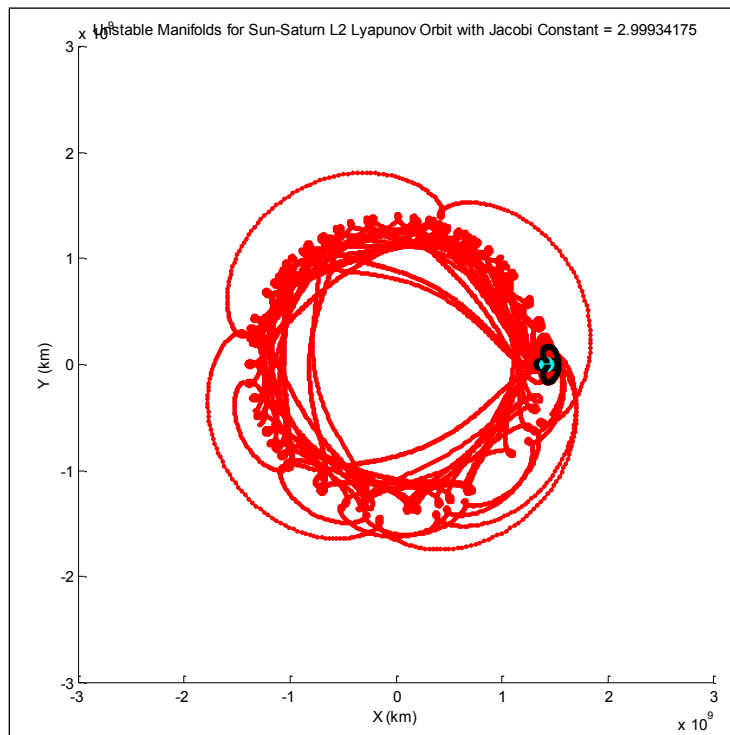


(a)



(b)





(c)

Figure 3-6. Unstable invariant manifold structures from various periodic orbits about the Sun-Saturn  $L_2$ .

### 3.1.4 Intersections of Manifolds with KBO Orbits

The primary goal of a mission may be to rendezvous with and orbit a KBO. Thus far, the majority of work has focused on the means of getting to the target object by the use of manifolds in the CRTBP. The following sections show the first pieces of getting to an object, but are by no means close to fully characterizing the ability of these types of trajectory designs.

#### Simplified Orbit Transfer

This section contains data for a simplified Hohmann type transfer orbit from the Earth to an orbit containing the candidate binary KBO's. This transfer is only in a planar sense and assumes the initial and final orbits are circular about the

Sun. The columns in Table 3-1 indicate the required delta velocity to inject into and out of the transfer orbit from the Earth to the target orbit for each in the binary KBO's. The velocity change is indicated in terms of  $V_{\infty}$ . The last column indicates the half period of the transfer orbit to give some idea of the transit time.

This data is being generated to use as simple benchmark for the amount of velocity change required to arrive at the target object from Earth. These are not detailed estimates but something to use in the early stages of the analysis to indicate whether there is benefit from various options.

Table 3-1. Simple Hohmann transfer velocity increments to transfer from Earth to various binary KBO orbits.

TNOs full_name	spkid	Semi-Major Axis (AU)	deltaV 1	deltaV 2	Total deltaV	Half- period of TO
		a	$V_{inf_1}$	$V_{inf_2}$	delV <sub>tot</sub>	(yrs)
		(km/s)			(km/s)	(yrs)
42355 Typhon (2002 CR46)	2042355	37.97635	11.79308	-3.73836	15.53143	43.05
139775 (2001 QG298)	2139775	39.24782	11.81037	-3.69445	15.50482	45.17
47171 (1999 TC36)	2047171	39.31349	11.81123	-3.69223	15.50346	45.28
134340 Pluto	2134340	39.44507	11.81295	-3.68778	15.50074	45.50
120347 (2004 SB60)	2120347	42.02166	11.84452	-3.60400	15.44852	49.92
80806 (2000 CM105)	2080806	42.17636	11.84630	-3.59916	15.44546	50.19
(2003 UN284)	3169275	42.45076	11.84941	-3.59062	15.44003	50.67
(1999 RT214)	3031906	42.58000	11.85087	-3.58662	15.43749	50.89
(2003 QY90)	3160777	42.80270	11.85335	-3.57976	15.43311	51.28
134860 (2000 OJ67)	2134860	42.90046	11.85443	-3.57676	15.43120	51.46
136108 (2003 EL61)	2136108	43.28627	11.85866	-3.56501	15.42367	52.14
66652 (1999 RZ253)	2066652	43.84450	11.86465	-3.54821	15.41286	53.12
(2003 QW111)	3160800	43.71431	11.86327	-3.55210	15.41537	52.89
88611 (2001 QT297)	2088611	44.08544	11.86719	-3.54103	15.40822	53.55
(2001 QW322)	3092511	44.12765	11.86763	-3.53978	15.40741	53.63
79360 (1997 CS29)	2079360	43.81905	11.86438	-3.54897	15.41335	53.08
(2000 CF105)	3031933	43.81870	11.86438	-3.54898	15.41335	53.08
(1998 WW31)	3031823	44.48152	11.87130	-3.52934	15.40064	54.26
(2005 EO304)	3277443	45.92026	11.88566	-3.48785	15.37351	56.86
58534 (1997 CQ29)	2058534	45.29110	11.87949	-3.50580	15.38529	55.72
(2001 QC298)	3092445	46.28336	11.88914	-3.47762	15.36676	57.52
(2000 CQ114)	3035251	46.16295	11.88799	-3.48100	15.36899	57.30
26308 (1998 SM165)	2026308	47.55763	11.90096	-3.44244	15.34340	59.86
(2000 QL251)	3078880	47.72553	11.90247	-3.43789	15.34036	60.17
48639 (1995 TL8)	2048639	52.25557	11.93960	-3.32179	15.26139	68.75
82075 (2000 YW134)	2082075	57.68104	11.97650	-3.19770	15.17419	79.52
60458 (2000 CM114)	2060458	59.69100	11.98848	-3.15528	15.14377	83.64
136199 Eris (2003 UB313)	2136199	67.73155	12.02940	-3.00171	15.03111	100.80
65489 Ceto (2003 FX128)	2065489	102.23430	12.13244	-2.53572	14.66816	185.55

### Invariant Manifold Orbit Transfer

This section presents some preliminary results of how an unstable manifold from a periodic orbit can intersect with the desired target third-body KBO. It is a single example of the numerous instances the manifolds intersect with the KBO and the difference in the inertial velocities at these intersections. It is a benefit to utilize the unstable manifolds because almost no velocity needs to be spent to get

onto these trajectories from the periodic orbits. However, not all intersections realize a favorable amount of velocity change that would be required to be captured by the target object system once it is rendezvoused with.

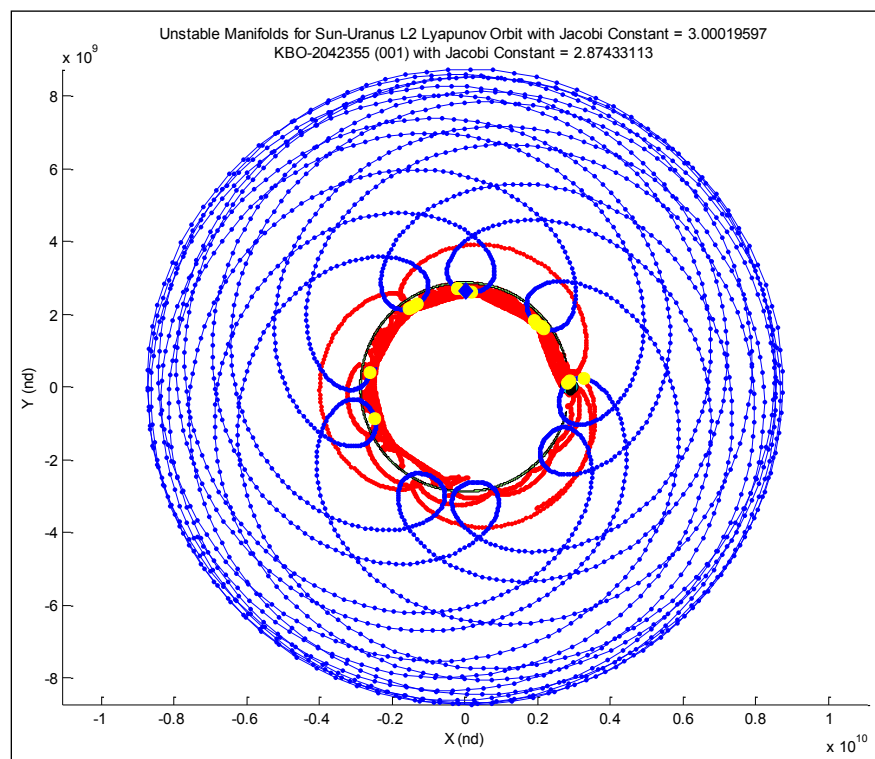
Figure 3-7 shows the intersections between the unstable invariant manifolds of an  $L_2$  periodic orbit in the Sun-Uranus system with the orbit of the binary KBO 2002 CR46. The top figure (a) shows the full view of the rotating frame while the lower (b) figure shows a blowup of the region near the smallest relative velocity difference crossing. For each manifold (red traces) that crosses the KBO trajectory (blue traces), a yellow dot indicates the intersection with the smallest relative velocity difference. The relative velocity difference is the vector difference of the velocities of both the manifold and the third-body trajectory at that given state in the CRTBP, but only in the x-y planar sense. The minimum of the relative velocity difference magnitudes is shown by the blue diamond.

For this example the minimum relative velocity difference is 1.5968 km/sec. As a benchmark comparison, the velocity change for the injection into the target object orbit from the Hohmann transfer calculation shown for the first object in Table 3-1 is 3.738 km/sec, which is twice as large as this transfer. If comparing the total amount of velocity change needed relative to the Hohmann transfer, some nearly 14 km/sec would be available to get from Earth and into the Uranus halo orbit. This is by no means an easy task, but there is room for exploration of ways to get there.

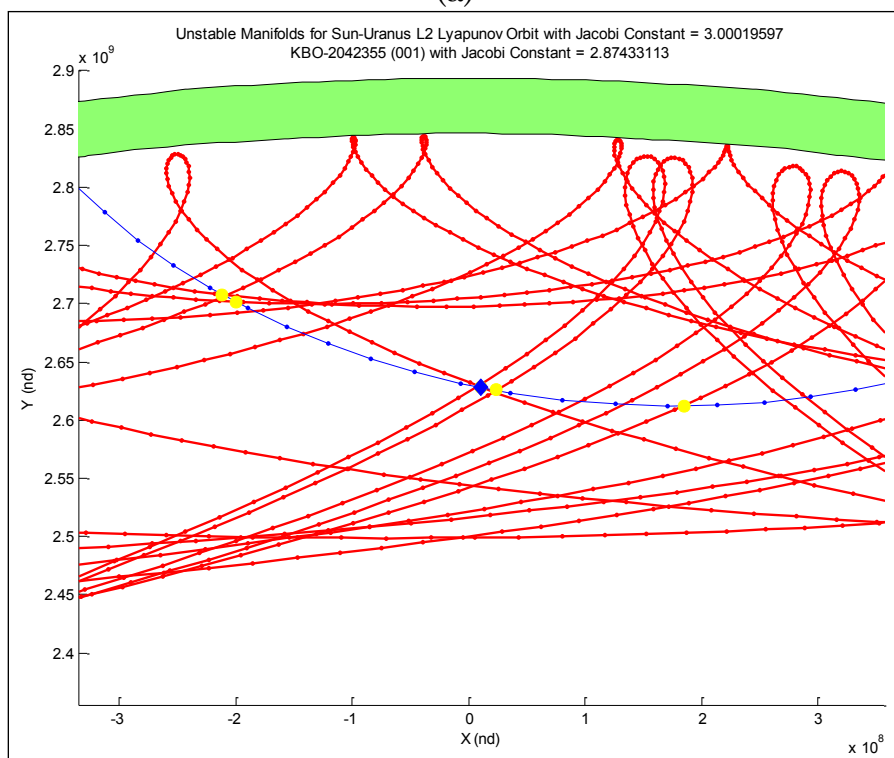
The KBO's trajectory was propagated out for nearly eight periods to get a feel for the amount and size of the intersections that would occur. The manifolds are propagated out far enough for potential intersections, but not necessarily driven by a time period since it is assumed that entry onto the manifold could be designed to correspond with the time of the desired intersection.

Most of the intersections with the lower relative velocity differences occur in the interior region of the manifold's forbidden zone. This is also the region near the point of perigee of the KBO's orbit about the Sun (the flattened parts of the blue trace toward the center of the plot). This example shows how much trade space exists in this problem since at the KBO's perigee it is closer to the central bodies from a special sense, but traveling at its fastest rate in the terms of orbital velocity. Whereas, if an intersection occurred near the KBO's apogee there would be a better chance of the relative velocity difference from the manifold being smaller, albeit farther away from the central bodies. But if the intersection occurred anywhere in the orbit at a place where the inertial velocities matched closely in magnitude and direction, then presumably it would be at a low cost to get captured at that point.

This is an example where a better fundamental understanding of the characteristics of the invariant manifolds and the relationship of the Jacobi constants and orbital energies would help find the most beneficial trades in this large mission space. This method of orbit transfer seems loaded with potential for mission designs, but much more work need to be performed.



(a)



(b)

Figure 3-7. Intersections between the unstable invariant manifolds from an  $L_2$  orbit in the Sun-Uranus system and the binary KBO 2002 CR46.

### 3.1.5 Summary of Method

This section introduced many of the transport tools from Section 2 and their use in examining different three-body systems. The tools were used to help characterize different relationships between three-body objects and the more familiar two-body orbital parameters in an attempt to develop a deeper understanding of the trends throughout different systems. The technique of low energy manifold transport was also developed to rendezvous with outer system KBO's, and characterize potential cost savings for future missions utilizing such low energy techniques.

## 3.2 Manifold Transport to NEO's

Near Earth Objects (NEO's) have become increasingly popular as potential targets for future missions. Previous surveys have concentrated on energy requirements to rendezvous with such objects using orbit matching trajectory maneuvers and two-body transfers. Another technique which produces potentially lower transfer energy requirements utilizes the propagation of the invariant manifolds of libration point orbits in the three-body problem. At the cost of transfer duration these techniques can show potentially improved performance to rendezvous with various NEO asteroid orbits.

NEO's are made up of Near Earth Asteroids (NEA's) and Near Earth Comets (NEC's) with perihelion distances of less than 1.3 AU, as described by the NASA Near Earth Object Program (NASA/JPL, 2010). This analysis looks at the majority of NEO's included in the data base, except those objects that are entirely inside of the Earth's orbit.

This section exercises several of the tools from the previous chapter by looking at the phase-independent orbits in the planar problem to rendezvous with a large catalog of nearly planar NEO's and establishes a baseline for transfer energy requirements in the Sun-Earth three-body system.

### 3.2.1 Periodic Orbits in the CRTBP

The periodic orbits in the CRTBP that are of interest here are orbits that repeat periodically about an axis in the rotating frame. They are not conic and do not exist in the two-body system. But real missions use them for various types of mission designs. Many families of periodic orbits exist in the CRTBP, including families that exist around each of the Lagrange equilibrium points. There are many varieties and categories of periodic orbits in the CRTBP, but this analysis only considers the use of periodic Lyapunov orbits about both of the Sun-Earth  $L_1$  and  $L_2$  Lagrange equilibrium points.

The periodic Lyapunov orbits are a subset of periodic halo orbits that are restricted to the plane of the two primary bodies (the  $x - y$  plane in the synodic frame). Lyapunov orbits are a function of the mass ratio,  $\mu$ , and tend to increase in size with smaller Jacobi constant values. A single-shooting method is used to construct periodic orbits in the CRTBP, as described in Howell's paper (1984) and expanded upon in Section 2.2 above.

These periodic Lyapunov orbits can be generated corresponding to varying values of Jacobi constants about both  $L_1$  and  $L_2$  equilibrium points. These orbits in turn can be used to generate invariant manifolds to transport an object through the three-body system. These are summarized in the following section.



### 3.2.2 Invariant Manifolds of Unstable Periodic Orbits

A manifold may be defined as an  $m$ -dimensional surface embedded in the set of real numbers,  $\mathbb{R}^n$ , which locally possesses the structure of  $\mathbb{R}^m$  (Wiggins, 2003). The term “invariant” indicates that a point on the manifold will remain on the manifold as time evolves. Invariant manifolds can be categorized as stable or unstable, which is to say that the manifolds will approach a saddle point or unstable periodic orbit in the system as time goes to infinity or negative infinity, respectively. Invariant manifolds can be applied to an unstable periodic Lyapunov orbit (one having at least one stable and one unstable eigenvector) about an equilibrium point in the CRTBP.

An object traveling along an unstable periodic orbit that realizes a small perturbation in the direction of the unstable eigenvector will fall away from the periodic orbit in an exponential fashion along the unstable invariant manifold. Conversely, if an object is given the correct initial conditions it will travel in an exponential fashion along the stable invariant manifold and eventually approach an unstable periodic orbit from the direction of the stable eigenvector. The non-dimensional perturbation size of  $1 \times 10^{-6}$  used here is similar to that suggested by Gómez et al. (Gomez, Jorba, Masdemont, & Simo, 1993).

The invariant manifolds of unstable periodic orbits in the CRTBP can be utilized to transport an object from one orbit to another orbit or to possibly intersect another object in a separate orbit. With the vast number of possible Lyapunov orbits and the associated manifolds, and the essentially zero energy cost to get onto these transfers from the Lyapunov orbits, the invariant manifolds can be a very useful tool for designing rendezvous trajectories to small objects near Earth.

Examples of both stable ( $W^s$ ) and unstable ( $W^u$ ) invariant manifolds traveling to and from periodic Lyapunov orbits in the Sun-Earth three-body system

are shown in Figure 3-8 and Figure 3-9 (figures courtesy of (Lathrop & Anderson, 2010)). These figures represent the  $x - y$  planar view of the rotating reference frame centered at the barycenter of the system. The stable manifolds (shown in green) travel from a distance above the Earth (such as a park orbit) to the periodic Lyapunov orbit. The unstable manifolds (shown in red) travel from the Lyapunov orbit to regions outside the Earth's orbit of the Sun. These are sometimes referred to as exterior manifolds because they initially travel outside the region of Earth's orbit. A negative perturbation in the direction of the unstable eigenvector along the periodic orbit can generate similar manifolds that tend to initially go closer toward the Earth. These can be referred to as interior manifolds (not shown on these figures) and are useful for traveling into the interior region of the system.

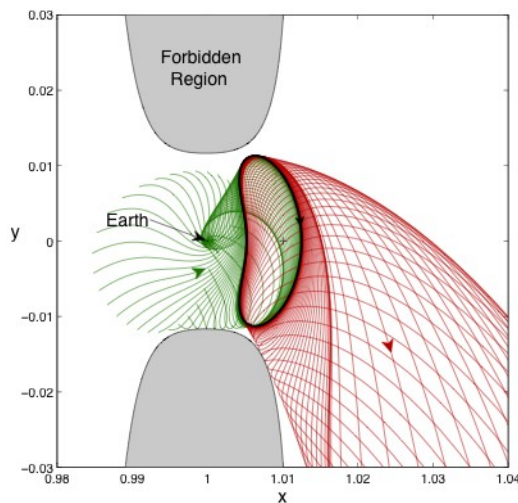


Figure 3-8. Periodic  $L_2$  Lagrange point Lyapunov orbit with Jacobi Constant value equal to 3.00051.

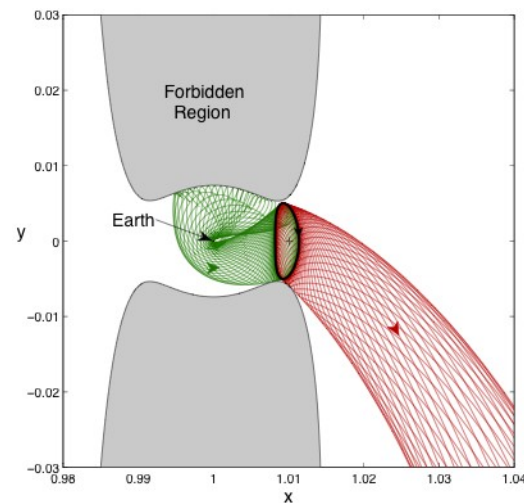


Figure 3-9. Periodic  $L_2$  Lagrange point Lyapunov orbit with Jacobi Constant value equal to 3.00081.

### 3.2.3 Computation for Total $\Delta V$ to Rendezvous

The energy requirements for a spacecraft from the Earth to rendezvous with a potential NEO are reflected in terms of  $\Delta V$ . The maneuvers needed to leave Earth's orbit and arrive at a matching orbit of the targeted asteroid describe the approximate cost in energy. Each maneuver determined in this analysis is assumed to be impulsive. The total  $\Delta V$  expressed in this analysis is calculated starting in a low Earth park orbit (LEO) at approximately 185 km in altitude. This LEO is assumed to be circular and in the ecliptic plane. The first component of the total  $\Delta V$  calculation is the impulsive velocity needed to depart the LEO and propagate asymptotically into the desired periodic Lyapunov orbit. This component,  $\Delta V_{LEO}$ , is independent of the desired NEO being targeted and only a function of the desired Lyapunov orbit being injected into.

The  $\Delta V_{LEO}$  values for this analysis were determined numerically by first generating a periodic Lyapunov orbit in the CRTBP system at the desired Jacobi constant and then propagating a series of stable manifolds from the periodic orbit backward in time until they intersect the LEO. The components of the velocity vector of the circular LEO and the stable manifold at the intersecting point were then compared to determine the relative velocity difference and the  $\Delta V$  required for insertion onto the manifold. The  $\Delta V$ s for each intersection were computed, and the minimum  $\Delta V$  was selected. The relative time of the propagation was also calculated for this LEO to Lyapunov orbit portion of the total transit. Note that this time could vary somewhat depending upon the offset distance used to compute the invariant manifolds.

Table 3-2 Total  $\Delta V$  from a 185 km Circular LEO Park Orbit to various Sun-Earth Lagrange Point Lyapunov Orbits

Lagrange Point	L <sub>1</sub>		L <sub>2</sub>	
Jacobi Constant of Lyapunov Orbit	3.00051	3.00081	3.00051	3.00081
Delta Velocity from LEO to Lyapunov Orbit (km/sec)	3.2279	3.2161	3.2282	3.2162
Delta Time from LEO to Lyapunov Orbit (days)	284.67	238.85	289.90	242.51

To help show a relationship to the energy level of the periodic Lyapunov orbit, a range of Jacobi constants for both L<sub>1</sub> and L<sub>2</sub> Lyapunov orbits were used in this analysis. Table 3-2 shows the  $\Delta V_{LEO}$  values required for two bounding values of Jacobi constant Lyapunov orbits. Refer back to Figure 3-8 and Figure 3-9 to see the Lyapunov orbits associated with the data in the table. These Jacobi constant values were chosen for this analysis to approximately bound the range of energy values of the periodic orbits that allow the stable manifold to intersect the LEO park orbit about the Earth in a reasonable time. Manifolds generated from Lyapunov orbits with Jacobi constants higher than approximately 3.00081 pass by the Earth at too high of an altitude, while those values lower than approximately 3.00051 tend to take a relatively long time before they intersect the desired LEO altitude. Note that the computed  $\Delta V_{LEO}$  values for transfers to the L<sub>1</sub> and L<sub>2</sub> Lyapunov orbits for the same Jacobi constant are very nearly the same, but they can provide pathways to very different regions.

Also included in Table 3-2 are the associated time-of-flights (TOF) needed to travel from the LEO to the particular Lyapunov orbit. This component can then be added to the remaining propagation time along the orbit and the unstable manifold to give an approximate determination of the total mission duration required to rendezvous with the selected NEO.

Since the  $\Delta V$  to insert onto and leave the periodic Lyapunov orbit is generally considered negligible, the spacecraft can travel around the Lyapunov orbit at zero cost until the desired point to asymptotically transition onto the proper unstable manifold to intersect with the targeted NEO orbit. Since any number of unstable manifolds can be generated from the Lyapunov orbit and there is no  $\Delta V$  cost for the spacecraft to transition onto any of manifolds, it is simply a matter of time to propagate around the periodic orbit to get to the desired transition manifold to intersect the NEO orbit. For this analysis the desirable transition manifold from the Lyapunov orbit to the NEO orbit is the one yielding the minimum  $\Delta V$  at the intersection point.

This  $\Delta V$  needed to transition from the unstable manifold to the NEO orbit at the intersection point is the required second component of the total  $\Delta V$ . This component,  $\Delta V_{rend}$ , is referred to as the rendezvous velocity change needed to match the NEO orbit velocity from the manifold velocity at the intersection point. These components are also restricted to the  $x - y$  vector components in the rotating frame.

Similar to the transition from the LEO to the Lyapunov orbit the transition away from the periodic orbit is accomplished by generating a series of unstable manifolds at various points about the Lyapunov orbit and propagating these out until they intersect the NEO orbit. At the point of intersection the relative velocity components were then compared to determine the impulsive  $\Delta V$  needed to transition from the manifold to match the NEO orbit.

Since this analysis is phase-independent, a series of initial states about an entire orbit for each NEO were propagated for multiple orbital periods to account for the time dependency of the third body. The series of unstable manifolds were propagated for a period of time equivalent to just over three years and each intersection between the manifolds and NEO orbit was determined. The period of

just over three years was used as a manageable mission duration time yet still reasonable from a simulation run time upper bound.

The minimum  $\Delta V_{rend}$  for the desired NEO object was determined from all the calculated intersections. Unstable manifolds were generated for Lyapunov orbits at the two Jacobi constant levels and from periodic orbits centered around both  $L_1$  and  $L_2$  Lagrange points in the Sun-Earth system. Unstable manifolds in both the interior and exterior directions were examined. The trajectory times for both the TOF about the Lyapunov orbit and the rendezvous transition along the manifold were also calculated.

The minimum total  $\Delta V$  from the LEO park orbit to the NEO rendezvous was then determined by

$$\Delta V_{tot} = \Delta V_{LEO} + \Delta V_{rend}$$

where the  $\Delta V_{rend}$  is the minimum value from all the intersections for that NEO object and the  $\Delta V_{LEO}$  is the value associated with the same Lyapunov orbit used to get the minimum  $\Delta V_{rend}$ .

### 3.2.4 Limitations of the Analysis

To gather a statistical database for this analysis certain assumptions and process implementations impose limitations to the applicability of the results. By utilizing the planar CRTBP this analysis is restricted to results in the planar case only. The periodic Lyapunov orbits and manifolds are all computed in the  $x - y$  two dimensional plane defined by the Earth's orbit about the Sun. To help reduce the out-of-plane effects of the target NEOs, the database of objects (Jet Propulsion Laboratory, 2007) was filtered to include only those NEOs with inclinations of less than 5 degrees. Based on these criteria the set of objects analyzed is as follows:

- 115 Atens (ATE) Objects

- 986 Apollos (APO) Objects
- 491 Amors (AMO) Objects

The total  $\Delta V$  determined for each object is calculated assuming the spacecraft starts from a circular LEO park orbit in the ecliptic plane at an altitude of 185 km. The velocity cost needed to reach this LEO is assumed to be obtained from a potential launch vehicle and is not included in this analysis. More favorable or more realistic park orbits could be used to begin the trajectory and would affect the results, but those are not reflected here.

While multiple Lyapunov orbits over a range of Jacobi constant values are used to help characterize where minimum results could be found, to apply the analysis to a phase-independent review simulation time has to be limited to reasonable durations. To accomplish this, certain discrete parameters were used. To be time-independent the target NEO's orbit was varied so that it could intersect the manifolds at the correct time. For computational considerations a series of 20 evenly spaced trajectories for the third body were used to characterize time independence. There are also an infinite number of potential unstable manifolds leaving a periodic Lyapunov orbit that could intersect the NEO orbit. These were limited to 20 evenly spaced manifolds propagated for just over three years of simulated time to reach any intersections.

Therefore, the exact minimum results may not be captured in each case, but with a large database of objects to analyze, the analysis results hope to characterize the trends. It is also worth noting that the current database of asteroids is incomplete, and the simulated asteroids can serve to give an idea of potential requirements for the large numbers of asteroids that have yet to be discovered. Certainly individual object analysis can be performed in the future to more accurately determine minimum results if needed.

### 3.2.5 Results and Analysis

To aid in comparison, the results from this analysis were compiled similarly to the methods used by Stacey and Connors (2009) and Perozzi et al. (Perozzi, Rossi, & Valsecchi, 2001) For an overall statistical analysis of the phase-independent rendezvous minimum  $\Delta V$  needed to deliver a spacecraft from a LEO orbit to a targeted NEO, the following summarizes the results based on the methods described above. Given this process and the assumptions described earlier, rendezvous intersections between the invariant manifolds and each of the NEOs were achieved for all of the objects with semimajor axes closer to that of the Earth's (all of the ATE and APO object sets). Due, however, to either insufficient propagation duration of the unstable manifolds or the lower relative energy of the manifolds not allowing them to reach a great enough distance from the Sun to intersect the NEO orbit, only 276 of the 491 object AMO set were able to produce even a single intersection. The majority of the minimum  $\Delta V$  intersections resulted from trajectories utilizing external manifolds coming off of the lower energy (Jacobi constant = 3.00051)  $L_2$  Lyapunov orbit. This holds true for about 85 percent of the ATE and AMO sets which contain objects spanning the lower and upper end of the semimajor axis range. The objects in the APO set with the mid-range values of semimajor axes were split about evenly between  $L_1$  and  $L_2$  Lyapunov orbit manifold intersections but were still heavily weighted toward those from the lower energy periodic orbit.

The total transit time from the LEO park orbit to the NEO rendezvous was also computed for each object. These times are associated with the minimum  $\Delta V$  trajectory cases for each object. The total transit times are made up of three components. The first is the time from the LEO park orbit to the particular Lagrange point orbit (see Table 3-2 for these values for the given periodic orbits).



The value used from the table corresponds to the particular Lagrange point and orbit that produced the minimum  $\Delta V$  case for each object. Note that these times will also vary based on the offset used to compute the invariant manifolds, and they will be refined in future studies.

The second component is the time spent between entering and then leaving the periodic Lagrange point orbit. Since the stable and unstable manifolds actually approach and leave the periodic orbit in an asymptotic manner, the calculation of this portion of the total time is somewhat approximate, but should be accurate enough for the purposes of this study. The third component of the total transit time calculation is the time propagated along the unstable manifold from the periodic orbit to the rendezvous point with the NEO object. This time was calculated numerically and is associated with the minimum  $\Delta V$  case for each object.

Based on the ground rule described above limiting the propagation time limit for the unstable manifold to just over three years worth of time, the maximum total transit time for all of the objects analyzed was approximately 1911 days (about 5.23 years). The minimum total transit time for all the cases was approximately 384 days (1.05 years). Trajectory durations within these time spans fall in line with past and current missions of these kinds.

A comparison of the minimum total  $\Delta V$  for each NEO relative to specific orbit parameters can be seen in Figure 3-10 through Figure 3-12. For each of these figures the ATE objects are shown in dark blue, the APO objects in red, and the AMO objects in green. Figure 3-10 shows the data versus each object's semimajor axis. This data suggests, as expected, a strong correlation between an object's semimajor axis and the amount of energy needed to reach it from Earth. The objects that have increased  $\Delta V$  requirements above the strong lower line are possibly those objects needing additional velocity to match other orbital characteristics.

The velocity needed to reach the NEOs versus their eccentricity value is shown in Figure 3-11. This data also shows a strong correlation between increasing eccentricity values and increasing velocity requirements. This correlation may arise from the greater difference from Earth's orbit and corresponding increases in  $\Delta V$  required to match these different orbits.

Figure 3-12 shows the same  $\Delta V$  values versus the object's inclination. As stated previously this analysis has been limited to planar results and only includes the two dimensional velocity components for the maneuver required between the manifold and the third body orbit. It is known that out-of-plane maneuvers can require large amounts of velocity, which is the reason this analysis limited the NEO set to those objects with inclinations less than five degrees. This was intended to minimize the effect of the out-of-plane velocity component of the third body. The results do indicate that some suitable asteroids with low  $\Delta V$ s exist with near zero degree inclinations for which these planar results would most closely approximate real-world  $\Delta V$ s. Two of these cases are selected for further analysis in the next section.

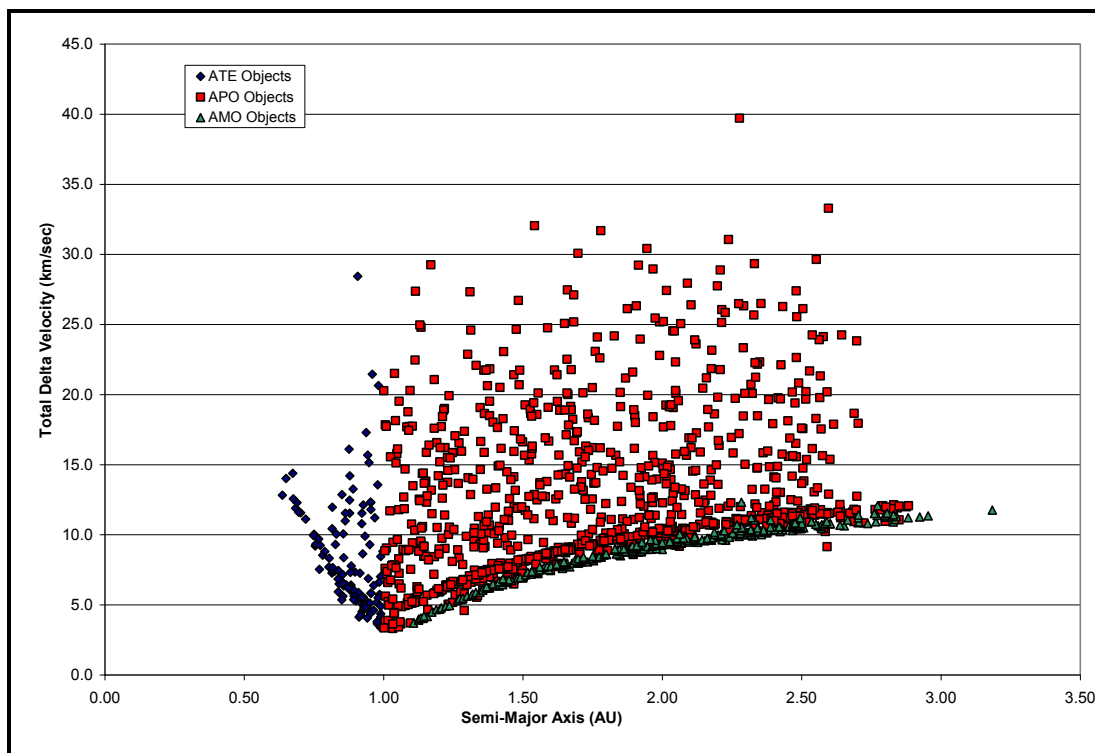


Figure 3-10. Total  $\Delta V$  as function of NEO semimajor axis.

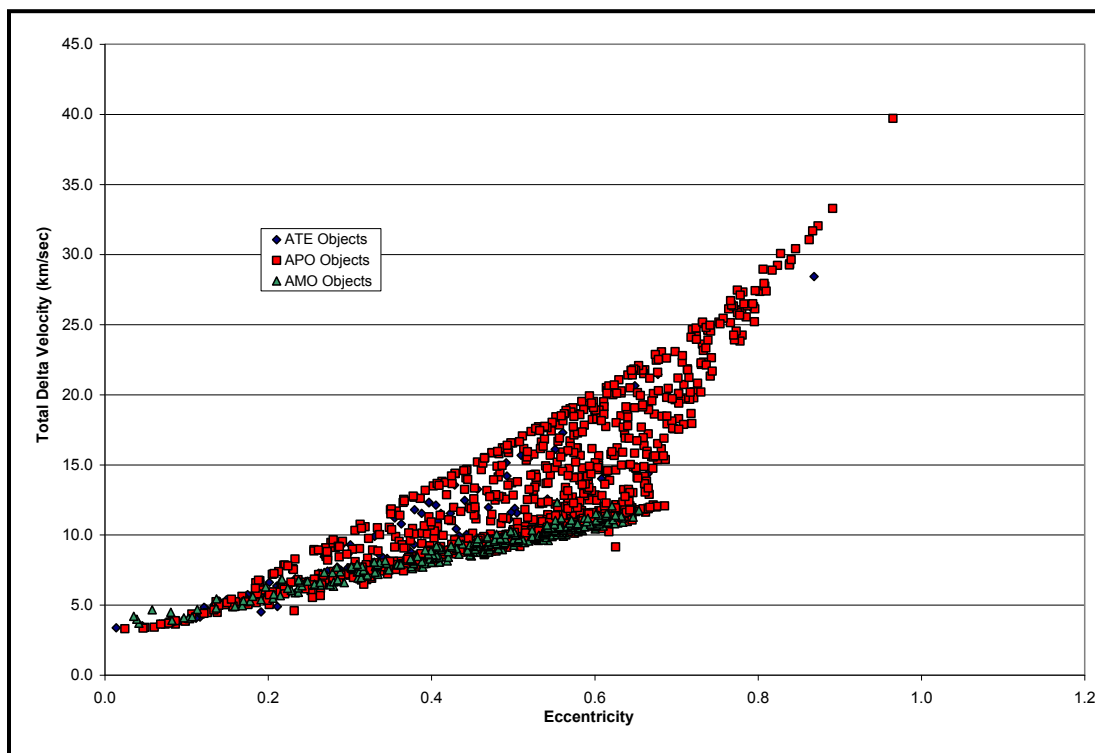


Figure 3-11. Total  $\Delta V$  as function of NEO eccentricity.

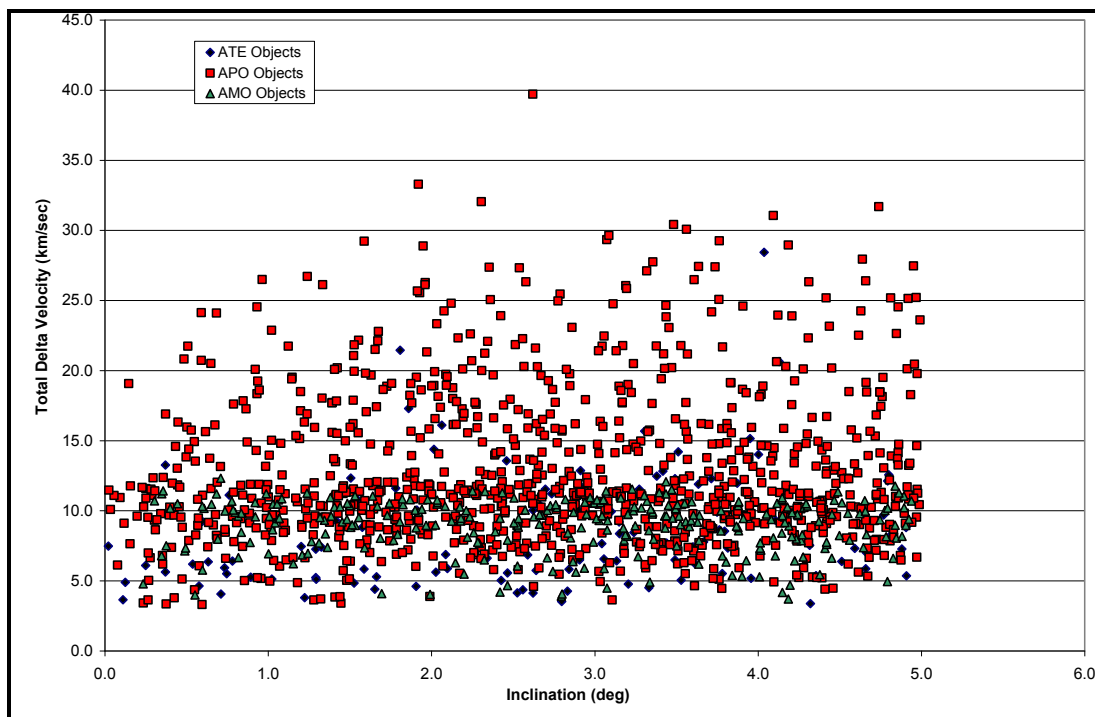


Figure 3-12. Total  $\Delta V$  as function of NEO inclination.

Another approach used to analyze the data was to look at the  $\Delta V$  distribution relative to the Jacobi constant. Figure 3-13 shows the total  $\Delta V$  as a function of the relative difference in the Jacobi constant between the Lyapunov orbit and the NEO object for each of the NEO categories. The top figure shows the ATE objects in blue, the middle curve shows the APO objects in red, and the bottom curve shows the AMO objects that rendezvoused in green. All three data sets show that the closer the NEO's Jacobi constant value is to the Jacobi constant value of the Lyapunov orbit used to transport the spacecraft to the rendezvous, the lower the minimum required  $\Delta V$ .

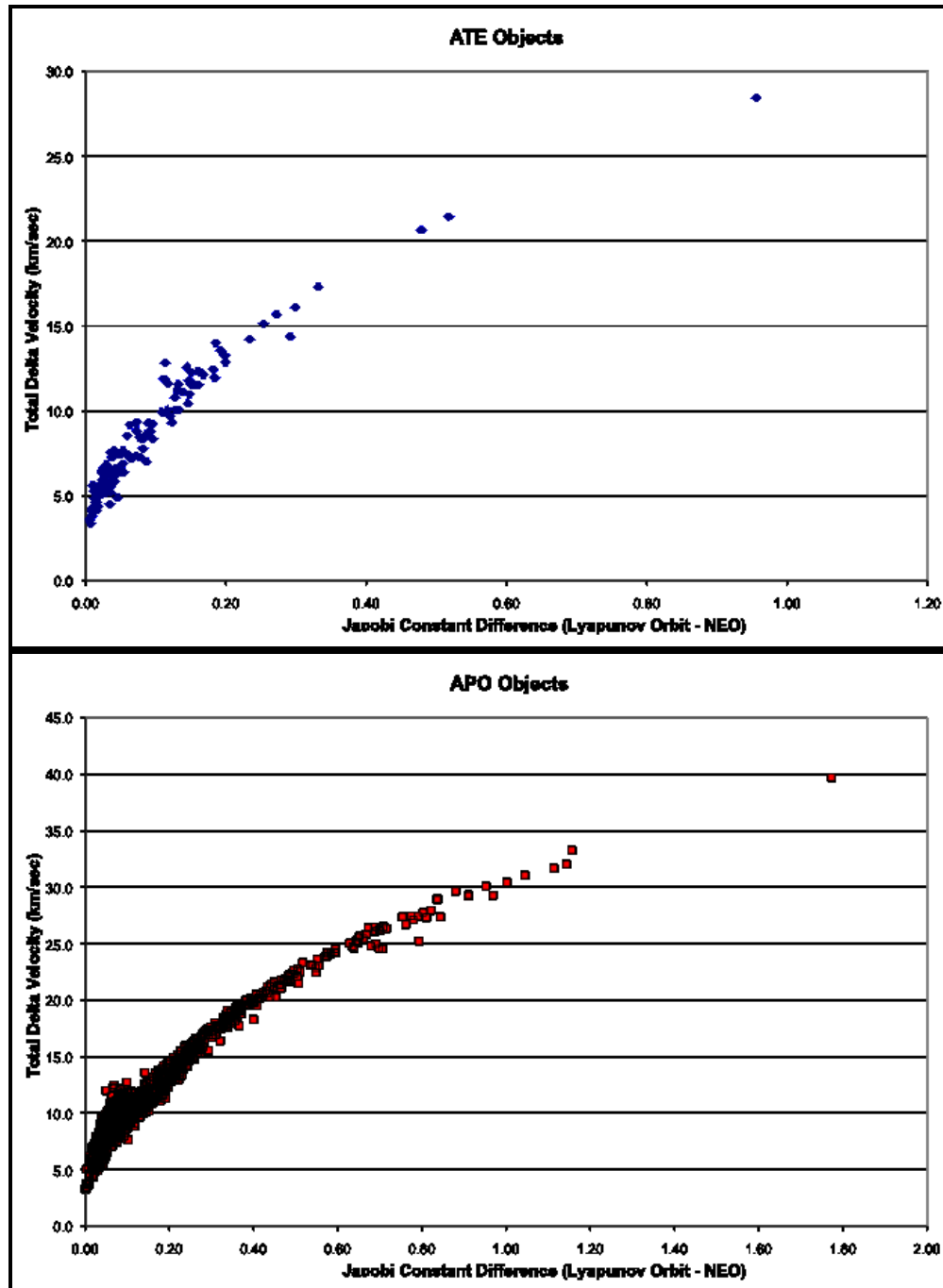
All the values of the Jacobi constant for the ATE and APO data sets used had Jacobi constant values less than the Jacobi constant values for the Lyapunov orbits used in this analysis. The data for the ATE and APO objects both show a growing velocity cost when the Jacobi constant value for the NEO lies farther away

from the Lyapunov value. The data set of AMO objects that produced intersections contained objects both higher and lower in Jacobi constant values than the Lyapunov orbits. That data is shown in the bottom curve on both the positive and negative sides of zero, but the data still shows the trend of lower minimum  $\Delta V$  required for closer relative values of Jacobi constant to the Lyapunov orbit. These results support a rule of thumb in the method for choosing the desired Lyapunov orbit used to transport the spacecraft along the trajectory to minimize the required  $\Delta V$ . A closer match to the NEO's Jacobi constant should yield a lower  $\Delta V$ .

Another parameter used by both Stacey et al. and Christou (2003) is the Earth relative Tisserand parameter, defined as

$$T_E = \frac{1}{a} + 2\sqrt{a(1-e^2)}\cos i$$

This parameter is related to the three-body energy an object would have if it were in the Earth's orbit but can be constructed by the object's Keplerian orbit parameters. Here  $a$  is the object's semimajor axis,  $e$  is the object's eccentricity and  $i$  is the inclination. The  $\Delta V$  values for the objects in this analysis were plotted versus the  $T_E$  parameter, and the results were nearly identical in shape to those in Figure 3-13. These traces also correspond very closely in shape to the results seen in the Tisserand curves shown in the Stacey et al. and Christou papers.



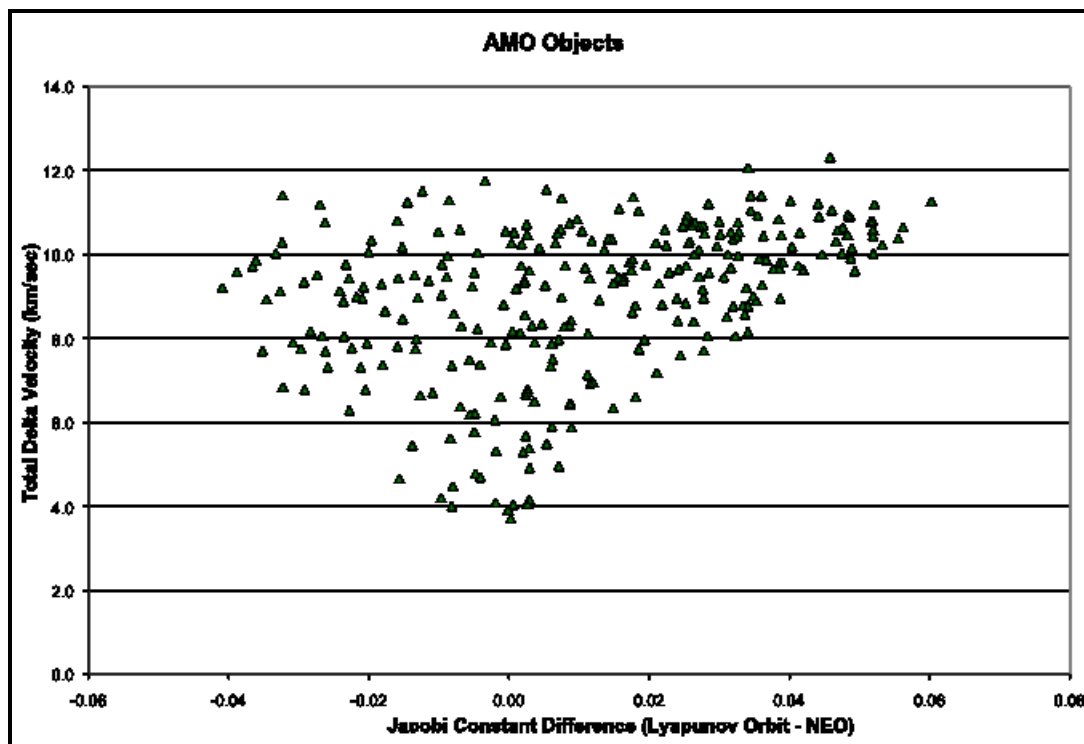


Figure 3-13. Total  $\Delta V$  as a function of the relative change in Jacobi Constant between the Lyapunov periodic orbit and the NEO object.

### 3.2.6 Specific Cases

Several specific comparisons were made to the results from previous research. In some cases the  $\Delta V$ s obtained using the invariant manifolds were larger than the results from this previous research, but many cases showed improvement over the two-body techniques. Specific results from Stacey et al. and Perozzi took into account inclination effects, so it is expected that they would generally have larger  $\Delta V$  values. However, it is worth examining several cases noting as a rough guide that a spacecraft in an Earth-like orbit would require approximately 1.3 km/s to change inclination by 2.5 degrees. One case is asteroid 2003 WP25 in the ATE group which possesses an inclination of 2.5 degrees. Stacey et al. obtained a  $\Delta V$  of 6.3 km/s while a  $\Delta V$  of 4.36 km/s was obtained for this analysis. For asteroid 1991 VG in the APO group with an inclination of 1.45 degrees, Perozzi obtained a  $\Delta V$  of

4.48 km/s while this study produced a  $\Delta V$  of 3.41 km/s. Finally, asteroid 1996 XB27 in the AMO group with an inclination of 2.47 degrees required a  $\Delta V$  of 6.22 km/s in Perozzi's study while this study resulted in 4.66 km/s. As expected these results compare favorably with the spatial results, and they are low enough that future study is warranted to determine if these results will produce superior  $\Delta V$ s even with the spatial effects included. Realistic  $\Delta V$ s for the most planar asteroids, however, can be obtained by examining these cases further. As already seen in Figure 3-12, there are a number of satellite cases with extremely low inclinations and small  $\Delta V$ s.

The following analysis examines two specific cases in detail. These cases were chosen because their inclination values are relatively small, and consequently the planar assumptions of this analysis should yield results for these particular objects that are closer to actual  $\Delta V$  values. Asteroids from different groups were selected for this analysis, with the second producing a very low  $\Delta V$ .

The first object is an ATE asteroid referred to as 2004 FH. It has orbital characteristics of semimajor axis = 0.81 AU, eccentricity = 0.2891, and inclination = 0.021 degrees. The total  $\Delta V$  required to rendezvous for this object is 7.4716 km/sec, which is made up of 3.2282 km/sec to depart the LEO orbit and 4.2434 km/sec to change the orbit of the spacecraft from the manifold to the asteroid final orbit. The total transit time for this trajectory would be approximately 858 days (2.35 yrs). As can be seen in Figure 3-14, the transit includes propagating through a lower energy  $L_2$  Lyapunov orbit onto an unstable manifold that initially starts off traveling toward the interior region near the Earth and between the two Lagrange points,  $L_1$  and  $L_2$ . It then travels out to the exterior region where it intersects the asteroid orbit. The transit from LEO to the Lyapunov orbit is shown in green while the unstable manifold from the Lyapunov orbit to the asteroid is shown in red. Figure 3-14 (a) shows the entire planar system while Figure 3-14 (b) is a blown up section near the Earth and Lyapunov orbit.



The second example is from an APO object referred to as 2007 UN12. It has orbital characteristics of semimajor axis = 1.05 AU, eccentricity = 0.0604, and inclination = 0.235 degrees. The Jacobi constant for 2007 UN12 is equal to 2.99827. The total  $\Delta V$  required to rendezvous with this object is 3.4112 km/sec, which is made up of 3.2282 km/sec to depart the LEO orbit and 0.1830 km/sec to change the orbit of the spacecraft from the manifold to the asteroid final orbit. The total transit time is approximately 1168 days (3.20 yrs). This trajectory, as shown in Figure 3-15, travels from the LEO orbit to a lower energy  $L_2$  Lyapunov orbit and then transitions onto an exterior departing unstable manifold to intersect with the asteroid orbit. This trajectory travels longer to reach a favorable intersection with the asteroid but spends less time near the Earth than the ATE example above. This very low  $\Delta V$  compares favorably with other  $\Delta V$ s found in the literature and is certainly worthy of more detailed analysis.

Figure 3-14 and Figure 3-15 are provided courtesy of (Lathrop & Anderson, 2010).

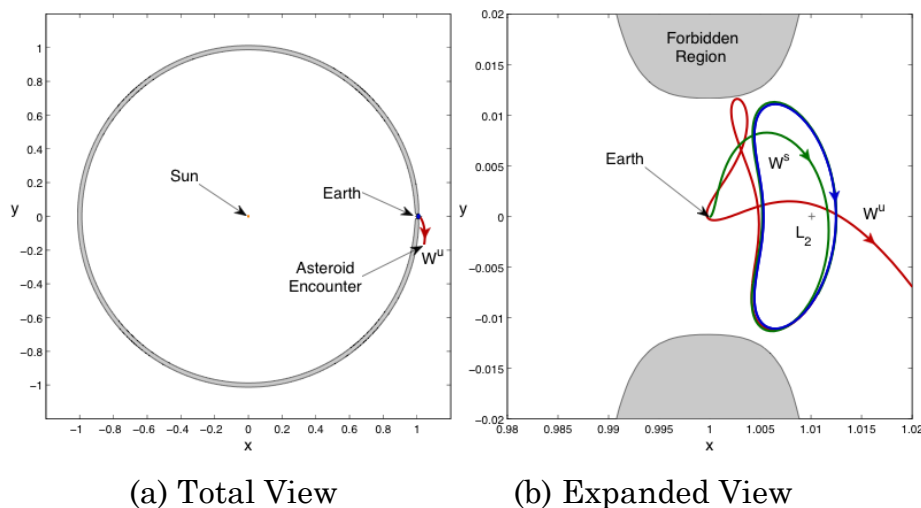


Figure 3-14. Total trajectory from LEO park orbit to rendezvous of example ATE asteroid 2004 FH. This example utilizes an interior region starting unstable manifold from an  $L_2$  Lyapunov orbit with Jacobi constant value equal to 3.00051.

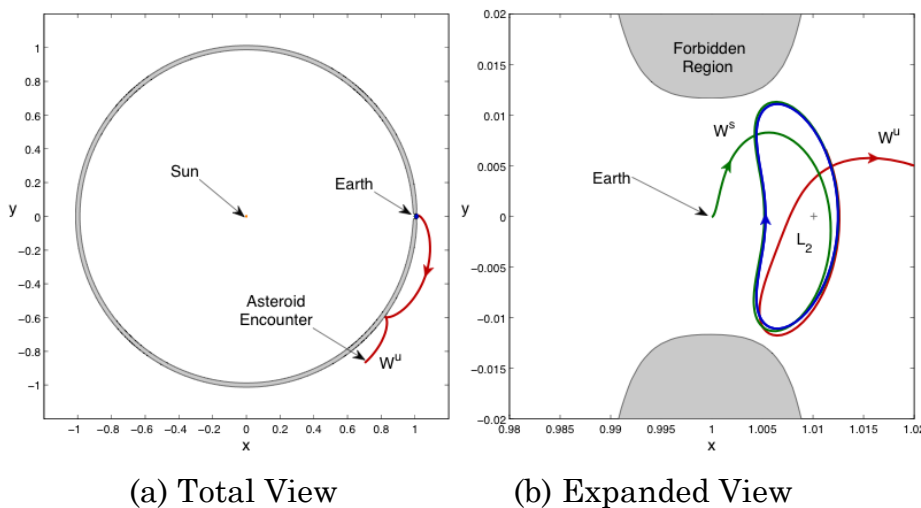


Figure 3-15. Total trajectory from LEO park orbit to rendezvous of example APO asteroid 2007 UN12. This example utilizes an exterior region starting unstable manifold from an  $L_2$  Lyapunov orbit with Jacobi constant value equal to 3.00051.

### 3.2.7 Summary of Method

Many potential asteroid rendezvous trajectories have been computed and analyzed using the invariant manifolds of Lyapunov orbits to transfer from LEO to

the asteroids. Analyzing a survey of the required  $\Delta V$ s revealed several trends. The minimum required  $\Delta V$ s for reaching asteroids tended to occur for those asteroids possessing semimajor axes similar to that of the Earth. Examining the three-body Jacobi constant revealed that the  $\Delta V$ s required to reach various asteroids were a minimum when the Jacobi constant was closest to the Jacobi constant of the selected Lyapunov orbit. As expected, a significant number of the  $\Delta V$ s required to reach asteroids in this planar analysis were lower than those obtained for low inclination orbits in previous studies. Two specific cases were analyzed showing feasible phase-independent rendezvous trajectories that could be computed using invariant manifolds. One of these cases possessed a low total  $\Delta V$  of 3.4112 km/s in addition to a very low inclination of 0.235 degrees. These results compare quite favorably with previously published results, and with this low inclination, the results are potentially close to real world values. The favorable results obtained here indicate that this method is worth pursuing with more detailed analyses.

### 3.3 Periodic to Periodic Orbit Transfer

The advantage of utilizing transfers from one periodic orbit to another is that the velocity cost to leave the initial periodic orbit on an unstable invariant manifold is negligible. The only cost is associated with the arrival and transfer onto the final periodic orbit to match the velocity at the intersection point. This section analyzes the cost and transfer time from periodic orbits about the S-E  $L_1$  and  $L_2$  locations to the S-E  $L_4$  and  $L_5$  locations. The cost does not contain that for getting into the initial  $L_1/L_2$  periodic orbit from the Low Earth Orbit (LEO).

### 3.3.1 Grid Search Method

The technique developed for this analysis utilizes a two- pass grid search method to first run unstable manifolds from the circumference of the initial periodic orbit the intersections of the final periodic orbit. After determining the minimum insertion velocity change from those manifolds, a finer grid of unstable manifolds is then propagated about the initial minimal location, so a local minimum rendezvous is essentially determined.

Figure 3-16 shoes the initial pass of propagations from several S-E  $L_1$  and  $L_2$  orbits to intersections of  $L_4$  and  $L_5$  orbits. Figure 3-17 shows a close up of the unstable manifolds leaving the initial orbits, while Figure 3-18 and Figure 3-19 show the first pass arrival of the intersections at the  $L_4$  and  $L_5$  periodic orbits. All these plots are shown in the Sun-Earth rotating frame.

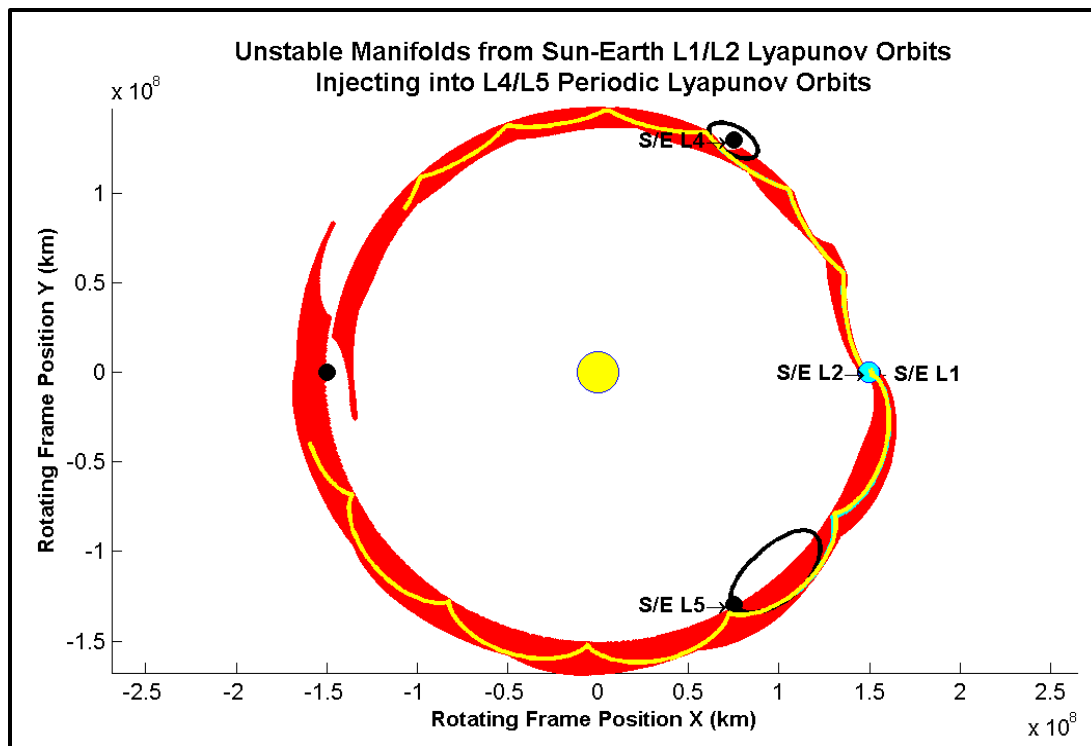


Figure 3-16. Propagation of Unstable Manifolds from S-E  $L_1/L_2$  Lyapunov Orbits to Intersections with  $L_4/L_5$  Lyapunov Orbits.

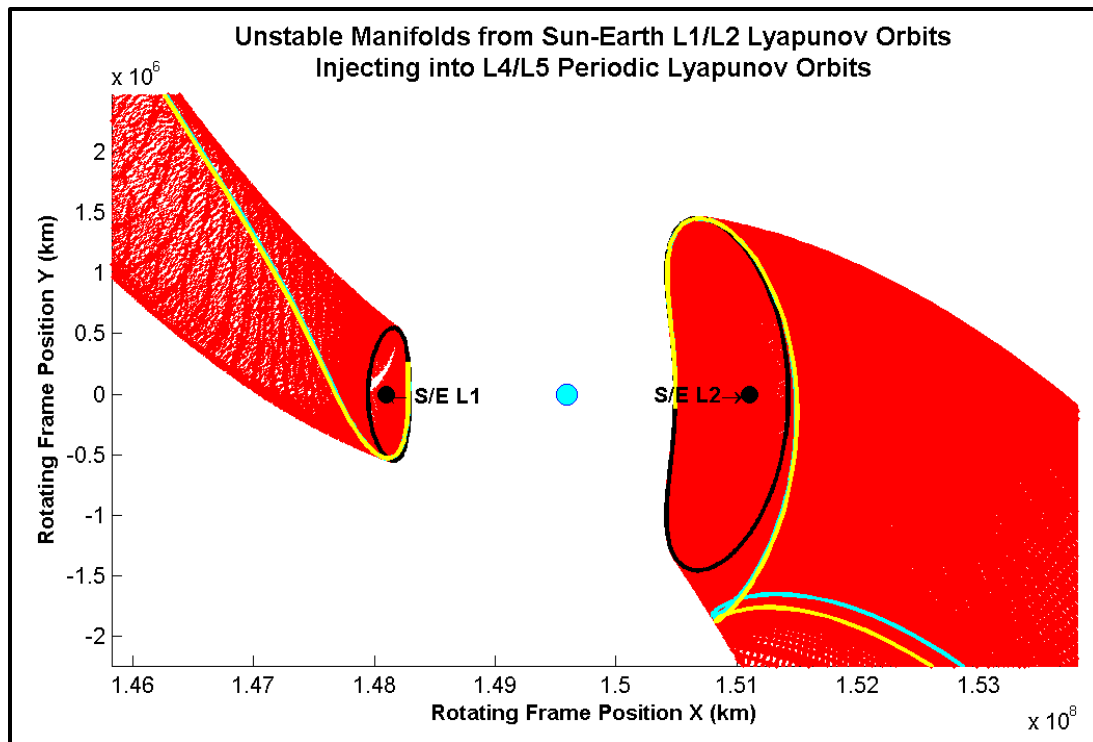


Figure 3-17. Closeup of Propagation of Unstable Manifolds from S-E L<sub>1</sub>/L<sub>2</sub> Lyapunov Orbits.

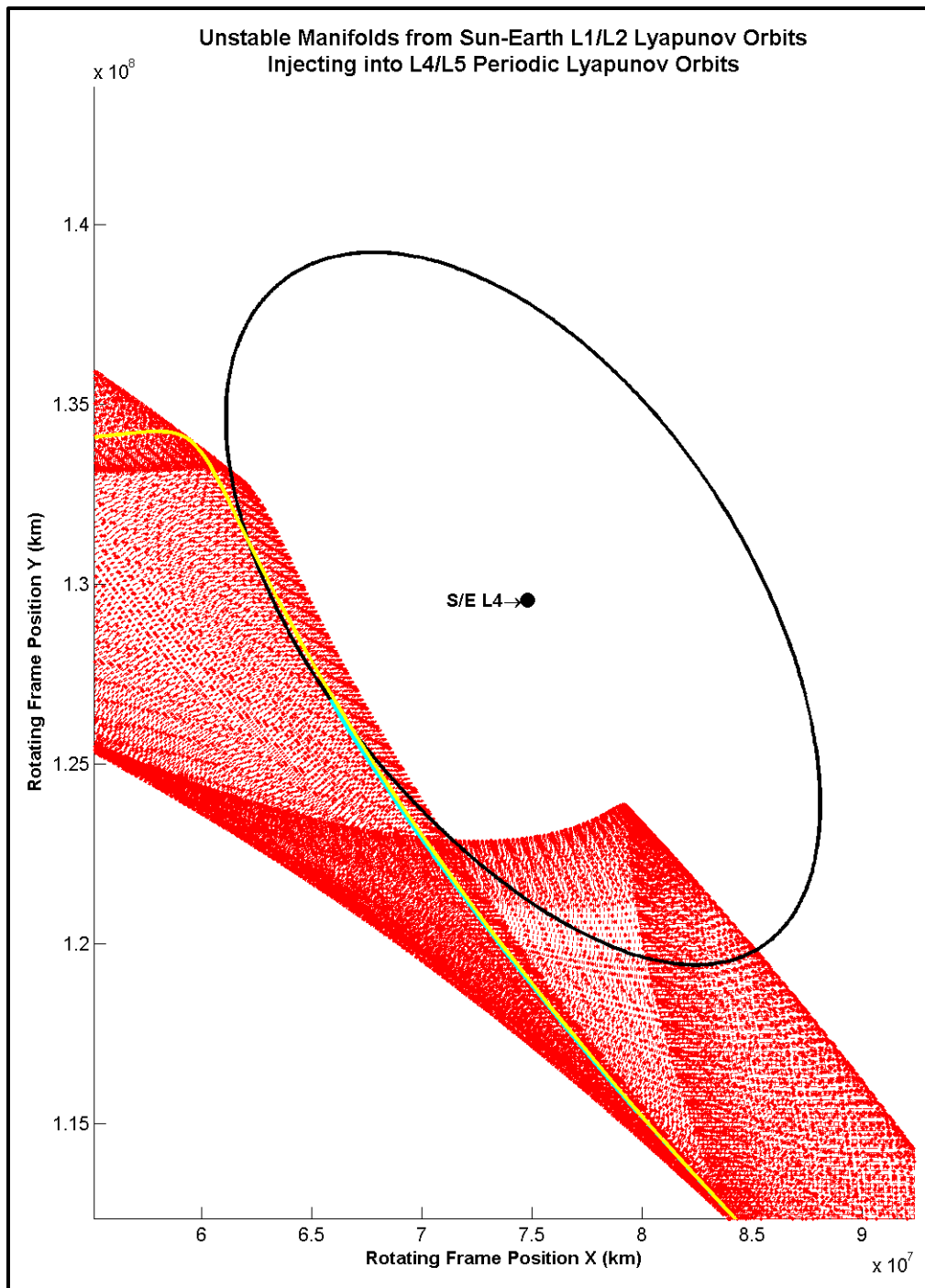


Figure 3-18. Closeup of Propagation of Unstable Manifolds Intersecting S-E  $L_4$  Centered Periodic Lyapunov Orbit.

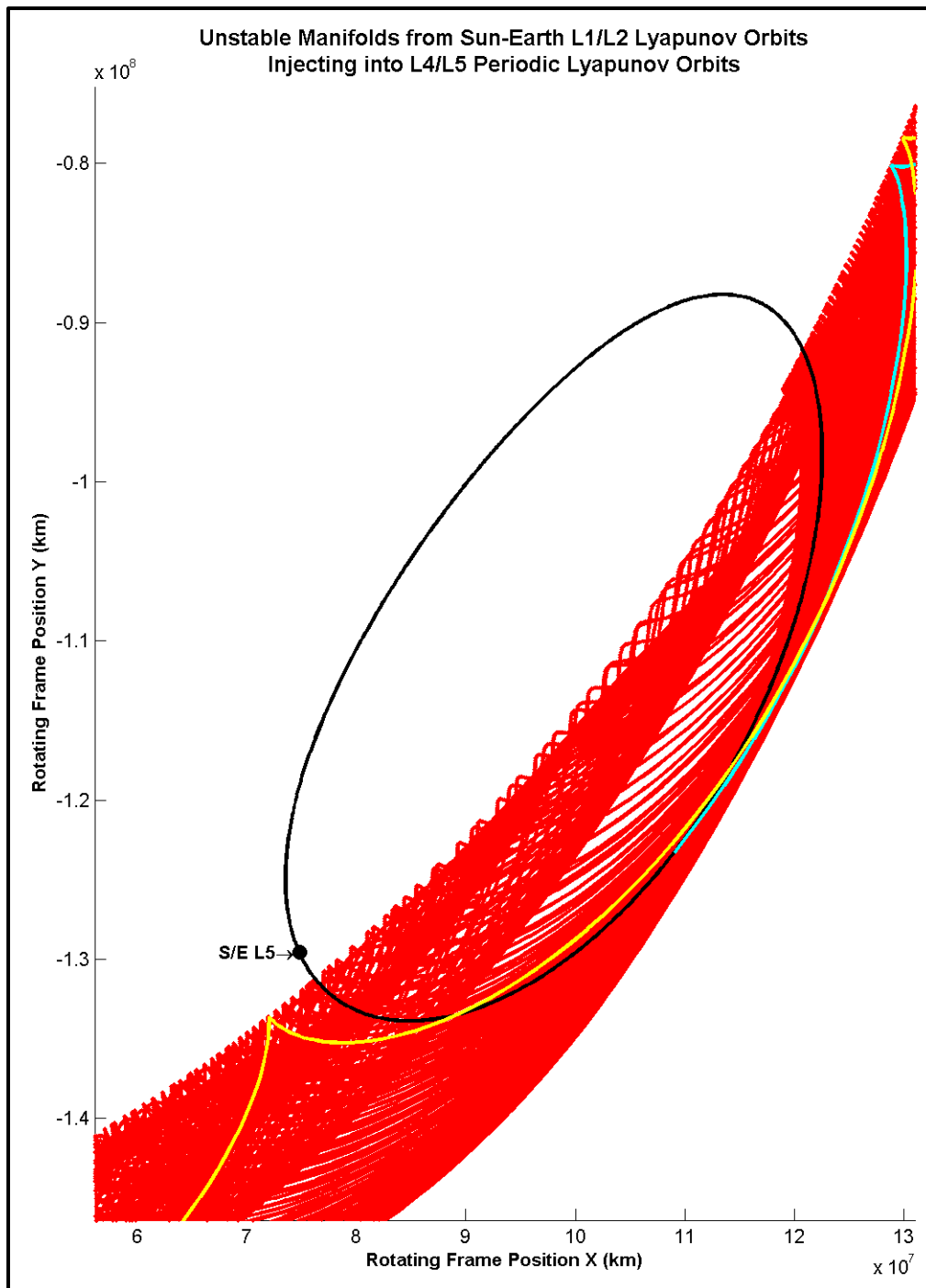


Figure 3-19. Closeup of Propagation of Unstable Manifolds Intersecting S-E  $L_5$  Intersecting Periodic Lyapunov Orbit.

The determination of the minimum rendezvous velocity change to transit from the manifold onto the arriving periodic orbit is found by taking the difference in the velocity of the manifold and periodic orbit at the intersecting state. This is shown on a phase type plot (rotating position magnitude versus rotating velocity magnitude) in an example in Figure 3-20. This indicated the magnitude difference at the intersection point.

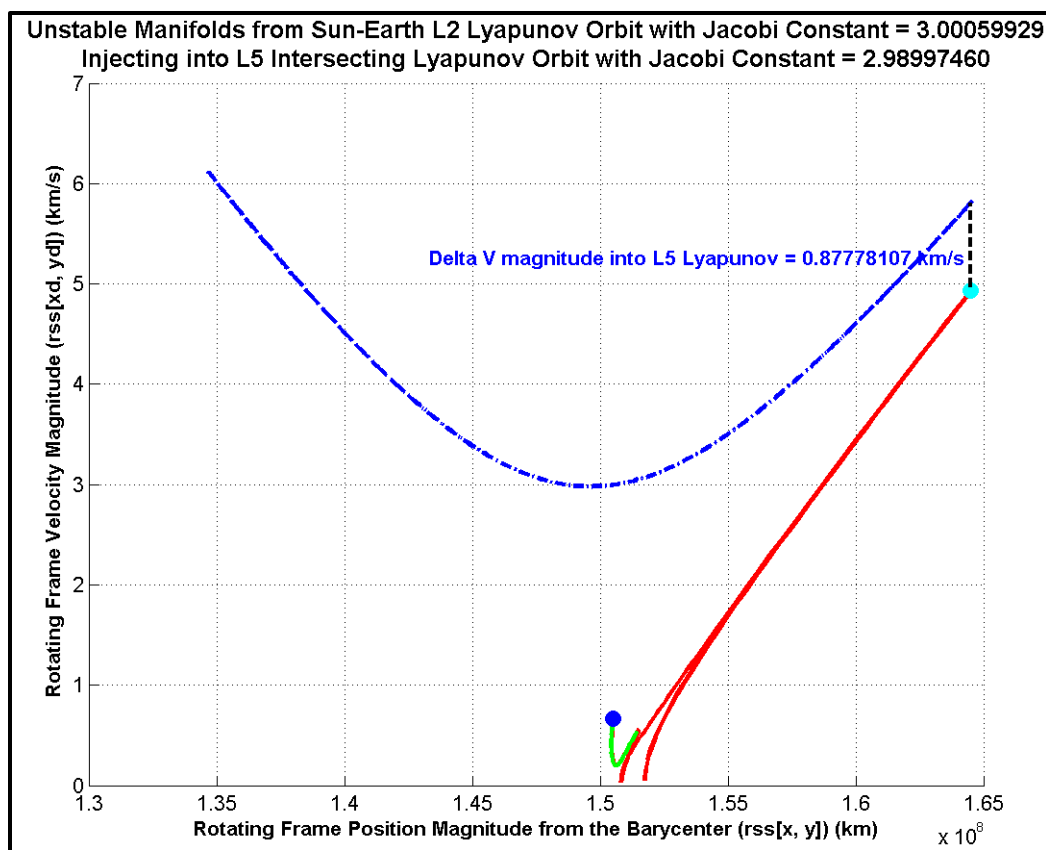


Figure 3-20. Phase Space Traces of Starting and Ending Periodic Lyapunov Orbits and the Connecting Unstable Manifold. The position axis corresponds to the radial magnitude, and the velocity axis corresponds to the total rotational velocity magnitude. The delta V magnitude is applicable at the positional intersection of the manifold and the ending Lyapunov orbit.

But what are really needed to minimize the transfer velocity change is the vector components of the velocity difference. This is indicated in an example in



Figure 3-21, showing the phase plane for both the rotating x-axis (top) and y-axis (bottom) separately. This measure leads to the minimal value for both the vector  $x$  and vector  $y$  velocity components which indicated the smallest required impulsive velocity change. On the figures, the initial periodic orbit is shown as the green oval to the right side, the final periodic orbit as the blue dashed oval on the left side and the manifold transfer as the red line in between.

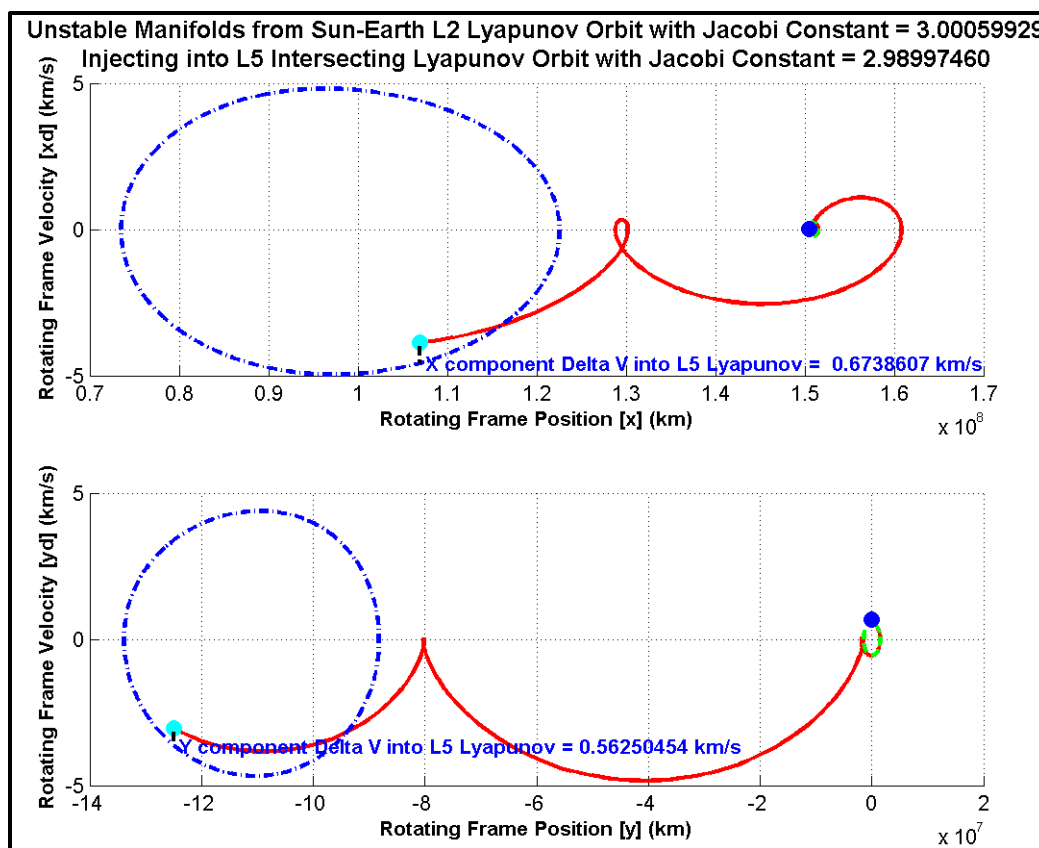


Figure 3-21. Component Phase Space Traces of Starting and Ending Periodic Lyapunov Orbits and the Connecting Unstable Manifold. The position axes correspond to the component  $x$  (top) and  $y$  (bottom) positions, respectively. The velocity axes correspond to the component  $x$  (top) and  $y$  (bottom) velocities, respectively. The component delta  $V$  magnitudes are applicable at the positional intersection of the manifold and the ending Lyapunov orbit.

These localized minimal velocity intersections between the unstable manifold and the arriving periodic orbit were determined for various initial periodic

orbits (from various sizes about  $L_1$  and  $L_2$ ) to various arrival periodic orbit (both concentric and intersecting the  $L_4$  and  $L_5$  points) in the Sun-Earth system. Examples of the complete locally minimal transfers are shown in Figure 3-22 and Figure 3-23. This method will be used across the entire search space and the results shown in Section 4.

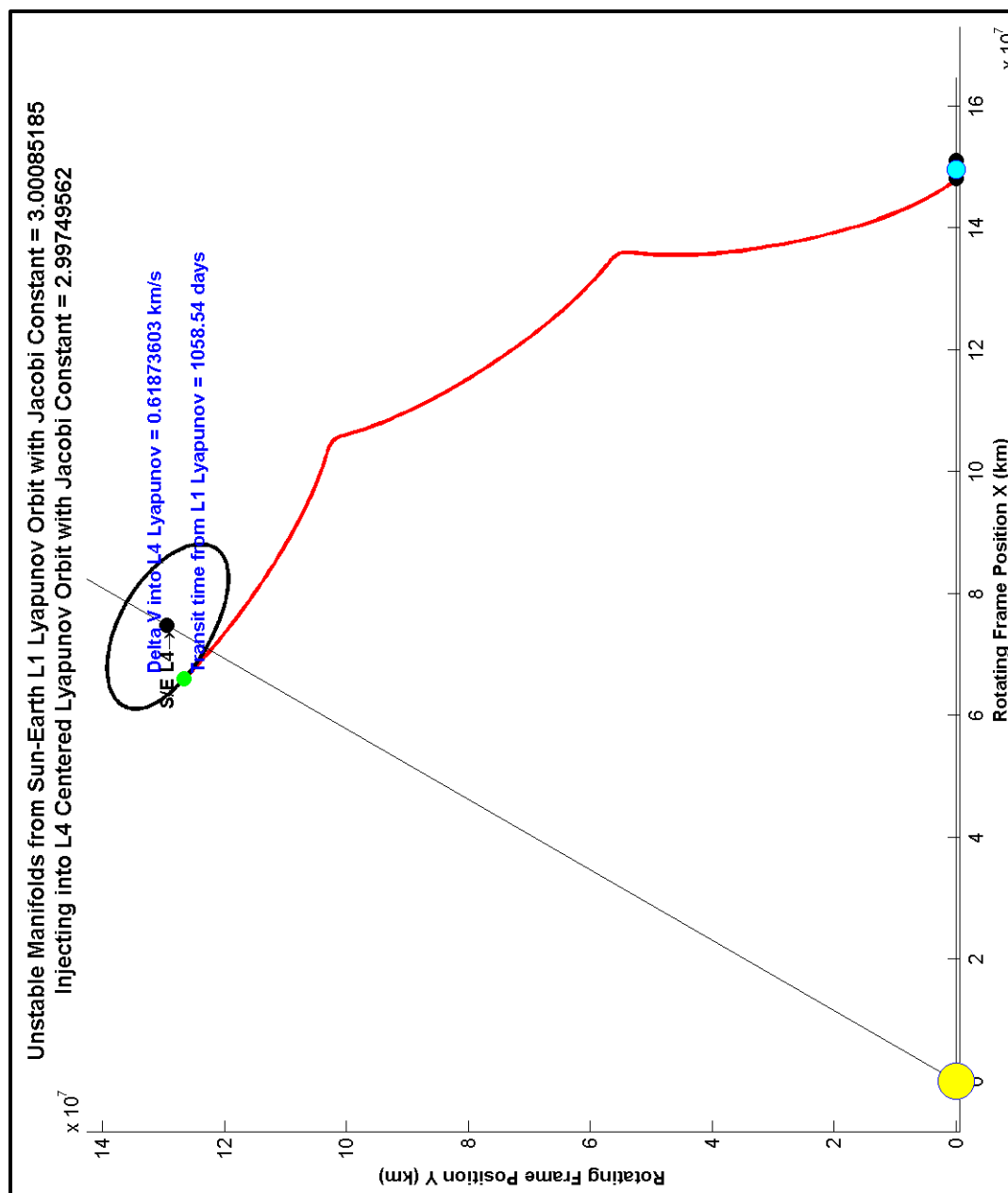


Figure 3-22. Case Solution for Locally Minimum Injection into S-E  $L_4$  Centered Lyapunov Orbit Transferring from an L1 Lyapunov Orbit.

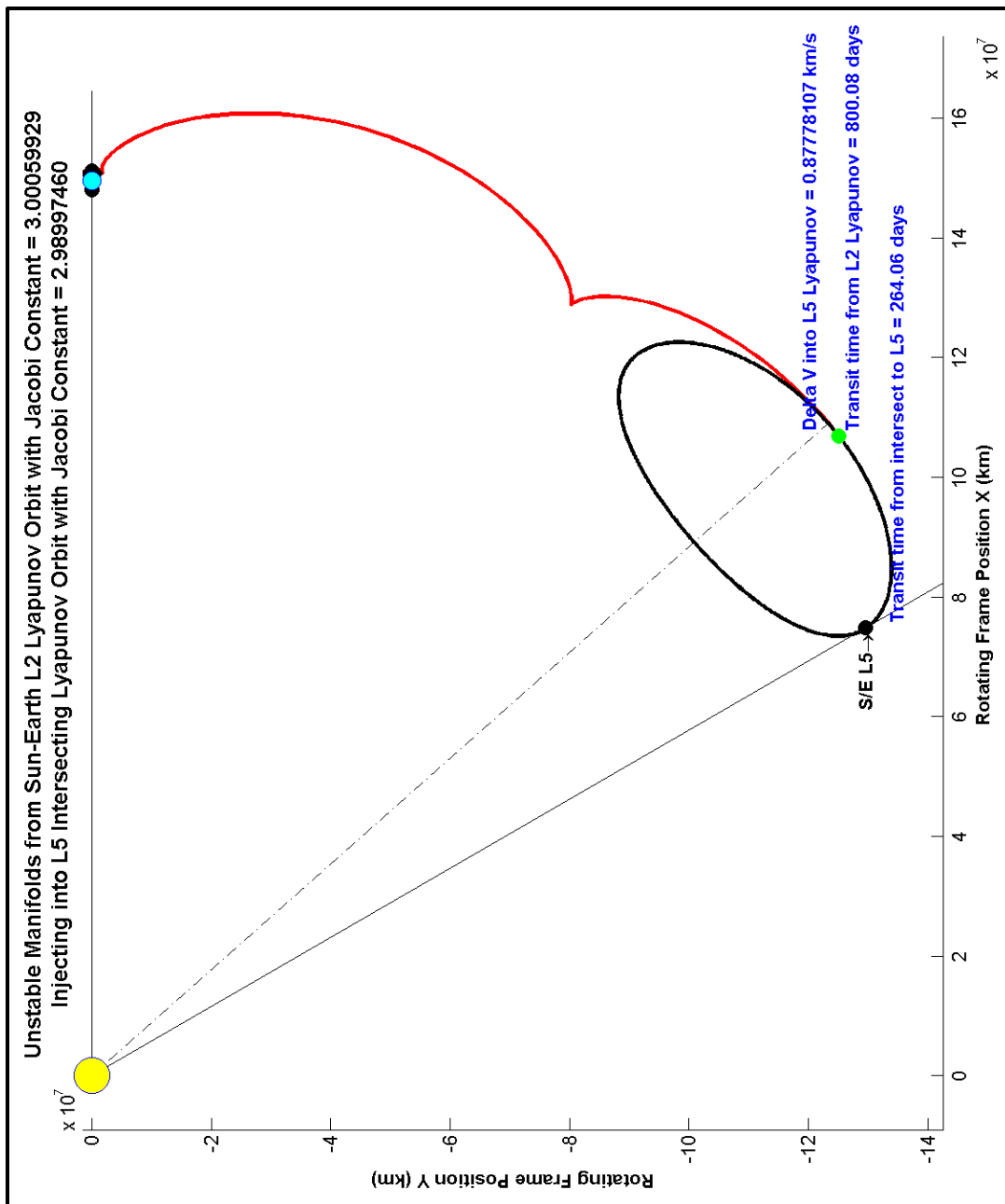


Figure 3-23. Case Solution for Locally Minimum Injection into S-E L<sub>5</sub> Intersecting Lyapunov Orbit Transferring from an L2 Lyapunov Orbit.

## CHAPTER 4

### LOW ENERGY TRANSFERS (APPLICATIONS TO L<sub>4</sub>/L<sub>5</sub>)

The following sections take advantage of the methods and tools described in the previous sections to develop low energy transfers to the Sun-Earth triangular Lagrange points, L<sub>4</sub> and L<sub>5</sub>. Several methods are explored with the goal of determining the delta velocity cost to get from the vicinity of the Earth to points at or near the S-E L<sub>4</sub> and L<sub>5</sub> points.

First is a theoretical determination to get from the Earth to L<sub>4</sub>/L<sub>5</sub> utilizing starting and ending impulsive maneuvers. Next low thrust transfers to the Lagrange points are determined over various impulsive configurations. The utilization of invariant manifolds to transfer from periodic orbits about S-E L<sub>1</sub> and L<sub>2</sub> Lagrange points to various periodic orbits about L<sub>4</sub> and L<sub>5</sub> is explored. And finally a sampling of low thrust transfers over various times that intersect periodic orbits about the L<sub>4</sub> and L<sub>5</sub> points are analyzed.

#### 4.1 Impulsive Ballistic Transfers

From a theoretical perspective, the orbital maneuvering required to go from a position representing the Earth in a circular orbit about the Sun to a position representing one of the triangular Lagrange points in the same orbit (in the rotating frame) can be determined using impulsive starting and stopping velocity changes. While the positions of the Earth and the triangular Lagrange points are coplanar in the rotating frame, they are also in the same size orbit and thus an ideal Hohmann or Bi-elliptic type transfer does not fit for this type of maneuver since there is really no transfer between orbits at the end result.

A more appropriate approach is to utilize circular coplanar phasing, or a circular rendezvous maneuver since the goal is to simply place the object into another angular location in the same orbit. This is sometimes referred to as the coplanar target-interceptor maneuver and is described in Chapter 5 of Vallado (1997). This maneuver utilizes an intermediate or phasing orbit to change the time it takes the interceptor (in this case the object leaving the Earth) to arrive back at the initial angular position at the same time as the desired target arrives (in this case the triangular Lagrange point). This works well with the assumptions of an object in the circular Sun-Earth rotating plane starting at the Earth's position and propagating in a 2-body fashion with the Sun (assumes no Earth gravity).

The concept is then to utilize initial and final tangential impulsive velocity maneuvers at the intersect point to size the intermediate phasing orbit to make up a specified amount of time to intercept the target at a corresponding phase angle change. Two cases arise, the first where the target is leading the interceptor in the orbit and the second where the target is trailing the interceptor in the orbit. The phase angle is defined in the direction from the initial target position to the interceptor initial position, positive in the direction of the targets orbital motion. For the case of the target leading the interceptor the phase angle,  $\theta$ , would have a negative sign as seen in Figure 4-1.

For the leading target case the phasing orbit will be smaller than the circular target orbit in order to make the period of the phasing orbit such that the interceptor arrives back at the intersect point at the same time as the target, which travels less than a full period of the circular target orbit. The initial tangential velocity maneuver will be directed against the orbital motion to shrink the interceptor phasing orbit. The final tangential velocity maneuver will then be equal but in the opposite direction to raise the elliptical phasing orbit back to the circular shape.

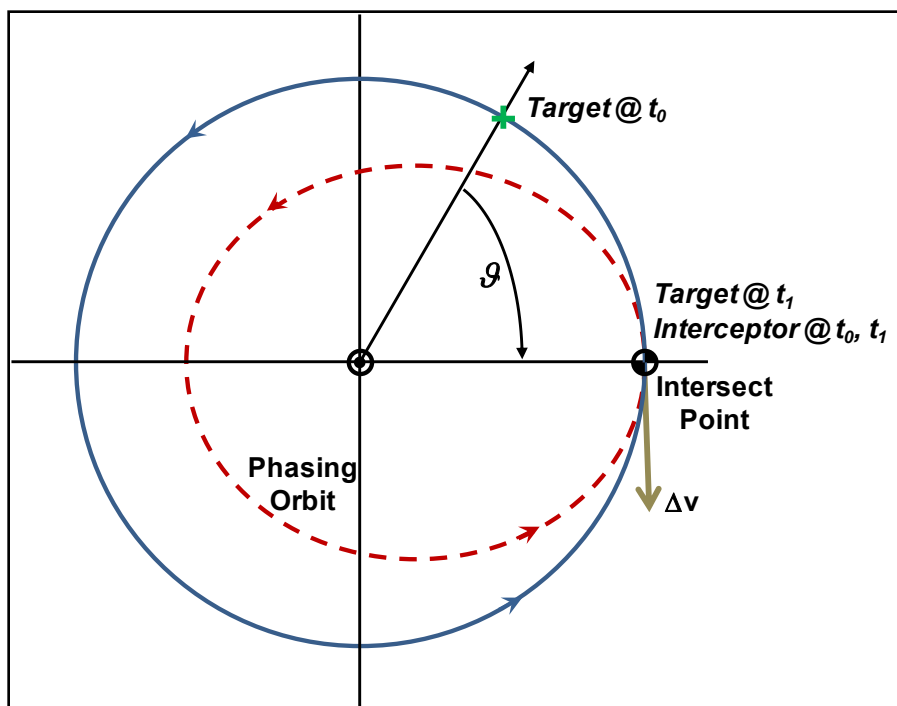


Figure 4-1. Circular Coplanar Rendezvous for a Target leading the Interceptor. The example is for the target representing the L<sub>4</sub> Lagrange point located at a phase angle of -60° from the initial interceptor point at the Earth.

At the initial state in the circular orbit both the target and interceptor angular velocities are equal to the mean motion,  $n$ , of the target orbit:

$$\omega_{tgt} = n = \sqrt{\frac{\mu}{a_{tgt}^3}} \quad (4.1)$$

Here  $\mu$  represents the gravitational constant of the central body (in this case the Sun, and not to be confused in this section for the mass ratio parameter used in the CRTBP described above) and  $a_{tgt}$  indicates the semi-major axis of the target orbit.

For the target to complete  $k_{tgt}$  revolutions, minus the initial separation phase angle,  $g$ , the interceptor completes  $m_{int}$  revolutions about the phasing orbit. Then the time it takes to go around the phasing orbit and return to the intersect point must be:

$$\tau_{phase} = \Delta t = \frac{k_{tgt}(2\pi) + \vartheta}{\omega_{tgt}} \quad (4.2)$$

Because the constraint in this method has the final meeting of the target and interceptor at the intersect point, which is equivalent to the initial interceptor point, the revolutions for both the target and interceptor must be integers, or ( $k_{tgt} = 1, 2, 3, \dots$ ) and ( $m_{int} = 1, 2, 3, \dots$ ). Knowing the mean motion of the phasing orbit is one revolution divided by the period, the semi-major axis of the phasing orbit is

$$a_{phase} = \sqrt[3]{\mu \left( \frac{\tau_{phase}}{m_{int}(2\pi)} \right)^2} \quad (4.3)$$

To find the velocity of the maneuver the circular assumption of the problem and the intersect point allows the change in velocity to simply be the sum of the magnitudes of the impulsive tangential maneuvers into and out of the phasing orbit for the interceptor. From the circular target orbit into the apohelion point of the phasing orbit the velocity change is

$$\Delta v = v_{phase} - v_{int} \quad (4.4)$$

Similarly, from the apohelion point of the elliptical phasing orbit back into the circular target orbit

$$\Delta v = v_{int} - v_{phase} \quad (4.5)$$

Since these two equations yield the same velocity but different signs, the total velocity change is the magnitude of both these maneuvers, or

$$\Delta v_{tot} = 2|v_{phase} - v_{int}| \quad (4.6)$$

$$= 2 \left| \sqrt{\frac{2\mu}{a_{tgt}} - \frac{\mu}{a_{phase}}} - \sqrt{\frac{\mu}{a_{tgt}}} \right|$$

This works for the case when the target is leading the interceptor in the direction of orbital motion. Such is the case in the Sun-Earth rotating frame going from an Earth escape to the L<sub>4</sub> Lagrange point with a phase angle  $\vartheta = -60^\circ$ . A second case exists when the target is trailing the interceptor in the direction of orbital motion, such as in the Sun-Earth rotating frame going from an Earth escape to the L<sub>5</sub> Lagrange point with a phase angle  $\vartheta = +60^\circ$  depicted in Figure 4-2.

In this scenario the interceptor must transfer into a larger period (and thus slower mean motion) elliptic phasing orbit to match the target revolution plus the phase angle, and meet at the intersect point. In this instance the intersecting point corresponds to the perihelion of the phasing orbit. Accounting for the sign difference in the definition of  $\vartheta$  all the above described equations hold for this case as well.

The resultant initial impulsive tangential velocity maneuver will be in the direction of the orbital motion in order to increase the energy of the larger phasing orbit, but the determination of the magnitude of the total velocity maneuver follows the same calculations.



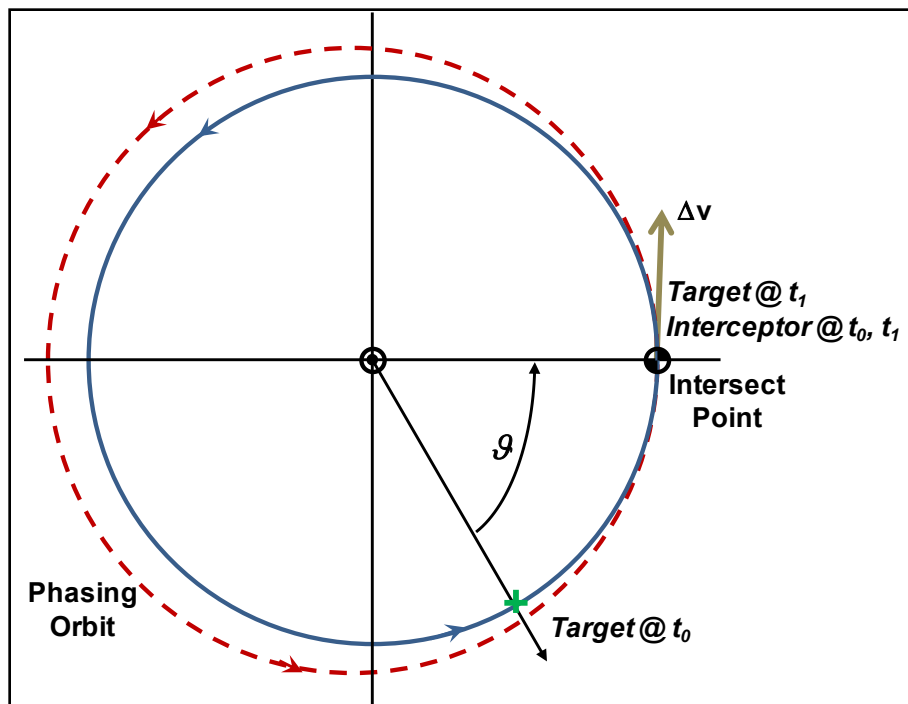


Figure 4-2. Circular Coplanar Rendezvous for a Target trailing the Interceptor. The example is for the target representing the  $L_5$  Lagrange point located at a phase angle of  $+60^\circ$  from the initial interceptor point at the Earth.

For a given phase angle there are any number of solutions to this problem depending on the number of revolutions chosen for both the target and interceptor before reaching the intersection point. The number of revolutions chosen to move around the phasing orbit prior to arriving at the intersection point at the same time as the target leads into the determination of  $a_{phase}$ , and thus the size of the phasing orbit. This phase orbit size leads directly into the magnitude of the velocity maneuver. By varying both  $k_{tgt}$  and  $m_{int}$  the number of revolutions for both the target and interceptor changes the time it takes to get to the intersecting point. The longer it takes to meet, the smaller the period change needs to be to match the synodic period and the smaller the velocity maneuver that should be required.

Applying this method to the Sun-Earth circular coplanar scenario, maneuvering from an initial Earth escape point to target points at both  $L_4$  and  $L_5$ , the phasing orbit semi-major axis size versus transit time can be seen in Figure 4-3.

For the maneuver from Earth to  $L_4$ , with the leading phase angle equal to  $+60^\circ$ , the transit times revolve into the synodic period of a 5:6 resonance and the intersections occur at integer years minus 0.1667 years. Similarly, for the maneuver from Earth to  $L_5$ , with the trailing phase angle equal to  $-60^\circ$  the transit times revolve into the synodic period of a 7:6 resonance and the intersections occur at integer years plus 0.1667 years.

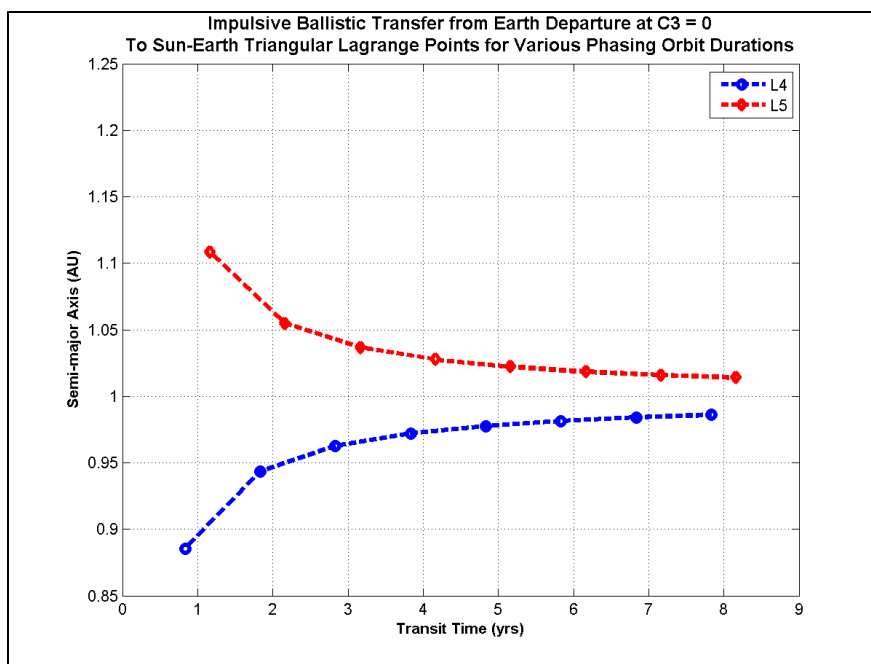


Figure 4-3. Circular Rendezvous Phasing Orbit SMA versus Transit Time. Larger phasing orbits needed to allow  $L_5$  target to catch up, while smaller phasing orbits needed to speed up and catch the  $L_4$  target.

The resultant total velocity maneuvers for each of the transit time cases is shown in Figure 4-4 for both the  $L_4$  and  $L_5$  target intercepts. Trending as expected, the required total impulsive velocity decreases as the size of the phasing orbit change is decreased with the longer transit time cases. While there is a slight difference between the required velocity maneuvers at the shorter transit times, the difference in velocity required to maneuver to either  $L_4$  or  $L_5$  is approximately the

same as transit times increase. This is primarily due to the impulsive nature of the velocity changes and the tangential application of them at the apses points.

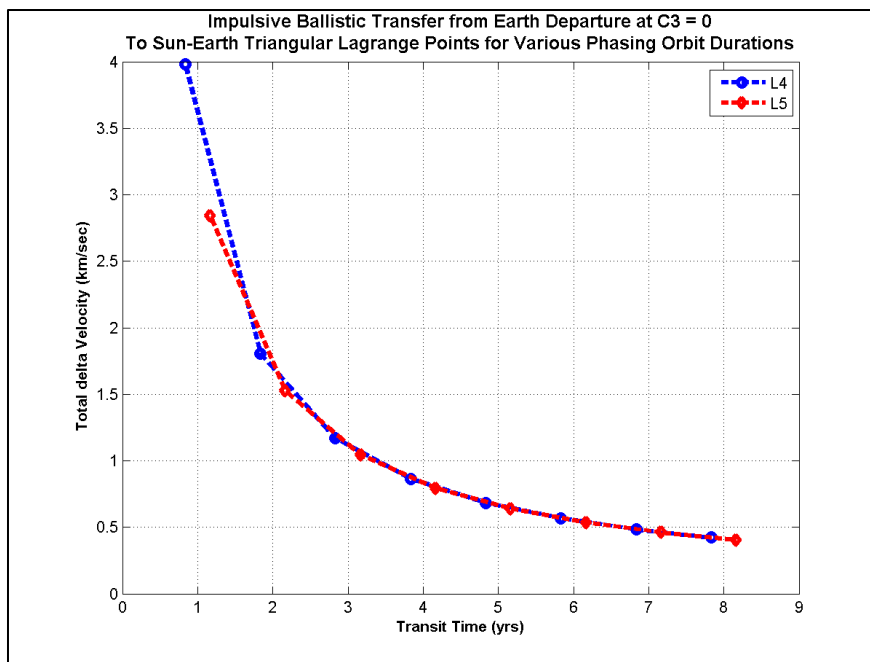


Figure 4-4. Total Velocity Needed versus Varying Transit Times for Circular Rendezvous to S-E L<sub>4</sub>/L<sub>5</sub> Targets. Based from impulsive maneuvers from Earth escape to the leading and trailing Lagrange points.

In summarizing the impulsive ballistic transfers, the minimum impulsive velocity change was determined across various transit times to intersect the target Lagrange point. The magnitudes of the velocity maneuvers range from about 4 km/sec to just under 0.5 km/sec as the transit times spread out to about 8 years. The impulsive nature of these maneuvers make them somewhat ideal, and can be expected to bound on the lower side maneuvers modeled with more realistic finite burns. The orbital changes to the phasing orbit only take into account modifications to the in-plane shape of the orbital elements. The constraining of the apsides to the intersection point does not allow any rotational orbit changes to the phasing orbit such as argument of perigee, which would contribute to higher required velocity maneuvers in more realistic cases.

## 4.2 Low Thrust Transfers

Transfers from the location of the Earth to the location of both of the triangular Lagrange points in the Sun-Earth circular rotating system were determined using the tools and methods described in Section 2.4.1, above. Low thrust trajectories were optimized across a range of transit times to intersect the  $L_4$  and  $L_5$  points with the goal of minimizing the required total velocity change. A range of engine specific impulse, or Isp characteristics was analyzed to determine the effects velocity requirements.

The assumptions built into this analysis utilize the CRTBP modeling of the rotating Sun-Earth system and the location of the triangular  $L_4$  and  $L_5$  Lagrange points. But the dynamic modeling of the tool used assumes the spacecraft initially has achieved an Earth escape trajectory with an Earth relative C3 value equal to zero. This initializes the spacecraft to be in the circular orbit about the Sun starting in the location of the Earth, proceeding in a Sun-centered 2-Body trajectory from that point in inertial space. There are no perturbing forces included from the secondary Earth body included.

Therefore the velocity magnitude results shown in this section are an indication of that needed to transfer from a zero velocity state in the rotating system at the Earth to a zero velocity state in the rotating system at the location of one of the triangular Lagrange points. This does not include any velocity change to launch from Earth and achieve an escape C3 equal to zero for the particular payload.

#### 4.2.1 Direct Transfer to S-E $L_4$

For direct transfer times from one to six years and Isp ranges from 1500 to 4000 sec, low thrust transfer trajectories were optimized to achieve the minimum velocity impact to transfer from the Earth location to the S-E  $L_4$  Lagrange point. A representative trajectory trace in both the rotating and inertial frames is shown in Figure 4-5, and represents a 1.833 year transfer case. The transfer starts at the Earth, represented by the small blue circle, and transfers to the  $L_4$  point indicated with a green plus symbol. The maximum thrust level for this Isp = 1500 sec case is approximately 1.1278 N, and the thrust profile burns for approximately 0.1 years at both the start and end of the transfer as is indicated on the plots by the red arrows.

The initial thrust shrinks the transfer orbit from the initial circular orbit (shown as the dashed circle in the inertial frame) to lessen the orbital period and make up time before intersecting the  $L_4$  point after the 1.833 year transit. The final thrust then raises the transfer orbit back to the size of the circular orbit. In this case the transfer time corresponded to a 5:6 resonance period and the intersection of the  $L_4$  point occurred at the initial starting point of the Earth. The total velocity change to make this transfer is 1.90 km/sec.

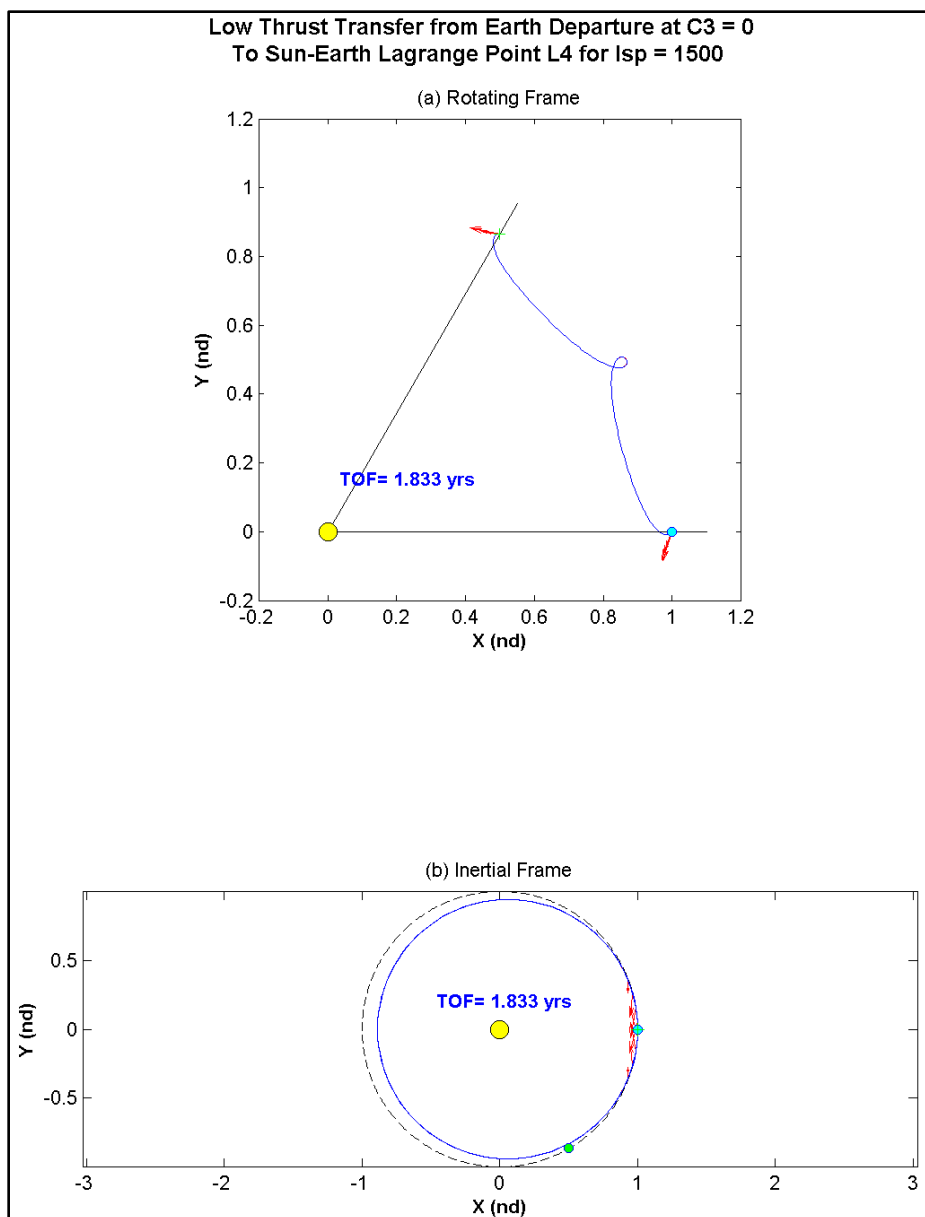


Figure 4-5. Low Thrust Transfer Example to S-E  $L_4$  for  $I_{sp} = 1500$  sec and  $TOF = 1.833$  years. Example case that departs Earth at  $C3 = 0$  and intersects  $L_4$  in the rotating frame after 1.833 years. The trace in the rotating frame is shown in plot (a), and the inertial frame in plot (b).

The same type runs were optimized across various transit times, and the resultant minimum total velocity change to intersect the S-E  $L_4$  point is compiled in Figure 4-6. Once again, this is the delta velocity needed to transfer from an Earth location to the  $L_4$  location in the S-E rotating frame using low thrust and does not

include the velocity needed to launch the payload and achieve an Earth escape  $C3$  equal to zero  $\text{km}^2/\text{sec}^2$ . For comparison the lower bounding impulsive velocity change derived from the circular rendezvous method is shown as the dashed black line.

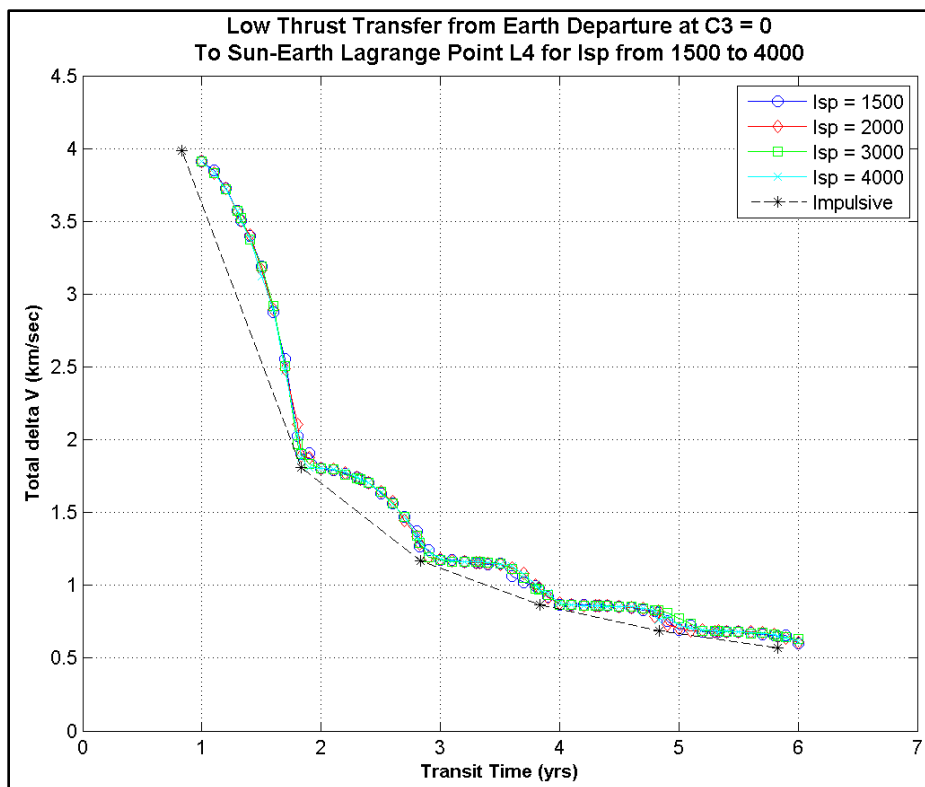


Figure 4-6. Total delta V for Low Thrust Transfers to S-E  $L_4$  versus Transit Time. Multiple cases for engine Isp variances from 1500 to 4000 sec. Velocity change based on an Earth departure at  $C3 = 0$  and intersecting the  $L_4$  point in the rotating frame. Lower bound impulsive velocity change shown in dashed black line.

As is seen on Figure 4-6, the total delta velocity is mostly independent of the range of Isp values of the motor modeled, due mostly to the long durations available for the various thrust levels to affect the needed changes in the transfer orbit. As with the impulsive cases the delta velocity is primarily dedicated to changing the in-plane shape of the transfer orbit in the form of shrinking the semi-

major axis in these cases trying to catch up to the  $L_4$  point. Shrinking the SMA more takes more delta velocity.

Applying the finite delta velocity at the initial and final epochs of the transfer or phasing orbit directly affects the apsides opposed from the intersect point for the cases that have transit times equivalent to the 5:6 resonance periods of the transfer to  $L_4$ . Evidence of this is seen in Figure 4-6 as the delta velocity for the low thrust cases very closely matches that of the theoretical impulsive circular rendezvous results. But there is a slightly different dynamic produced for transit times that fall between the 5:6 resonance requiring slightly more delta velocity for those cases.

Figure 4-7 shows several in-plane orbital elements for the transfer phasing orbit for the low thrust cases plotted against the resultant total delta velocities from Figure 4-6. This gives an indication of what part of the transfer orbit the low thrust velocity is trying to change to most efficiently solve the problem.



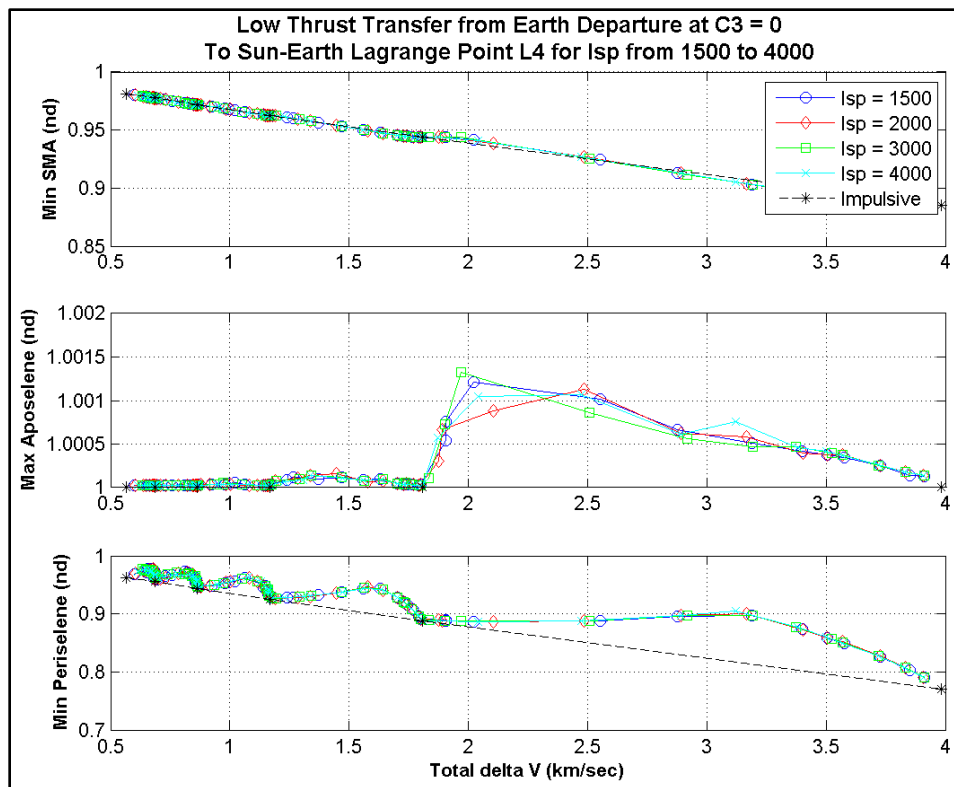


Figure 4-7. Orbital Parameters versus Total delta V for Low Thrust Transfers to S-E L<sub>4</sub>. Multiple cases for engine Isp variances from 1500 to 4000 sec. Velocity change nearly linearly affects the in-plane shape of the transferring orbit via the semi-major axis, but is apportioned differently between the two radii of apsides. Comparison to the impulsive velocity change results shown from the dashed black line.

The top plot in this figure shows a nearly linear relationship between the amount of delta velocity required to affect the semi-major axis and the size of the transfer orbit, which correlates well with the impulsive cases shown. For the impulsive cases that always apply the initial and final burns at the intersect point in the rotating frame, the affect is only seen in the perihelion value of the transfer orbit while the apohelion radius stays the same. This is shown once again by the dashed black trace in the lower two plots in Figure 4-7.

For the shorter transit time cases the optimizer finds it more beneficial to apply the low thrust to actually move the apohelion radius higher, along with lowering the perihelion to achieve the proper period change in the transfer orbit.

After about the second 5:6 resonance period (or after 1.833 year transit times) the longer duration mean motion about the transfer orbit allows the finite low thrust change to properly affect the perihelion radius only and no further impacts to the apohelion radius are needed.

For transit times occurring between the 5:6 resonance periods, the final intersect point is no longer coincident with the initial point at Earth, and therefore a portion of the velocity change must move the transfer orbit apohelion point away from the initial point by affecting the argument of perihelion of the transfer orbit to align with the new intersect point. It needs to move farthest at the transit times corresponding to the midpoint between the resonant periods, and thus requires the most additional delta velocity above that needed to affect the in-plane SMA changes. These effects lead to the characteristic humps between the resonance points seen in the total delta velocity curves in Figure 4-6.

As has been shown for the low thrust transfer cases the total delta velocity needed is essentially independent of the  $I_{sp}$  of the modeled motor. But the thrust for these cases does vary, and how that leads into the delta velocity needed for a given transfer case is based on the motor size and is a function of the proportional payload to motor mass. From the rocket equation,

$$\Delta v = v_e \ln \left( \frac{m_i}{m_f} \right) = g I_{sp} \ln \left( \frac{m_i}{m_f} \right)$$

Here  $\Delta v$  is the velocity change,  $v_e$  is the exit velocity of the propellants and is directly related to the thrust of the motor, and  $g$  is standard gravity. The initial to final mass ratio about the burn is shown by the fraction  $m_i/m_f$ , and indicates the usable propellants during a motor burn. For the cases seen here where a given  $\Delta v$  is fixed for varying values of  $I_{sp}$ , the mass fraction must change proportionally with

the change in Isp. This leads to the required fuel mass to change inversely with the change in Isp.

Lower Isp values then require higher thrust levels and correspondingly more fuel mass to produce the same velocity change. Figure 4-8 shows estimated values for the amount of fuel required to produce the corresponding delta velocity across a range of transit times for varying motor Isp characteristics. A motor with a lower Isp may cost less to produce the same amount of delta velocity, but would require more fuel and be a larger proportion of the total payload mass.

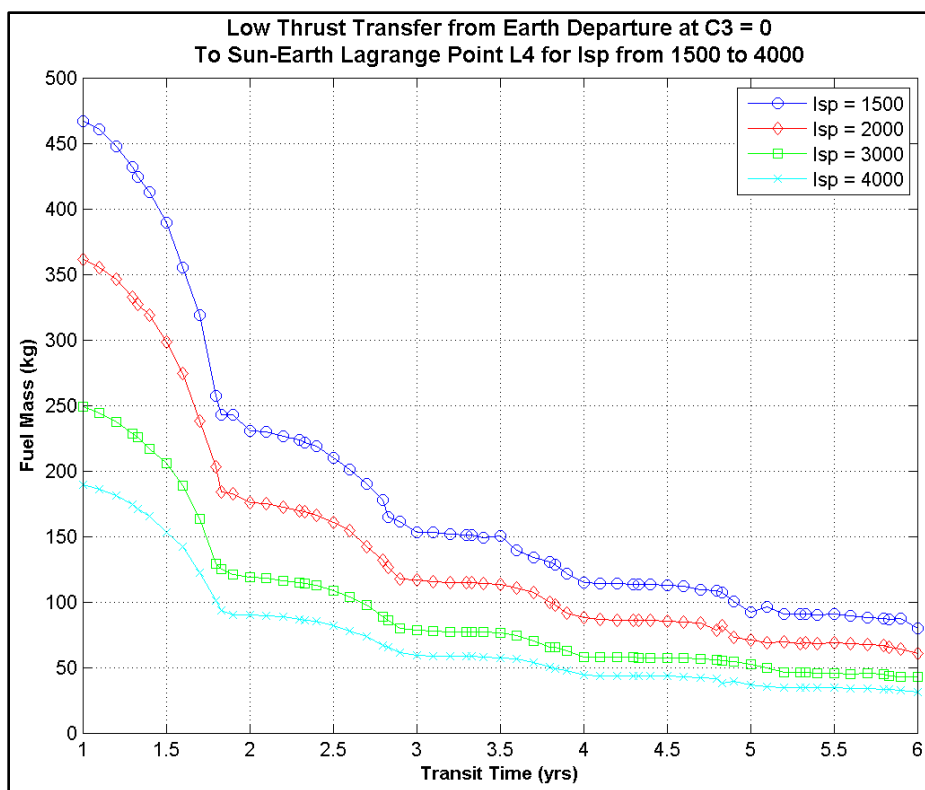


Figure 4-8. Estimated Fuel Mass versus Transit Time required achieving the desired delta V for a Transfer to S-E L<sub>4</sub>. Fuel mass varies with engine Isp to achieve the resultant velocity change and is a greater proportion of total payload mass for higher velocity requirements.

#### 4.2.2 Direct Transfer to S-E $L_5$

In similar fashion to the process described for transfers to the  $L_4$  Lagrange point above, for direct transfer times from one to six years and Isp ranges from 1500 to 4000 sec, low thrust transfer trajectories were optimized to achieve the minimum velocity impact to transfer from the Earth location to the S-E  $L_5$  Lagrange point. A representative trajectory trace in both the rotating and inertial frames is shown in Figure 4-9, and represents a 4.667 year transfer case. The transfer starts at the Earth, represented by the small blue circle, and transfers to the  $L_5$  point indicated with a green plus symbol. The maximum thrust level for this Isp = 4000 sec case is approximately 0.0505 N, and the thrust profile burns for approximately 0.7 years at both the start and end of the transfer as is indicated on the plots by the red arrows.

The initial thrust increases the transfer orbit from the initial circular orbit (shown as the dashed circle in the inertial frame) to increase the orbital period and lose time to let the target catch up before intersecting the  $L_5$  point after the 4.667 year transit. The final thrust then lowers the transfer orbit back to the size of the circular orbit. In this case the transfer time corresponded to half-way between a 7:6 resonance period and the intersection of the  $L_5$  point occurred one-half a revolution from the initial starting point of the Earth. The total velocity change to make this transfer is 0.81 km/sec.

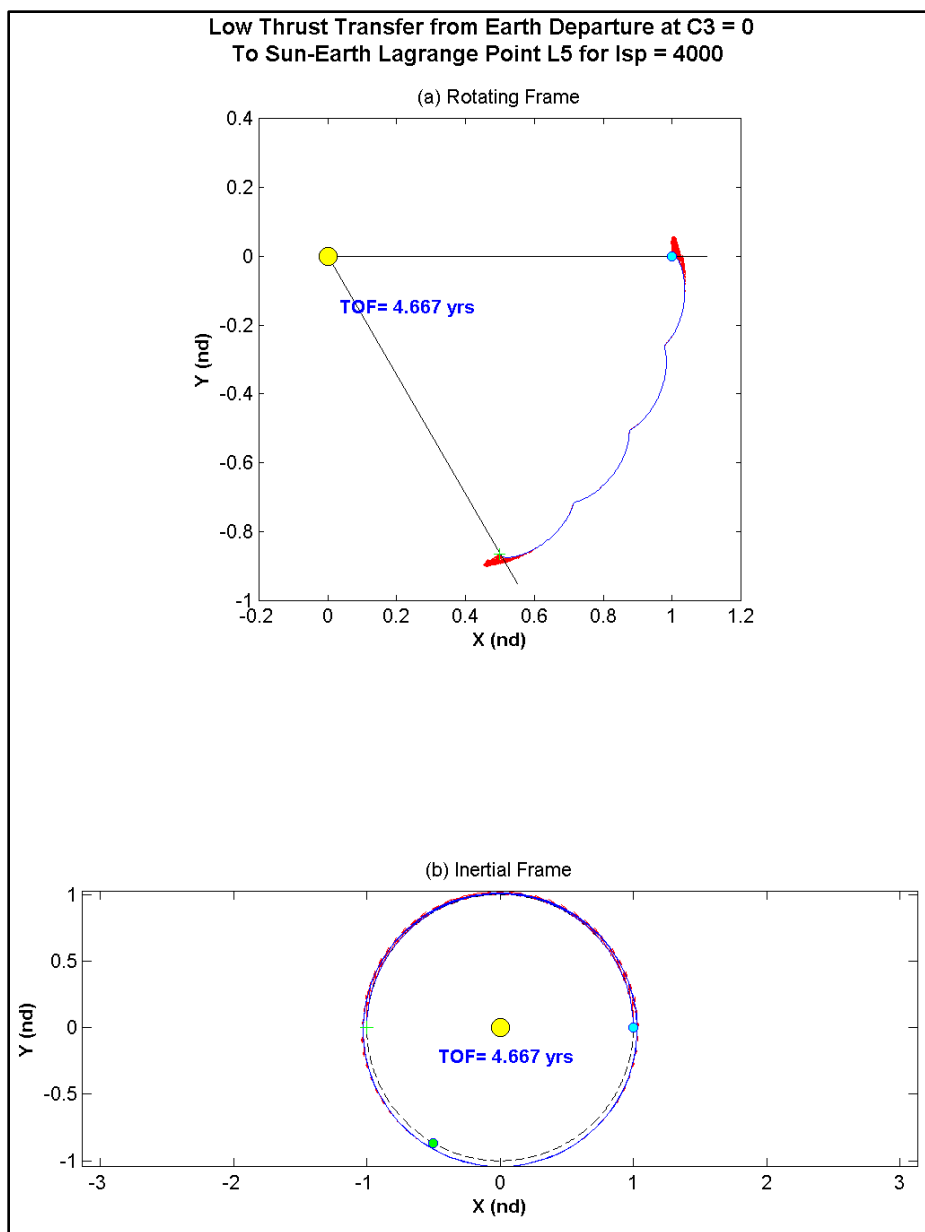


Figure 4-9. Low Thrust Transfer Example to S-E  $L_5$  for  $I_{sp} = 4000$  sec and TOF = 4.667 years. Example case that departs Earth at  $C_3 = 0$  and intersects  $L_5$  in the rotating frame after 4.667 years. The trace in the rotating frame is shown in plot (a), and the inertial frame in plot (b).

The same type runs were optimized across various transit times, and the resultant minimum total velocity change to intersect the S-E  $L_5$  point is compiled in Figure 4-10. Once again, this is the delta velocity needed to transfer from an Earth location to the  $L_5$  location in the S-E rotating frame using low thrust and does not

include the velocity needed to launch the payload and achieve an Earth escape  $C3$  equal to zero  $\text{km}^2/\text{sec}^2$ . For comparison the lower bounding impulsive velocity change derived from the circular rendezvous method is shown as the dashed black line.

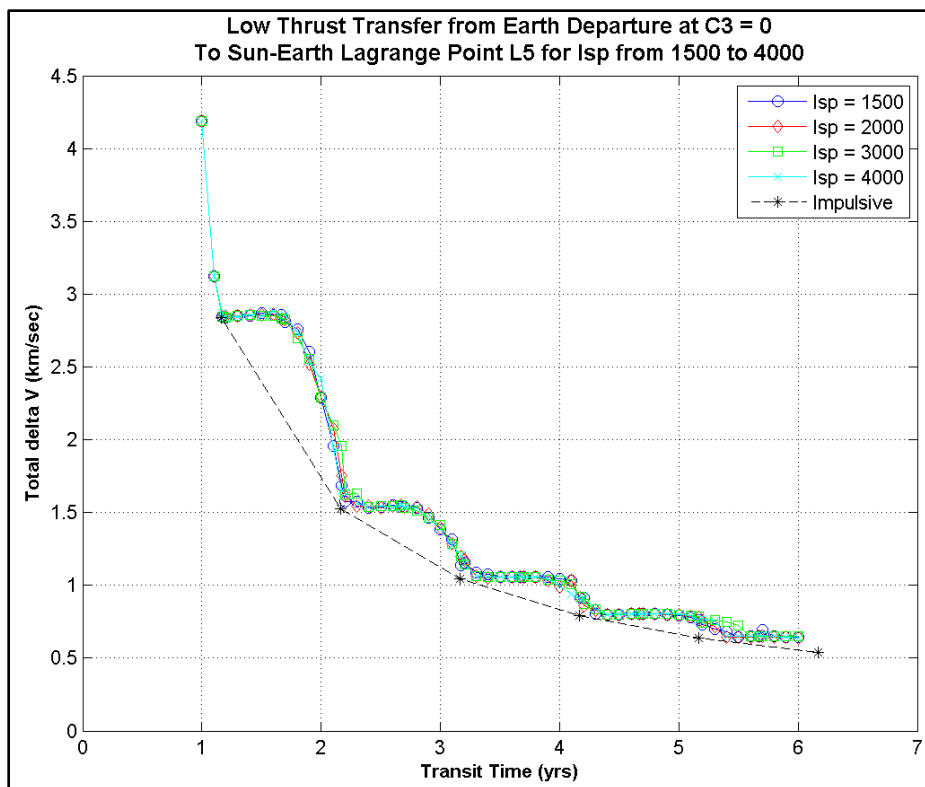


Figure 4-10. Total delta V for Low Thrust Transfers to S-E  $L_5$  versus Transit Time. Multiple cases for engine Isp variances from 1500 to 4000 sec. Velocity change based on an Earth departure at  $C3 = 0$  and intersecting the  $L_5$  point in the rotating frame. Lower bound impulsive velocity change shown in dashed black line.

As is seen on Figure 4-10 the total delta velocity is mostly independent of the range of Isp values of the motor modeled, due mostly to the long durations available for the various thrust levels to affect the needed changes in the transfer orbit. As with the impulsive cases the delta velocity is primarily dedicated to changing the in-plane shape of the transfer orbit in the form of increasing the semi-major axis in these cases trying to slow down and let the  $L_5$  point catch up. Increasing the SMA more takes more delta velocity.

Applying the finite delta velocity at the initial and final epochs of the transfer or phasing orbit directly affects the apsides opposite from the intersect point for the cases that have transit times equivalent to the 7:6 resonance periods of the transfer to  $L_5$ . Evidence of this is seen in Figure 4-10 as the delta velocity for the low thrust cases very closely matches that of the theoretical impulsive circular rendezvous results. But there is a slightly different dynamic produced for transit times that fall between the 7:6 resonance requiring slightly more delta velocity for those cases.

Figure 4-11 shows several in-plane orbital elements for the transfer phasing orbit for the low thrust cases plotted against the resultant total delta velocities from Figure 4-10. This gives an indication of what part of the transfer orbit the low thrust velocity is trying to change to most efficiently solve the problem.

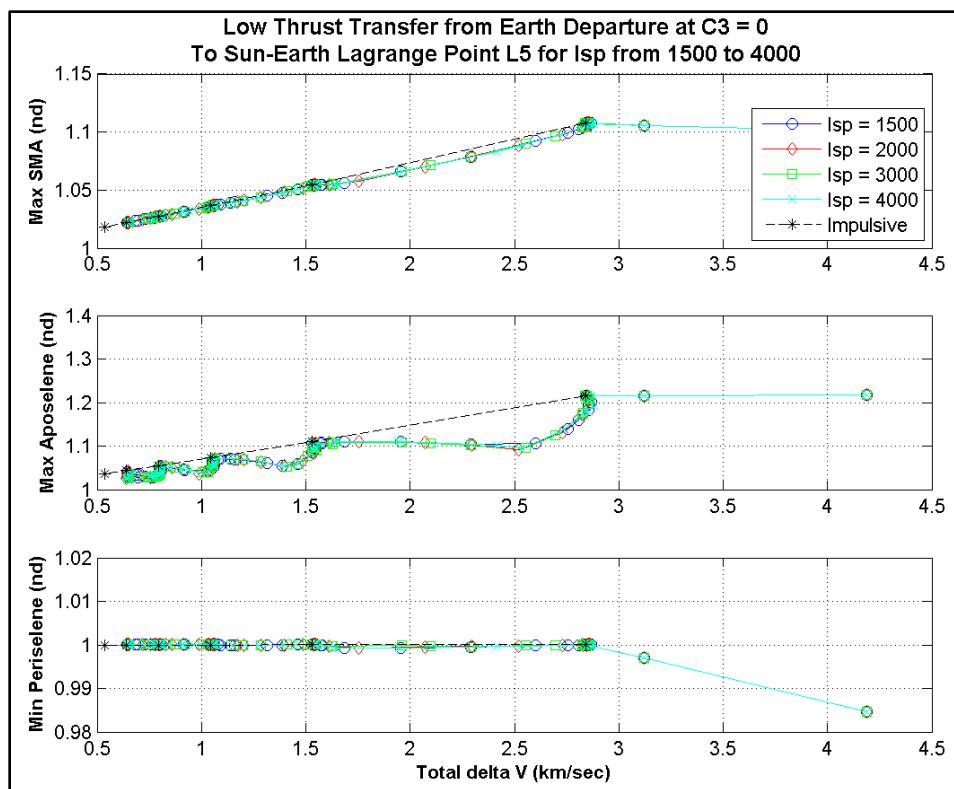


Figure 4-11. Orbital Parameters versus Total delta V for Low Thrust Transfers to S-E  $L_5$ . Multiple cases for engine Isp variances from 1500 to 4000 sec. Velocity change nearly linearly affects the in-plane shape of the transferring orbit via the

semi-major axis, but is apportioned differently between the two radii of apsides. Comparison to the impulsive velocity change results shown from the dashed black line.

The top plot in this figure shows a nearly linear relationship between the amount of delta velocity required to affect the semi-major axis and the size of the transfer orbit, which correlates well with the impulsive cases shown. There is an initial period for which a much larger delta velocity impact is needed for transit times less than the first 7:6 resonance period, or less than 1.1667 years. These cases are not afforded the time to within one revolution to properly size the apohelion, and the optimizer finds it more beneficial to apply the delta velocity to moving the near asides to the intersect point by affecting the argument of perihelion. For the impulsive cases that always apply the initial and final burns at the intersect point in the rotating frame, the affect is only seen in the apohelion value of the transfer orbit while the perihelion radius stays the same. This is shown once again by the dashed black trace in the lower two plots in Figure 4-11.

After about the first 7:6 resonance period (or after 1.167 year transit times) the longer duration mean motion about the transfer orbit allows the finite low thrust change to properly affect the apohelion radius only and no further impacts to the perihelion radius are needed.

For transit times occurring between the 7:6 resonance periods, the final intersect point is no longer coincident with the initial point at Earth, and therefore a portion of the velocity change must move the transfer orbit perihelion point away from the initial point by affecting the argument of perihelion of the transfer orbit to align with the new intersect point. It needs to move farthest at the transit times corresponding to the midpoint between the resonant periods, and thus requires the most additional delta velocity above that needed to affect the in-plane SMA



changes. These effects lead to the characteristic humps between the resonance points seen in the total delta velocity curves in Figure 4-10.

As has been shown for the low thrust transfer cases the total delta velocity needed is essentially independent of the Isp of the modeled motor. But the thrust for these cases does vary, and how that leads into the delta velocity needed for a given transfer case is based on the motor size and is a function of the proportional payload to motor mass. From the rocket equation,

$$\Delta v = v_e \ln \left( \frac{m_i}{m_f} \right) = g I_{sp} \ln \left( \frac{m_i}{m_f} \right)$$

Here  $\Delta v$  is the velocity change,  $v_e$  is the exit velocity of the propellants and is directly related to the thrust of the motor, and  $g$  is standard gravity. The initial to final mass ratio about the burn is shown by the fraction  $m_i/m_f$ , and indicates the usable propellants during a motor burn. For the cases seen here where a given  $\Delta v$  is fixed for varying values of Isp, the mass fraction must change proportionally with the change in Isp. This leads to the required fuel mass to change inversely with the change in Isp.

Lower Isp values then require higher thrust levels and correspondingly more fuel mass to produce the same velocity change. Figure 4-12 shows estimated values for the amount of fuel required to produce the corresponding delta velocity across a range of transit times for varying motor Isp characteristics. A motor with a lower Isp may cost less to produce the same amount of delta velocity, but would require more fuel and be a larger proportion of the total payload mass.

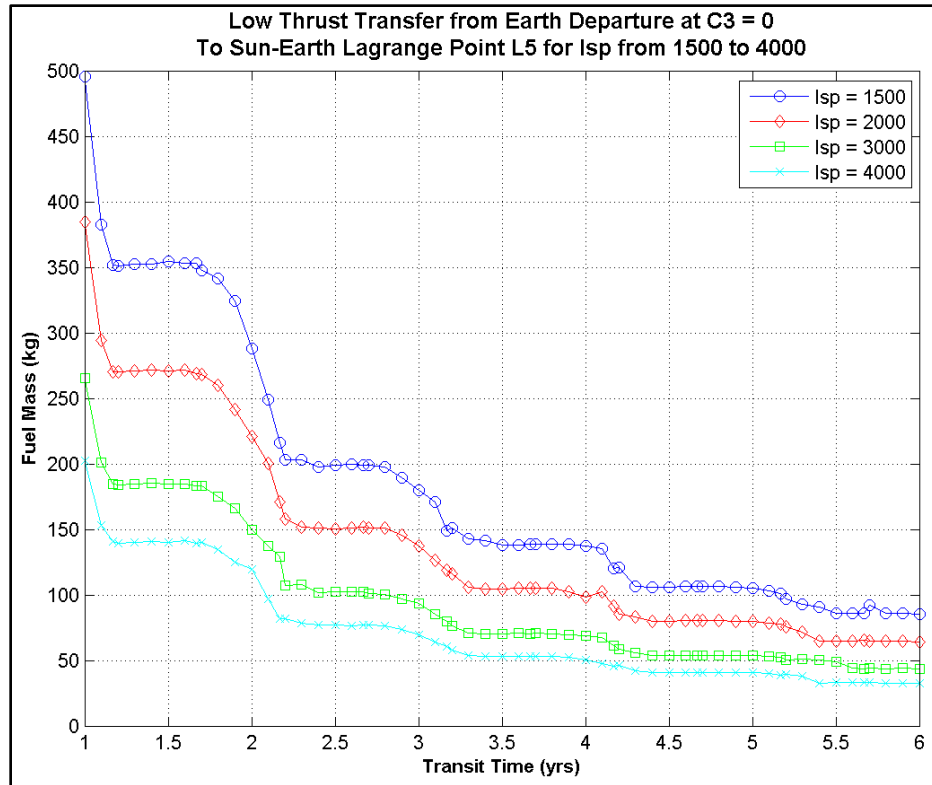


Figure 4-12. Estimated Fuel Mass versus Transit Time required achieving the desired  $\Delta V$  for a Transfer to S-E  $L_5$ . Fuel mass varies with engine Isp to achieve the resultant velocity change and is a greater proportion of total payload mass for higher velocity requirements.

### 4.3 Manifold Transport

Transfers from unstable periodic staging orbits about the  $L_1$  and  $L_2$  Lagrange points to stable periodic orbits about both of the triangular Lagrange points in the Sun-Earth circular rotating system were determined using the tools and methods described in Sections 2.2 and 2.3, above. Unstable invariant manifolds were propagated freely from various unstable periodic orbits about  $L_1$  and  $L_2$  until they intersected in position space various stable periodic orbits about  $L_4$  and  $L_5$ . The delta velocity needed to inject from the manifold onto the stable periodic orbit was calculated and the minimum velocity impacts were determined across the various staging periodic orbits. The results are plotted according to the Jacobi constant values for the departing unstable staging orbits about  $L_1$  and  $L_2$ , and the

Jacobi constant values for the arriving stable periodic orbits about  $L_4$  and  $L_5$ . The corresponding transit time it takes to translate along the given invariant manifold is also included on the traces.

The assumptions built into this analysis utilize the CRTBP modeling of the rotating Sun-Earth system and the location of the linear  $L_1$  and  $L_2$ , and triangular  $L_4$  and  $L_5$  Lagrange points. It is assumed the departing periodic orbits about the linear  $L_1$  and  $L_2$  points are unstable and therefore takes essentially no delta velocity to depart from them onto the transiting manifold.

Therefore the velocity magnitude results shown in this section are an indication of that needed to transfer from the unstable manifold state to the stable periodic orbit about the triangular Lagrange point at the intersecting position. This does not include any velocity change to launch from Earth to any of the periodic staging orbits about S-E  $L_1$  or  $L_2$  for a particular payload.

The Jacobi constant values for the departing and arriving periodic orbits are indicated on the axes in the following figures, with larger values corresponding to orbits closer to the corresponding Lagrange point. These figures attempt to compile on one plot the results of a multitude of initial and arrival conditions, akin to “pork chop” type plots that are commonly used to show results from Lambert’s solutions. The following sections step through  $L_1$  and  $L_2$  departing, and  $L_4$  and  $L_5$  arriving (both concentric and intersecting) periodic orbits and the associated transit times.

### 4.3.1 Transfer From S-E L<sub>1</sub> Staging Orbits to L<sub>4</sub> Periodic Orbits

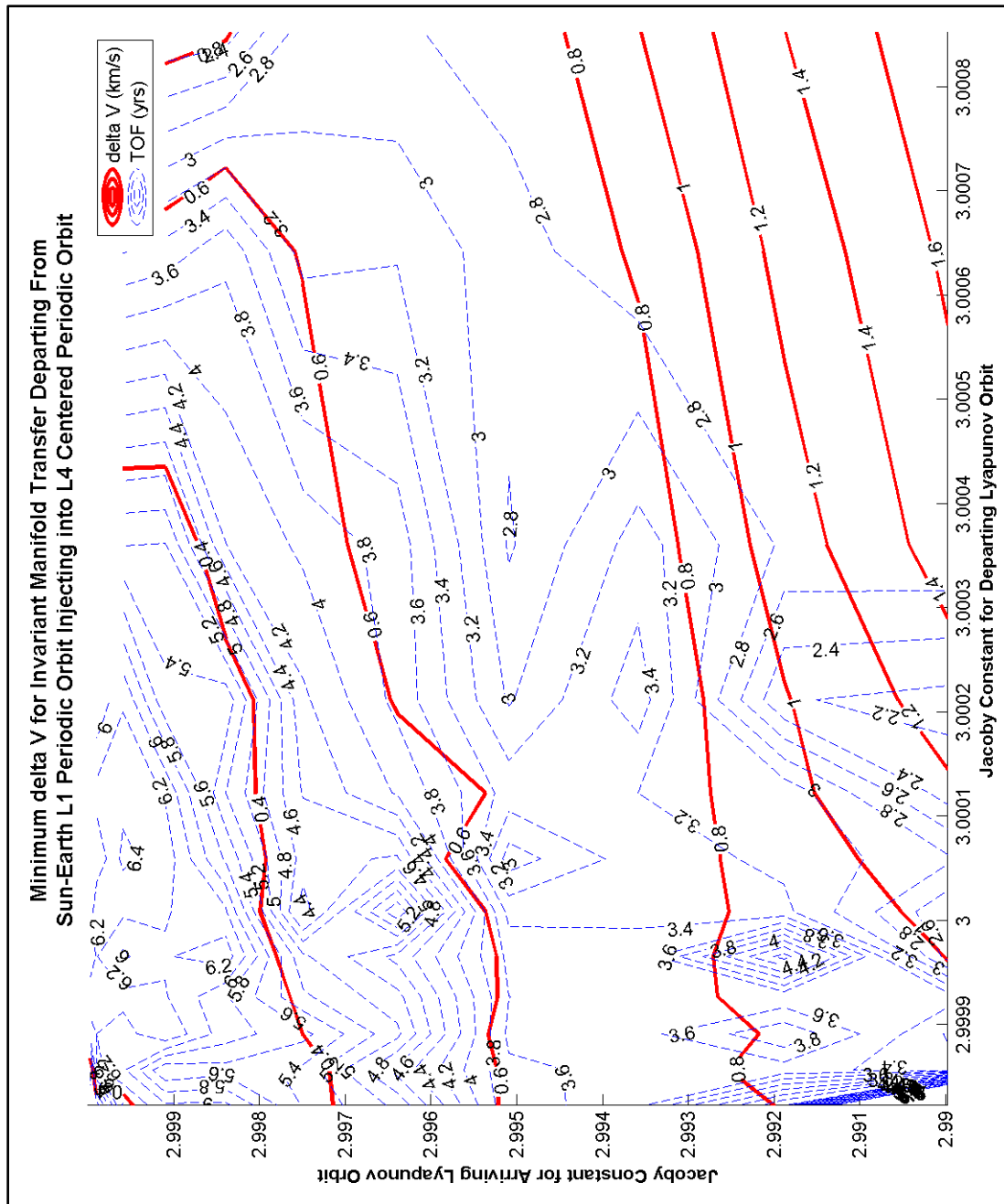


Figure 4-13. Delta Velocity and Time of Flight for Manifold Transfers from L<sub>1</sub> Periodic Orbits injecting into L<sub>4</sub> Centered Periodic Orbits.

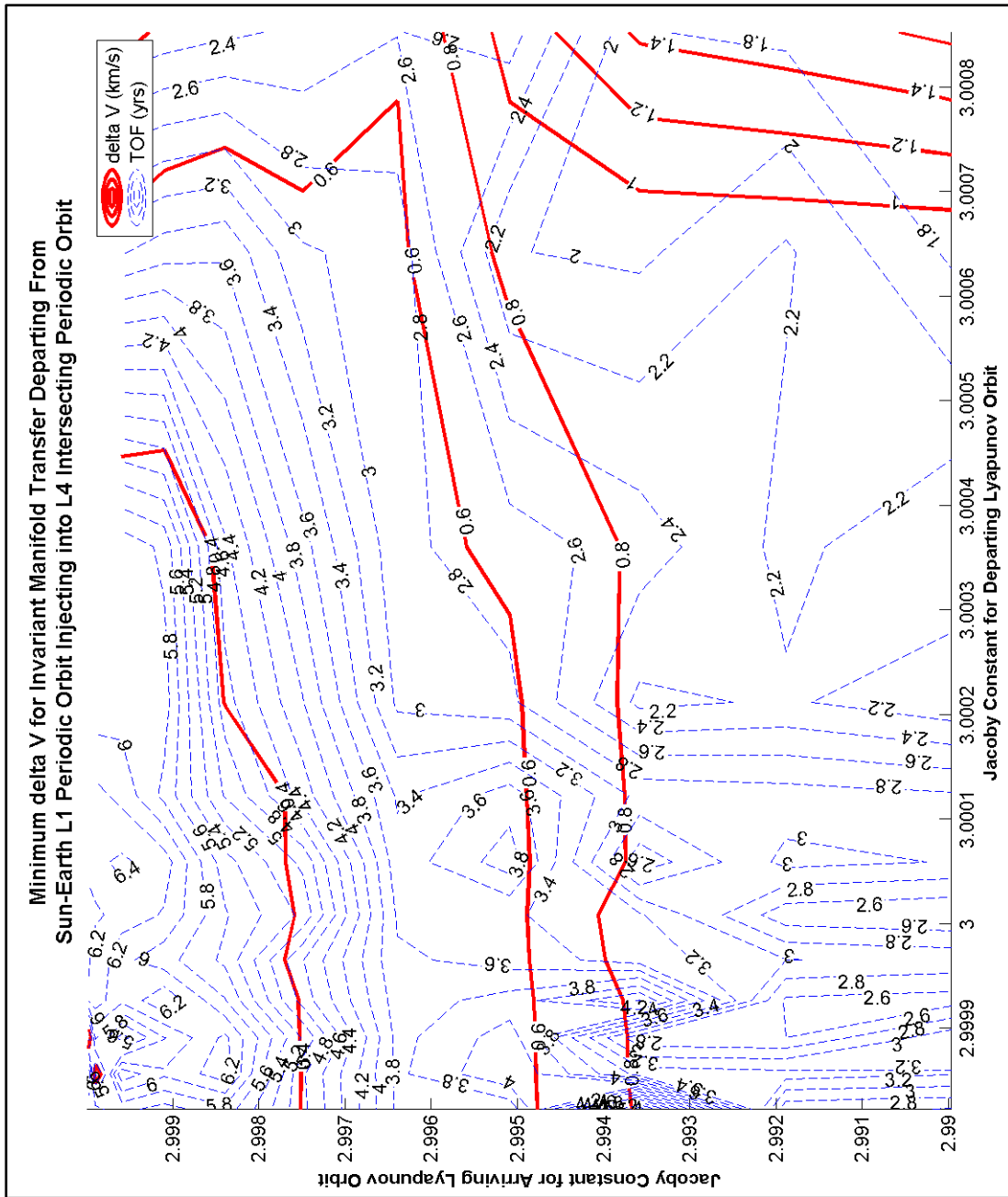


Figure 4-14. Delta Velocity and Time of Flight for Manifold Transfers from L<sub>1</sub> Periodic Orbits injecting into Periodic Orbits that intersect L<sub>4</sub>.

### 4.3.2 Transfer From S-E L<sub>2</sub> Staging Orbits to L<sub>4</sub> Periodic Orbits

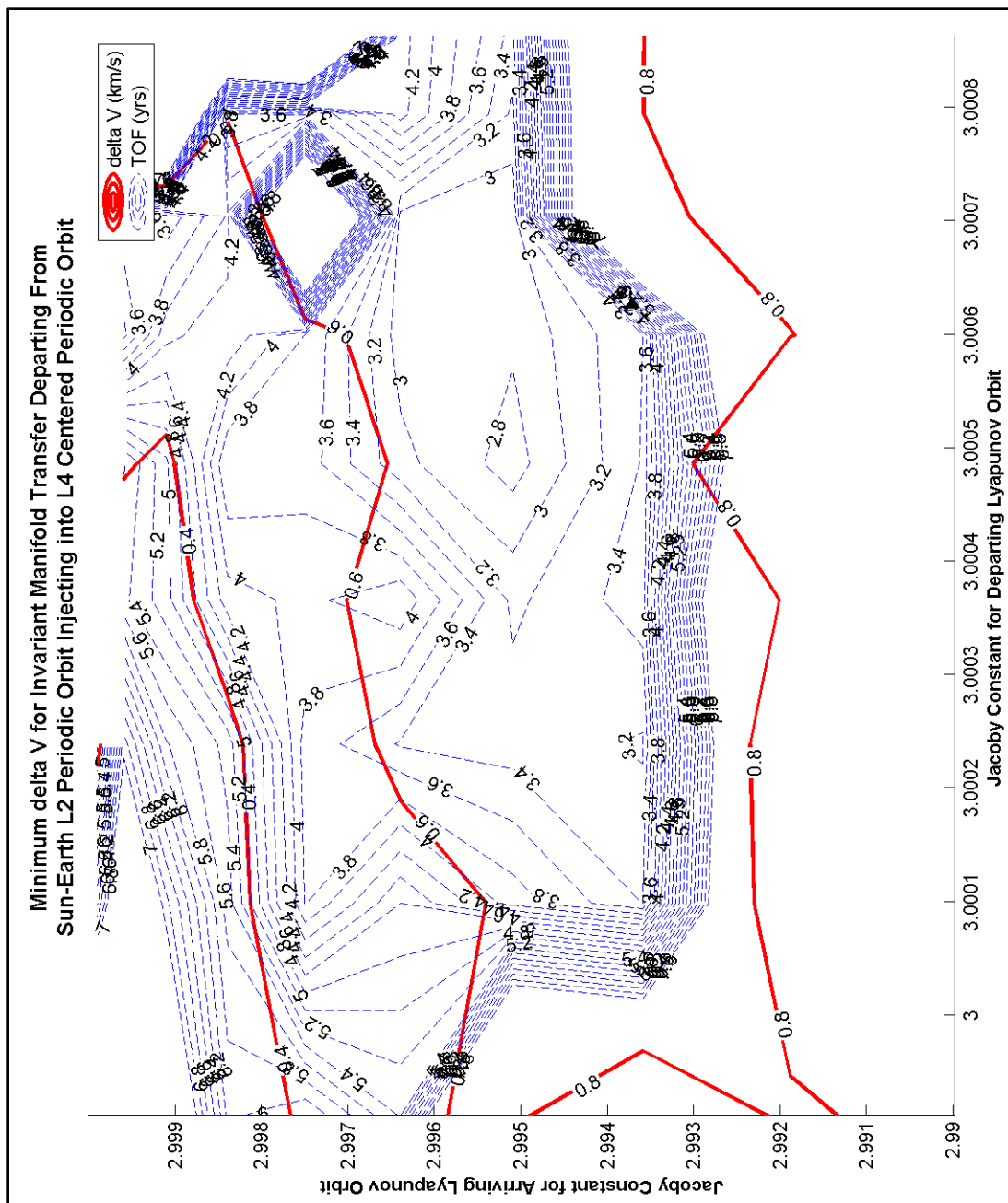


Figure 4-15. Delta Velocity and Time of Flight for Manifold Transfers from L<sub>2</sub> Periodic Orbits injecting into L<sub>4</sub> Centered Periodic Orbits.

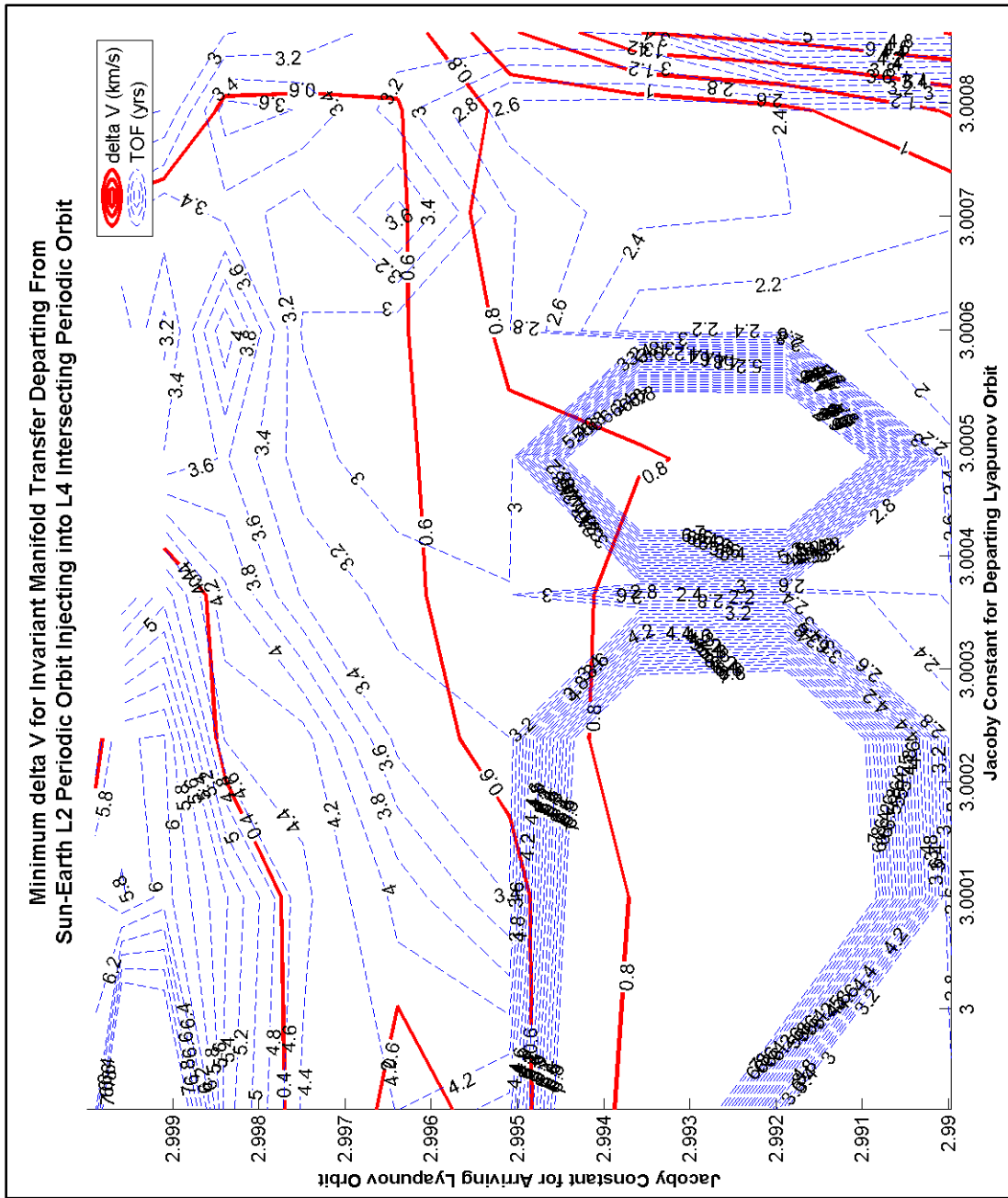


Figure 4-16. Delta Velocity and Time of Flight for Manifold Transfers from L<sub>2</sub> Periodic Orbits injecting into Periodic Orbits that intersect L<sub>4</sub>.

### 4.3.3 Transfer From S-E L<sub>1</sub> Staging Orbits to L<sub>5</sub> Periodic Orbits

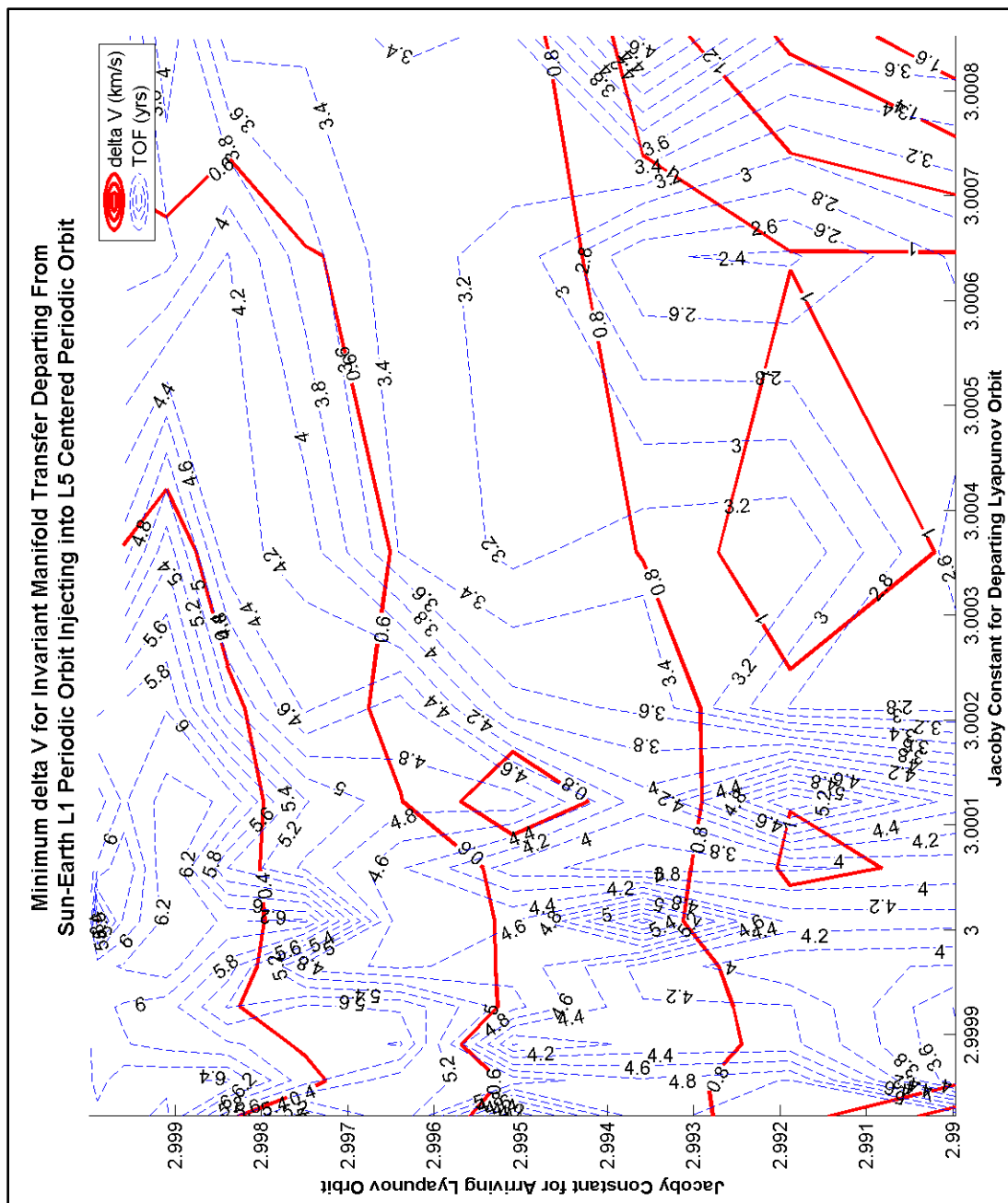


Figure 4-17. Delta Velocity and Time of Flight for Manifold Transfers from L<sub>1</sub> Periodic Orbits injecting into L<sub>5</sub> Centered Periodic Orbits.



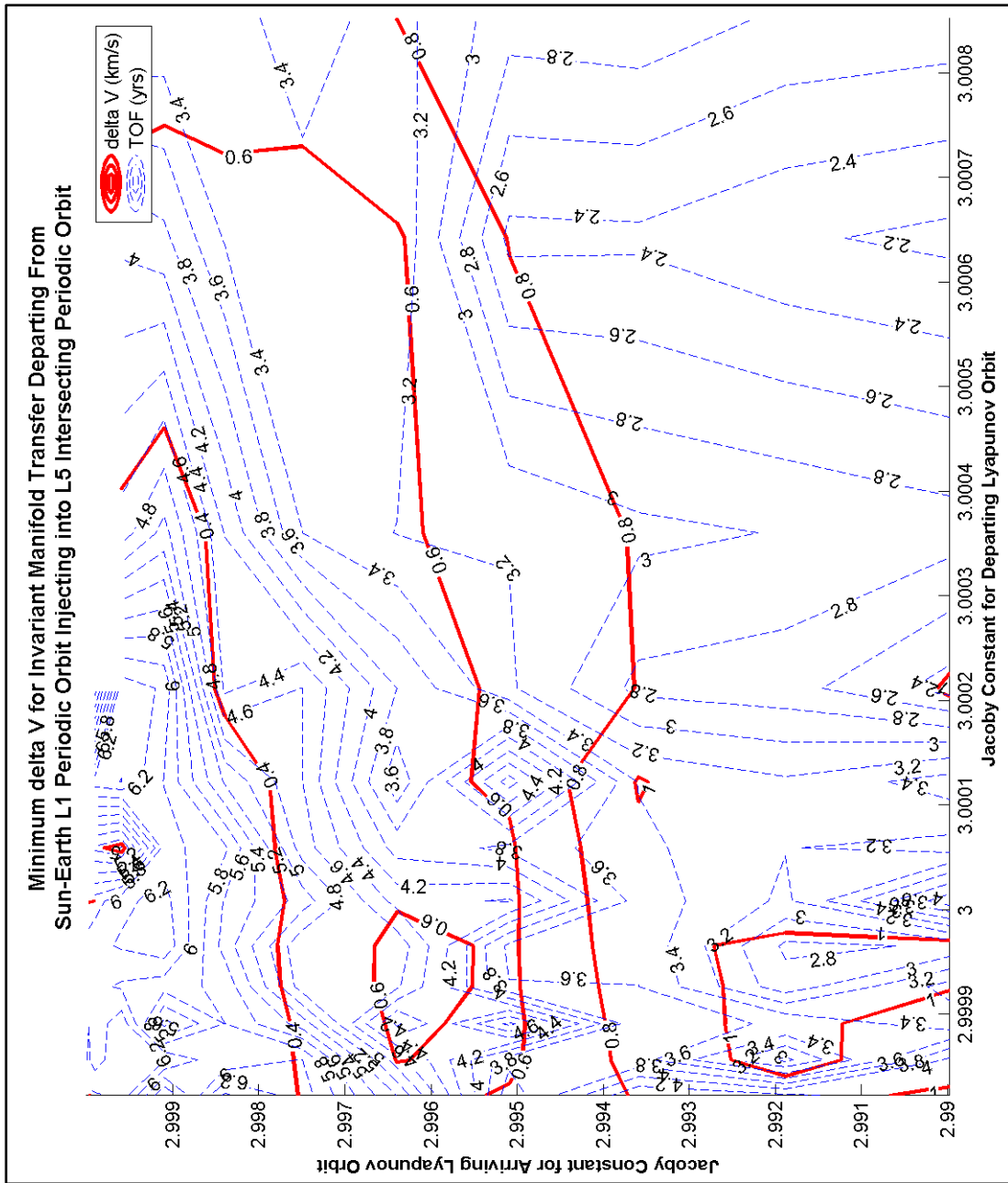


Figure 4-18. Delta Velocity and Time of Flight for Manifold Transfers from L<sub>1</sub> Periodic Orbits injecting into Periodic Orbits that intersect L<sub>5</sub>.

### 4.3.4 Transfer From S-E L<sub>2</sub> Staging Orbits to L<sub>5</sub> Periodic Orbits

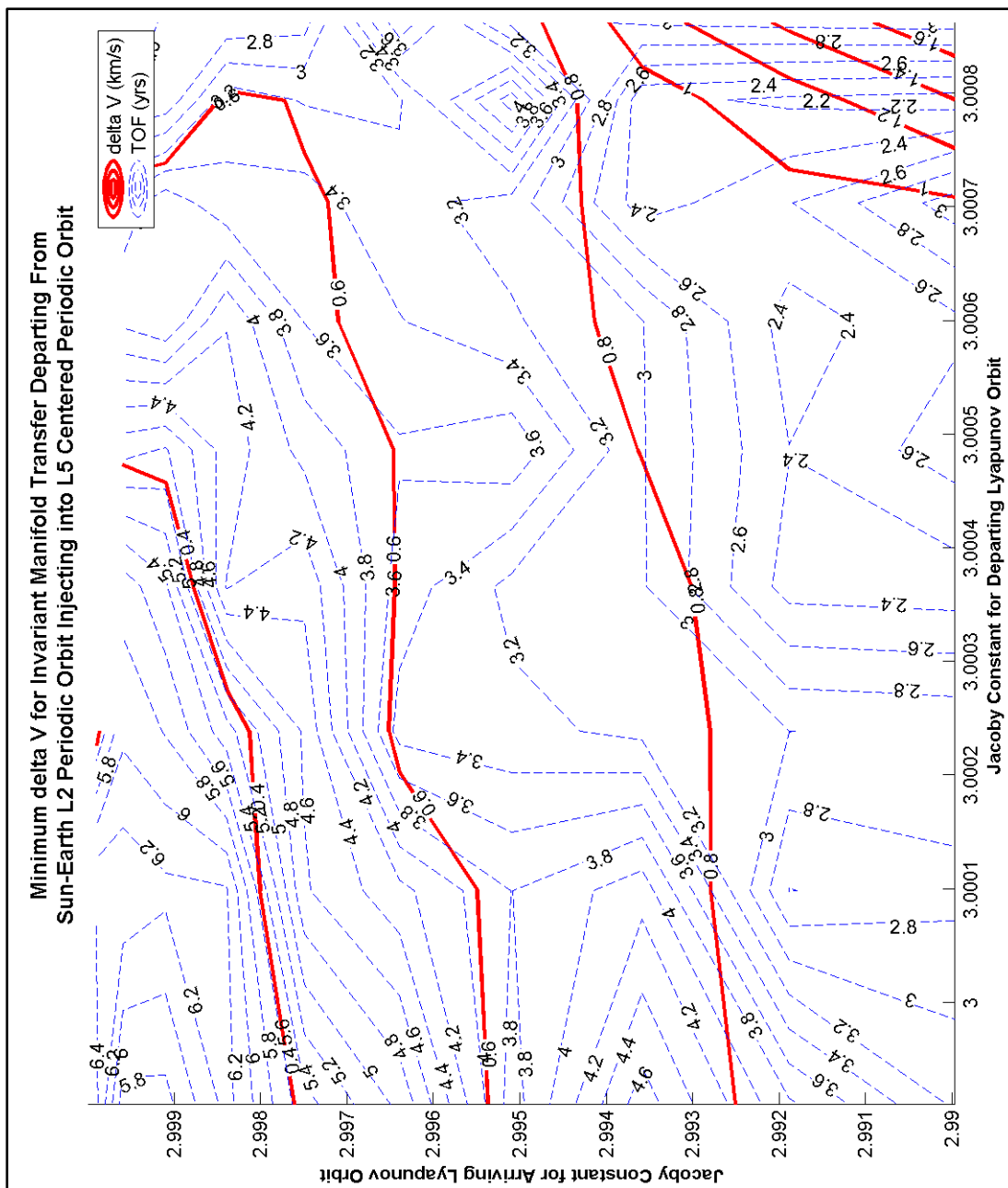


Figure 4-19. Delta Velocity and Time of Flight for Manifold Transfers from L<sub>2</sub> Periodic Orbits injecting into L<sub>5</sub> Centered Periodic Orbits.

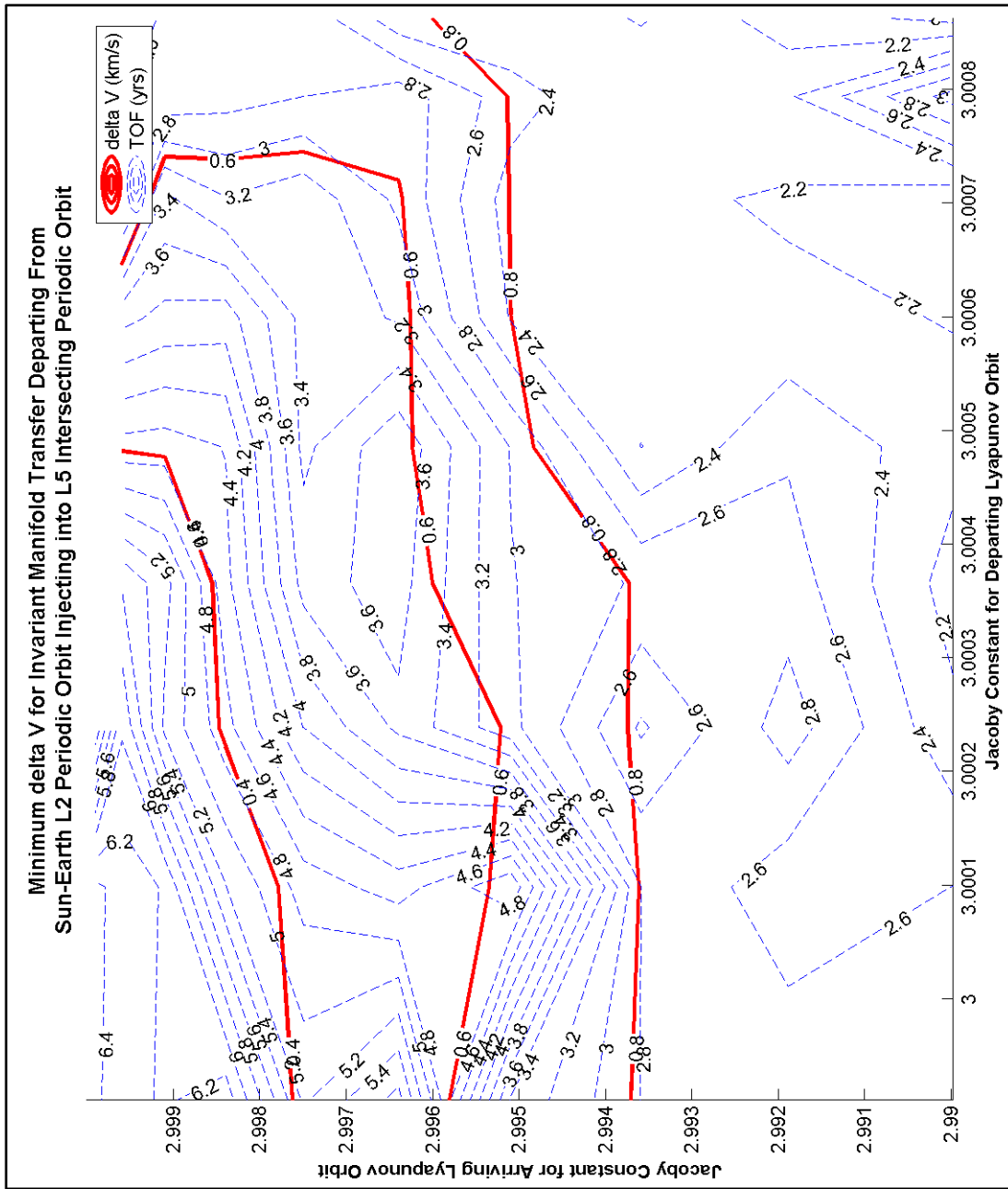


Figure 4-20. Delta Velocity and Time of Flight for Manifold Transfers from L<sub>2</sub> Periodic Orbits injecting into Periodic Orbits that intersect L<sub>5</sub>.

## CHAPTER 5

### SUMMARY AND CONCLUSIONS

#### 5.1 Summary of Contributions

The contributions to research that have been derived from this research start with the development of a method for generating families of periodic Lyapunov orbits about any radial axis in the three-body rotating frame. It has been demonstrated that unstable manifolds can be used to intersect both inner system NEO's and outer system KBO's within general velocity impact capabilities.

The development of a grid search method for transferring between various Lyapunov orbits to find the localized minimum velocity impact was performed and exercised with a wide range of results. Production of a parametric analysis of low thrust transfer capabilities to the Sun-Earth L4/L5 regions were completed with strong characterization of the engine results.

Overall, there was a survey of several methods for transfers to the Sun-Earth triangular Lagrange point region that can be utilized for potential mission designs to these regions in the future.

#### 5.2 Conclusions

The overall velocity cost for the various transfers complete from the Earth LEO orbit to the Sun-Earth L4 and L5 regions can be summarized in Figures 5-1 and 5-2, below. The low thrust results are shown as curves, while the transfer results are boxed in by the min/max delta velocity (circle and diamond, respectively). The specific transit times are those associated with those specific velocity points, and other flight time would need to be determined from the pork chop plots in Section 4.

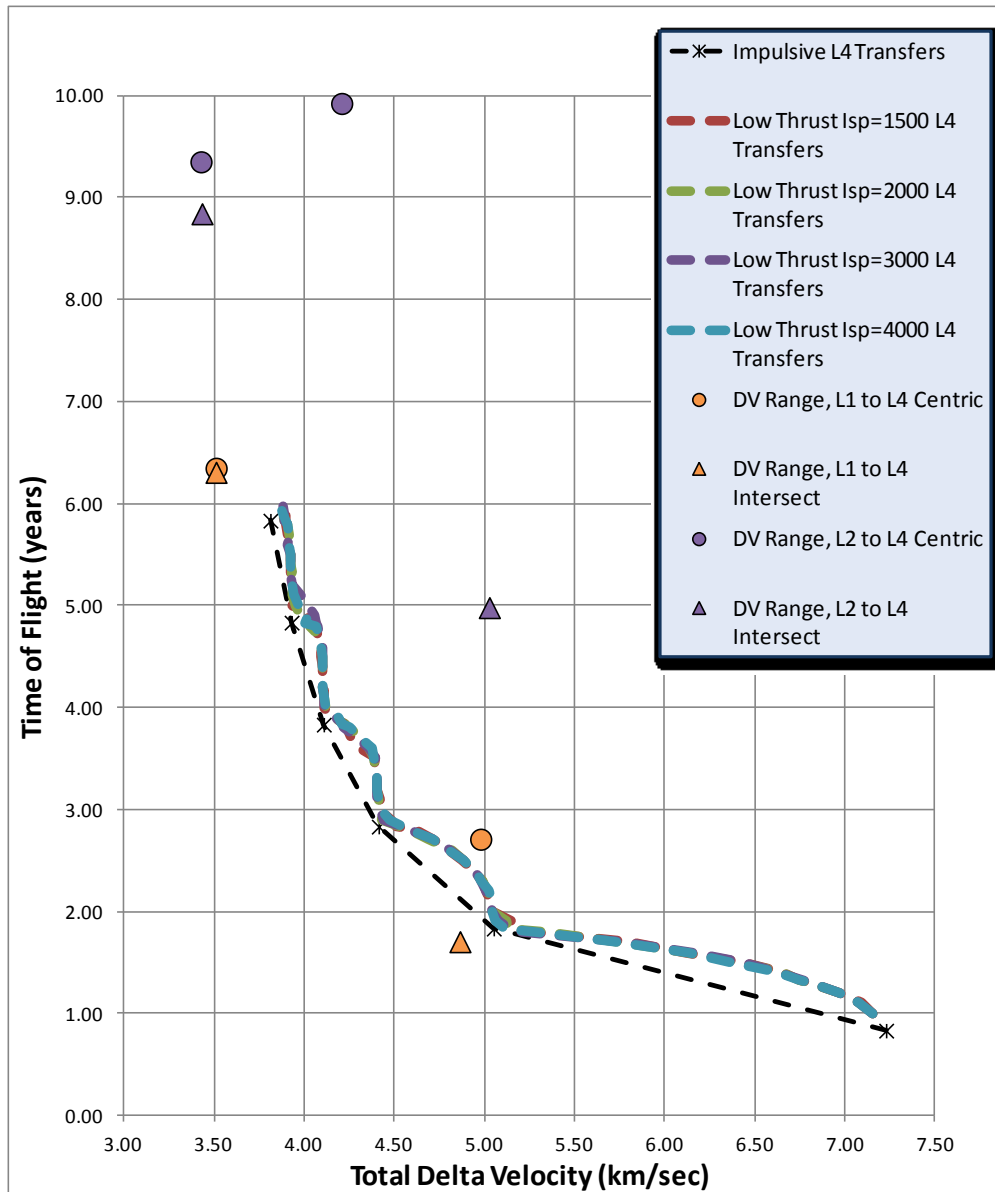


Figure 5-1. Summary of velocity impact versus time of flight for transfers from Earth LEO to the S-E L4 region using various techniques.

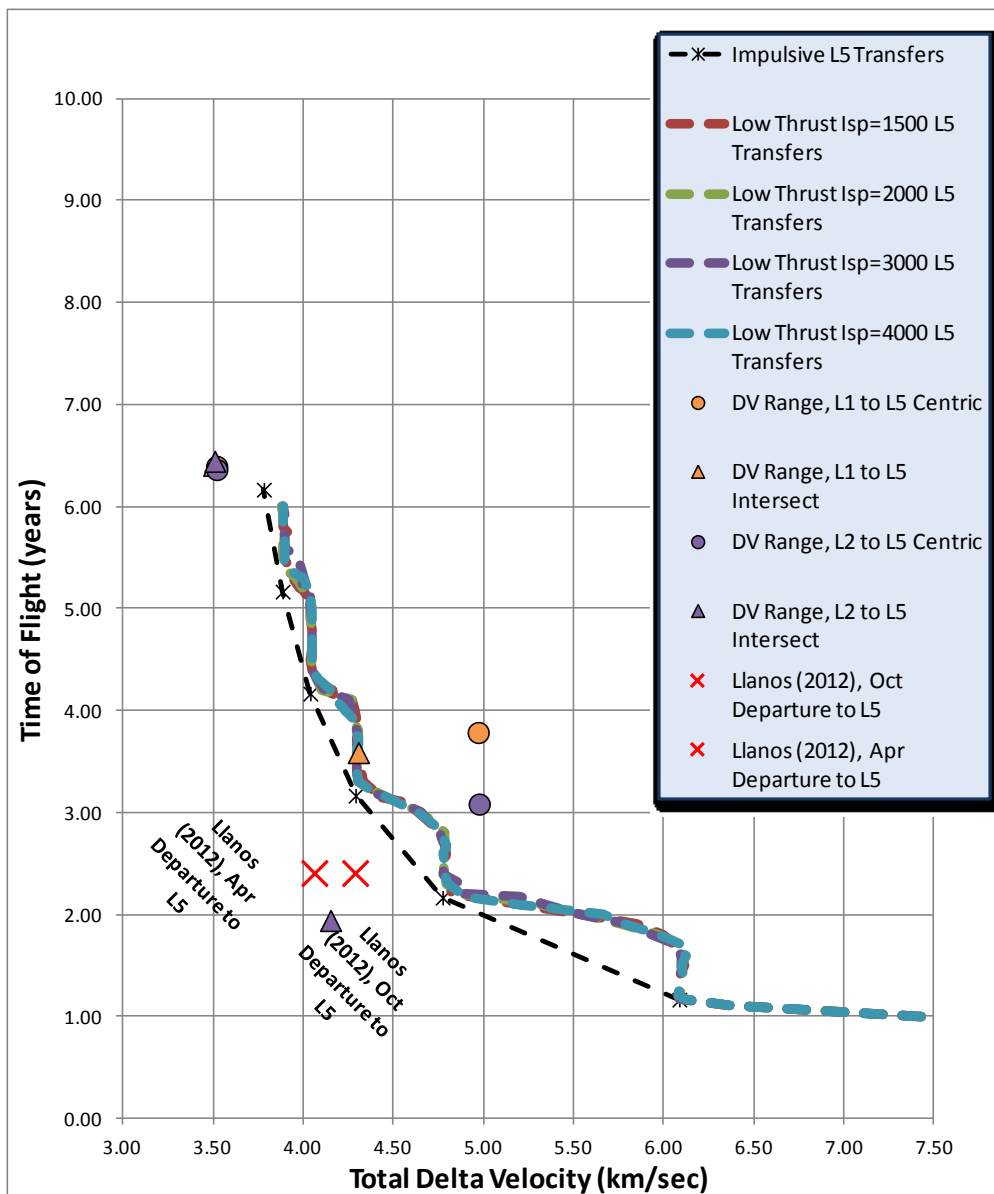


Figure 5-2 Summary of velocity impact versus time of flight for transfers from Earth LEO to the S-E L5 region using various techniques.

### 5.3 Future Work

While a vast amount of results were determined from this research, many other analyses can be performed to expand on these results. The determination of perturbation effects on the orbits should be analyzed and the results of the stability

of the orbits may change based on those features. More realistic cases can be looked at that contain out-of-plane effects to the transfer and periodic orbits.

Other techniques to help the transfer maneuvers, such as mid-course maneuvers or primer vector theory can be applied to determine if more cost savings can be found in the velocity impacts.

Further analysis on the relationship between the Jacobi constant and its affect on the manifold transfers to determine impact to the velocity cost for these types of transfers.

## BIBLIOGRAPHY

- Bate, R. R., Mueller, D. D., & White, J. E. (1971). *Fundamentals of Astrodynamics*. New York: Dover Publications, Inc.
- Brown, C. D. (1998). *Spacecraft Mission Design*. American Institute of Aeronautics and Astronautics, Inc., Second Edition.
- Christou, A. A. (2003). The Statistics of Flight Opportunities to Accessible Near-Earth Asteroids. *Planetary and Space Science*, 51, 221-231.
- Conley, C. (1968). Low Energy Transit Orbits in the Restricted Three-Body Problem. *SIAM Journal of Applied Mathematics*, 16, 732-746.
- Farquhar, R. W., Dunham, D. W., & McAdams, J. V. (1995). NEAR Mission Overview and Trajectory Design. *Journal of the Astronautical Sciences*, 43(4), 353-371.
- Farquhar, R. W., Dunham, D. W., Guo, Y., & McAdams, J. V. (2004). Utilization of Libration Points for Human Exploration in the Sun-Earth-Moon System and Beyond. *New Opportunities for Space. Selected Proceedings of the 54th International Astronautical Federation Congress*. 55, Number 3-9, pp. 687-700. Acta Astronautica.
- Gill, P. E., Murray, W., & Saunders, M. A. (Vol. 47, No. 1, 2005). SNOPT: An SQP Algorithm for Large-Scale Constrained Optimization. *SIAM Review*, 99-131.
- Gomez, G., Jorba, A., Masdemont, J., & Simo, C. (1993, August). Study of the Transfer from the Earth to a Halo Orbit Around the Equilibrium Point L1. *Celestial Mechanics and Dynamical Astronomy*, 56, 541-562.



- Gomez, G., Llibre, J., Simo, M. R., & Simo, C. (2001). Dynamics and Mission Design Near Libration Points Vol. I Fundamentals: The Case of Collinear Libration Points. *World Scientific Monograph Series in Mathematics. 2*. New Jersey: World Scientific.
- Herman, J. (2012). *Preliminary Mission Analysis for a Far-Side, Highly Inclined Solar Observatory using Electric Propulsion*. Master's Thesis, Delft University of Technology.
- Howell, K. C. (1984). Three-Dimensional, Periodic, 'Halo' Orbits. *Celestial Mechanics, 32*(53).
- Howell, K. C., Barden, B. T., & Lo, M. W. (1997, April-June). Application of Dynamical Systems Theory to Trajectory Design for a Libration Point Mission. *The Journal of Astronautical Sciences, 45*(2), 161-178.
- Jet Propulsion Laboratory. (2007, August 11). *HORIZONS System*. Retrieved from Solar System Dynamics: <http://ssd.jpl.nasa.gov/>
- Lathrop, B. W., & Anderson, R. L. (2010). Survey of Delta V Requirements for Low Energy Transfers to Near Earth Objects. *George H. Born Symposium*. Boulder, CO: American Astronautical Society.
- Llanos, P. J., Miller, J. K., & Hintz, G. R. (2012). Mission and Navigation Design of Integrated Trajectories to L4, L5 in the Sun-Earth System. *AIAA/AAS Astrodynamics Specialist Conference*. Minneapolis: AIAA.
- Lo, M. W. (2001). The Interplanetary Superhighway and the Origins Program. *Aerospace Conference Proceedings (2002)*. 7, pp. 3543-3562. IEEE.
- Mitchell, S. (2005). Analysis and Identification of Three-Asteroid (NEO) Rendezvous Missions. *15th American Astronautical Society / AIAA Space Flight Mechanics Conference*.
- Murray, C. D., & Dermott, S. F. (1999). *Solar System Dynamics*. New York: Cambridge University Press.

- NASA. (2013, June 2). *NASA Missions*. Retrieved from Solar System Exploration:  
<http://solarsystem.nasa.gov/>
- NASA/JPL. (2010, April 07). Retrieved from Near Earth Object Program:  
<http://neo.jpl.nasa.gov>
- Perozzi, E., Rossi, A., & Valsecchi, G. B. (2001). Basic Targeting Strategies for Rendezvous and Flyby Missions to the Near-Earth Asteroids. *Planetary and Space Science*, 49, 3-22.
- Rayman, M. D., Fraschetti, T. C., Raymond, C. A., & Russell, C. T. (2006). Dawn: A Mission in Development for Exploration of Main Belt Asteroids Vesta and Ceres. *Acta Astronautica*, 58(11), 605-616.
- Roy, A. E. (2005). *Orbital Motion*. Bristol and Philadelphia: Institute of Physics Publishing, Fourth Edition.
- Salazar, F. J., Macau, E. E., & Winter, O. C. (2013, November 29). Alternative Transfer to the Earth-Moon Lagrangian Points L4 and L5 Using Lunar Gravity Assist. *Advances in Space Research*.
- Sims, J., & Flanagan, S. (1999). Preliminary Design of Low-Thrust Interplanetary Missions. *AAS/AIAA Astrodynamics Specialist Conference*. Girdwood, Alaska: AAS/AIAA.
- Sims, J., Finlayson, P., Rinderle, E., Vavrina, M., & Kowalkowski, T. (2006). Implementation of a Low-Thrust Trajectory Optimization Algorithm for Preliminary Design. *AIAA/AAS Astrodynamics Specialist Conference Proceedings* (pp. 1872-1881). Keystone, CO: AIAA.
- Stacey, R. G., & Connors, M. (2009). Delta-V Requirements for Earth Co-Orbital Rendezvous Missions. *Planetary and Space Science*, 57, 822-829.
- Szebehely, V. (1967). *Theory of Orbits: The Restricted Problem of Three Bodies*. New York: Academic Press.

- Vallado, D. A. (1997). *Fundamentals of Astrodynamics and Applications*. McGraw-Hill Companies, Inc.
- Wiggins, S. (2003). Introduction to Applied Nonlinear Dynamical Systems and Chaos. In *Texts in Applied Mathematics* (Vol. 2, pp. 28-70). New York: Springer-Verlag.
- Yano, H., Kubota, T., Miyamoto, H., Okada, T., Scheeres, D., Takagi, Y., . . .  
Yoshikawa, M. (2006). Touchdown of the Hayabusa Spacecraft at the Muses Sea on Itokawa. *Science*, 312(5778), 1350-1353.

## APPENDIX A

These are detailed plots of the optimized thrust profiles for various times of flight for low thrust cases going from an Earth escape state to the respective Sun-Earth L4/L5 point. The transit times vary from 1 to 6 years, and the cases shown are for Isp levels of both 1500 seconds and 4000 seconds. See the captions within the figures for the respective details.

